An investigation into the crystallographic and magnetic properties of some REPtIn compounds (RE=Ho,Dy)

This item was submitted to Loughborough University's Institutional Repository by the/an author.

Additional Information:

- A Doctoral Thesis. Submitted in partial fulfillment of the requirements for the award of Doctor of Philosophy of Loughborough University.

Metadata Record: https://dspace.lboro.ac.uk/2134/6359

Publisher: © D.E. Pooley

Please cite the published version.

An investigation into the crystallographic and magnetic properties of some REPtIn compounds (RE=Ho,Dy)

by

Daniel E. POOLEY

Doctoral Thesis

Submitted in partial fulfillment of the requirements for the award of Doctor of Philosophy of Loughborough University

May 27, 2010

Abstract

This thesis concerns the determination of the magnetic properties of DyPtIn and HoPtIn. For this a series of neutron scattering experiments on both powder and single crystal samples were undertaken. The powdered sample data analysis determined the temperature dependence of the magnetic phases of DyPtIn. This was found to be a two-stepped transition, described by two propagation vectors. The first phase propagation vector, $\boldsymbol{k}_1 = [0, 0, 0]$, was determined to order below $T_c = 28.1 \pm 0.3$ K. The second phase propagation vector, $\boldsymbol{k}_2 = [\frac{1}{2}, 0, \frac{1}{2}]$ orders below $T_{ab} = 18 \pm 2$ K. Using symmetry analysis the magnetic moments were found to be restricted to the c-axis for the first phase. The second phase allowed a component within the ab-plane, antiferromagnetic in nature. The maximal ordered moment, for DyPtIn, extrapolated to T=0 K was found to be $\mu_{total}^{av} = 7.90 \pm 0.09 \mu_B/Dy$, which is reduced compared to the theoretic moment of $\mu_{theory} = 10 \mu_B/Dy$.

The single crystal analysis showed the magnetic moment of HoPtIn to be aligned to the c-axis at low temperatures. In this compound the full moment is measured, $\mu_{Total} = 10.4 \pm 0.4 \mu_B/Ho$.

Using a new method of data reduction, the form factor for Ho^{3+} was extracted. The method for this was developed to solve the problems of the non-centrosymmertic structure for the REPtIn compounds. To analyse this data, a program has been developed and tested to fit the full multipole expansion of the form factor to the measured form factor, or to the flipping ratio data. This programme can determine the crystalline electric field parameters from flipping ratio data taken on any of the REPtIn compounds.

Acknowledgements

First I would like to thank my supervisor Dr Klaus Neumann for his help and expertise, which enabled me to perform this research for my PhD. The nature of my PhD has allowed me to make new friends and scientific contacts across Europe, all of which I have him to be grateful for.

I would also like to thank everyone at Loughborough University for their help and friendship. Particular thanks goes to Bryan Dennis, who was always on hand to guide when things were going well and stepped in when they were not!

I would like to thank three people for their contribution toward this thesis. Firstly, Dr Emilia Morosan for supplying high quality single crystal samples for the D3 and D9 experiments. Secondly, Dr Janusz Waliszewski for his analysis of the flipping ratio data using maximum entropy techniques. Thirdly, Dr Reinhard Kremer for organising my three visits to the MPI in Stuttgart, allowing me to use their facilities, resources and expertise.

Special thank-yous go out to Andy P, Stan, Nuff, Chris H, Matt L, Amer, Mowgli, Tom P.G.F and Mark K for their help, friendship and occasional prank.

Thank you to my beautiful girlfriend Sonia, who has supported me through my studies, putting up with the trips to France, the long distance relationship, the stress, my zero income for half a year and my moods. I love you very much.

Thank you to all my family who have always supported me, particularly through my early education. Thank you to Sheila, who's insight and help changed my life.

Most of all I am grateful to Mum and Dad. Their continuing belief that I could achieve good things provided I went to the right school seems to have been right in the long run. I have no doubt that without their continued love, support and faith I would not have achieved what I have. This work is dedicated to them with all my love.

Contents

Chapter 1

Introduction

1.1 Research Aims

The aim at the start of this research was to explain the crystallographic and magnetic properties of some of the REPtIn compounds. It is hoped that this experimental study will answer some of the outstanding question that remain for this series. These questions are fully discussed in the next section, where the motivation for studying these compounds is presented along with the relevant background physics. For instance, an explanation for the reduction in the ordered magnetic moment remains outstanding. Across the REPtIn series the ordered magnetic moment is substantially less than that expected for the free rare earth ion [1], [2] [3] [4]. This is surprising, as the moment is localised on the 4f shell, and should be unaffected by metallic bonding [5].

Another unanswered question relates to the nature of the mechanism causing the strong magnetic anisotropy seen in single crystal magnetisation data [6]. This anisotropy exists beyond energy scales far exceeding the energy scale set by the magnetic ordering temperature. Several authors suggest [2], [7], that the crystalline electric field (CEF) splitting of the 4f degeneracy gives rise to this anisotropy. However, this explanation is inadequate for the REPtIn series, as strong anisotropy is observed also in the GdPtIn compound. GdPtIn is in a $L = 0$ configuration, so the 4f electron distribution is spherically symmetric. This means there is no preferred direction and there should be no anisotropy

in this compound. Despite this, some authors do attribute these effects to the CEF splitting, but no one has attempted to evaluate the magnitude of the B coefficients. This is due to the site symmetry of the RE ion requiring the full CEF hamiltonian, which gives an under-determined problem when analysing inelastic neutron data.

These physical problems and unanswered questions make the REPtIn series an excellent opportunity for PhD research. This study has benefited from the previous research conducted at Loughborough University, where much of the physics of the REPtIn has been discovered.

To achieve these research aims the determination of the magnetic ground state of some of these compounds is required. This involves neutron diffraction experiments and analysis of both powder and single crystal samples with the intention of determining the crystalline electric field splitting of the RE^{3+} ion. The determination of the magnetisation density of the select compounds is also essential, if progress beyond that reported in the literature is to be made. This analysis also requires complementary measurements, such as SQUID magnetisation data and X-ray diffraction measurements.

1.2   Thesis Structure

The structure of this thesis reflects the order in which the research aims were addressed. Listed below is a brief description of the content of each chapter within this thesis. It should be noted that the abbreviation 'RE' or 'RE^{3+}' is used frequently throughout, where the reference is being made to a rare earth atom or triply-ionised rare earth ion respectively.

- Chapter 2 provides an introduction to the REPtIn series explaining the interesting physics observed and the relevant theory. This is followed by a literature review of several noteworthy members of the REPtIn series, and a discussion of the theories reported to explain the magnetic ordering of the series.

- Chapter 3 is a self-contained chapter, which explains the theory of neutron scattering. The essential theory of nuclear and magnetic neutron

scattering is discussed with an emphasis on some aspects, which will be used for data reduction and analysis. This chapter is frequently referred to, as it provides the background for the form factor analysis in chapter 6.

- Chapter 4 is the first results chapter. It reports on powder diffraction experiments and analysis of the compounds DyPtIn and HoPtIn. The temperature dependance of the magnetic ordering of DyPtIn is reported, along with the determination of the magnetic structure. HoPtIn is measured and compared to the work of Baran *et al.* [1]. The motivation for this approach is discussed in chapter 2. Further discussion emphasises the need for single crystal measurements to determine the magnetisation density within the unit cell.

- Chapter 5 reports on two single crystal experiments performed at the Institut Laue-Langevin using the instruments D9 and D3. This chapter presents the magnetisation density of HoPtIn using maximum entropy reconstruction, and discusses the added complexity of analysing data of non-centrosymmetric structures.

- Chapter 6 provides an account of coding a programme, which extracts the Ho^{3+} form factor from flipping ratio data. This chapter implements the theory described in chapter 3, and uses the experimental findings of chapter 5 to determine the Ho^{3+} form factor.

- Chapter 7 concludes the research conducted for this thesis, and discusses the final results obtained. Suggestions are put forward for further work.

Chapter 2

Background and Motivation for Study

2.1   Introduction

The REPtIn series has been studied by several research groups including Morosan, Bud'ko and Canfield [6], Watson, Neumann and Ziebeck [3] and Baran, Gondek, Hernández-Velasco, Kaczorowski and Szytula [1]. The following sections aim to introduce the physics of the REPtIn series, reported by these authors. From these experimental results it is clear that there is physics that remains unexplained. This will be discussed and succinctly outlined as a set of unanswered questions. By the end of this chapter the reader should understand the requirement for further work on the REPtIn series and the way in which these problems will be addressed.

The first two sections of this chapter provide background information on the physics relevant to the theme compounds, DyPtIn and HoPtIn. This includes the crystallography and magnetic properties of the REPtIn compounds and observed effects such as 'canting' and 'frustration'.

The third section introduces the ideas behind crystalline electric field splitting, and why is it relevant to the magnetic order of the REPtIn series.

The final section in this chapter is a full literature review of the theme compounds. This includes a further subsection, where general trends of the

REPtIn series are discussed in section 2.3.3.

2.2 Crystallography of the REPtIn Series

The equiatomic REPtIn series crystallises in the hexagonal ZrNiAl-type structure with the exception of EuPtIn [8], which forms in the orthorhombic TiNiSi-type structure. As EuPtIn is the exception, any reference to the 'REPtIn series' does not include this compound. The hexagonal space group was originally determined by Ferro *et al.* [9] [10] to be $P\overline{6}2m$. This space group is non-centrosymmetric. The REPtIn structure consists of alternating planes along the crystallographic c-axis. The $z = 0$ plane contains two platinum ions and all the indium ions. This layer is effectively non-magnetic. As the RE ions are located within the $z = \frac{1}{2}$, and there are no magnetic atoms elsewhere, this series can be classified as a low-dimensional system [11] [12]. However, most of these compounds order magnetically at relatively high temperatures, such as GdPtIn where T_C=67.5 K [2].

The $z = \frac{1}{2}$ plane contains all the RE ions arranged in equilateral triangles. There are three formula units per primitive unit cell with the positions tabulated in 2.1 below.

Species	Site	Site Symmetry	Positions
RE	3g	m2m	$(x_{RE}, 0, \frac{1}{2})$, $(0, x_{RE}, \frac{1}{2})$, $(\overline{x}_{RE}, \overline{x}_{RE}, \frac{1}{2})$
Indium	3f	m2m	$(x_{In}, 0, 0)$, $(0, x_{In}, 0)$, $(\overline{x}_{In}, \overline{x}_{In}, 0)$
Platinum	2c	$\overline{6}$	$(\frac{2}{3}, \frac{1}{3}, 0)$, $(\frac{1}{3}, \frac{2}{3}, 0)$
Platinum	1b	$\overline{6}2m$	$(0, 0, \frac{1}{2})$

Table 2.1: *The occupied sites for the REPtIn series. Typical values for the free position parameters are $x_{In} \sim 0.3\mathring{A}$ and $x_{RE} \sim 0.6\mathring{A}$.*

Each RE site is a part of three equilateral triangles within the ab-plane. The triangle centred at $(0,0,\frac{1}{2})$ has a Pt ion in its centre located on the 2c-site. This arrangement is shown in part (c) of figure 2.1, where the atomic basis is also shown. The triangular geometry is such that a Dzyaloshinskii-Moriya [13] [14] type interaction is allowed, which could polarise the Pt ion. An interaction of this type would result in a small magnetic moment located

on the Pt site. This mechanism has been suggested by Stephens *et al.* [4] to explain the anisotropy seen in the REPtIn series.
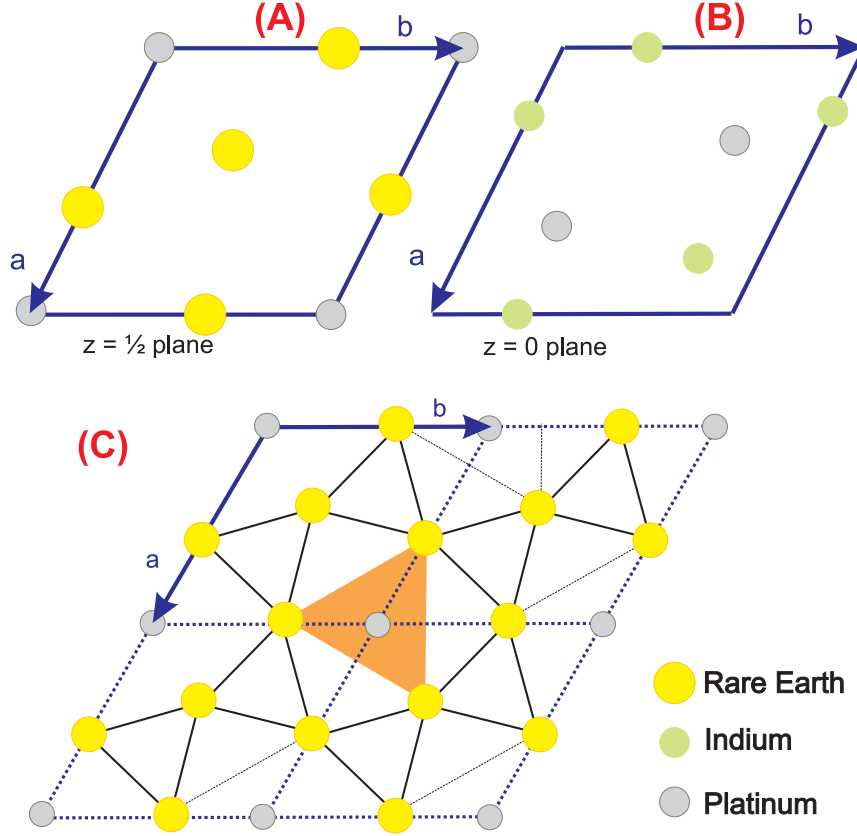
Figure 2.1: *The unit cell and atomic basis in the $z = \frac{1}{2}$ (**A**) and $z = 0$ (**B**) planes. (**C**): Four unit cells in the $z = \frac{1}{2}$ plane, highlighting the equilateral triangle around the platinum site.*

Typical values for the cell dimensions at low temperature are $\boldsymbol{a} \sim 7.57$ Å and $\boldsymbol{c} \sim 3.84$ Å. As the **a**-axis is nearly twice that of the **c**-axis, there is less distance between RE sites described by the translation $\boldsymbol{T} = (0, 0, \pm 1)$ than a RE neighbour within the ab-plane. As such, magnetic correlations along the **c**-axis are not negligible, and any model that restricts magnetic interactions to the ab-plane should be implemented with caution.

The nearest neighbours to the RE site located at $(x_{RE}, 0, \frac{1}{2})$ are the four Pt

sites located at $(\frac{2}{3},\frac{1}{3},0)(\frac{1}{3},\frac{2}{3},0)$, $(\frac{2}{3},\frac{1}{3},1)$ and $(\frac{1}{3},\frac{2}{3},1)$. Each of these Pt sites links an equilateral triangle centred at $(\frac{2}{3},\frac{1}{3},\frac{1}{2})$ to the equivalent RE triangle in the $z = \frac{1}{2}$ plane in the above and below unit cells. As such, the RE and Pt atoms form a 'pyramid' structure along the **c**-direction. A diagram of this structure is shown below in 2.2. As the Pt ion is easily polarised, this pyramid structure could give rise to magnetic correlation between the alternating planes, despite there being a shielding layer of In and Pt ions in between.
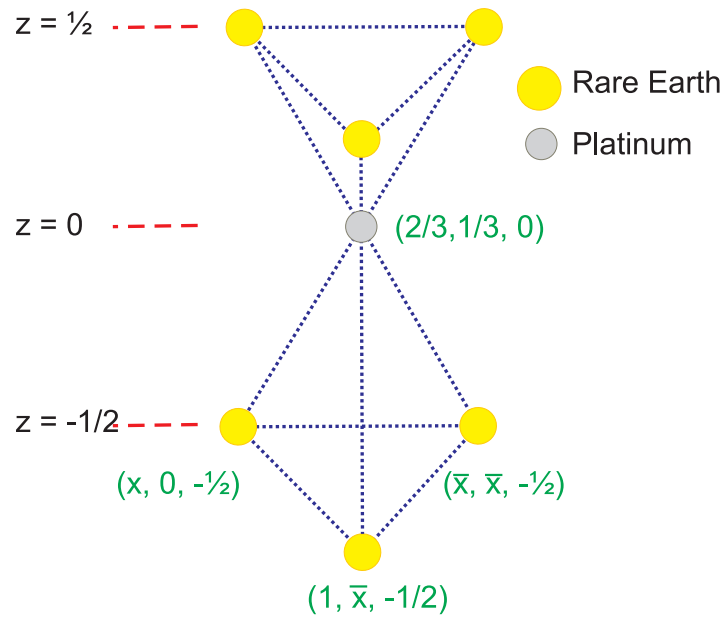
Figure 2.2: *The pyramid arrangement of RE and platinum sites. The atomic positions are given in green. In the figure 'x' is a free position parameter, typically $x \sim 0.6$ Å. This diagram shows two equivalent planes, that of $z = 0$ and $z = 1$.*

The complexity of the RE-Pt structure is further described with the aid of table 2.2 below. This table lists the distances to the neighbouring ions of the RE site located at $(_{RE},0,\frac{1}{2})$, where $x_{RE} = 0.5941$ Å. From this table it can be seen that the five nearest neighbours to the RE site are all Platinum.

The $P\bar{6}2m$ structure is closely linked to the kagome lattice [9]. It is obtained from the ideal kagome structure by a small rotation of the RE triangular unit within a cell. This distortion is shown in diagram 2.3 below, where the RE

Species	Equivalents	$\mathbf{a}$ [Å]	$\mathbf{b}$ [Å]	$\mathbf{c}$ [Å]	Distance [Å]
Pt	4	$\frac{2}{3}$	$\frac{1}{3}$	0	2.99418
Pt	1	1	0	$\frac{1}{2}$	3.07258
In	2	0.25994	0	0	3.17509
In	4	1	0.25994	0	3.30898
RE	2	0.5941	0	$-\frac{1}{2}$	3.83807
RE	4	0	-0.4059	$-\frac{1}{2}$	3.98091

Table 2.2: *The distance to the neighbouring sites of the RE ion located at the $(x_{RE},0,\frac{1}{2})$, where $x_{RE} = 0.5941$. The columns $\boldsymbol{a},\boldsymbol{b},\boldsymbol{c}$ give the location of neighbour site. The 'Equivalents' are all the same distance and same species.*

triangles are highlighted in red. The link with the kagome lattice is emphasised, as this lattice has been extensively studied [11] [12] in relation to magnetic frustration, described in section 2.3.3.
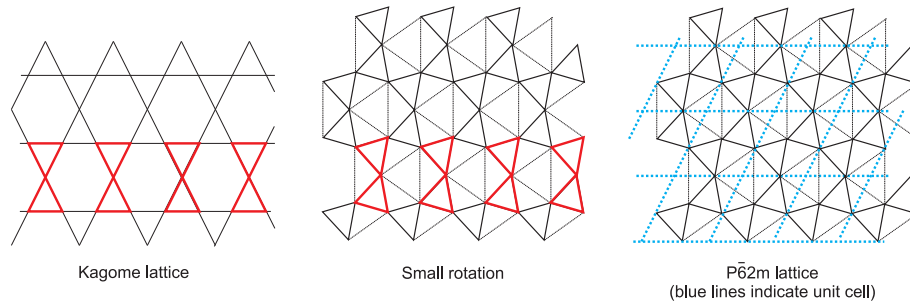
Figure 2.3: *The $P\bar{6}2m$ lattice is generated from the kagome lattice by a rotation of the equilateral triangle, highlighted in red.*

The nature of the $P\bar{6}2m$ structure gives the REPtIn series immediate potential for a lot of interesting physics. The geometry of equilateral triangles means that any in-plane antiferromagnetic magnetism would be frustrated. The nature of the Pt network around the RE ions means that they could be polarised by a Dzyaloshinskii-Moriya type interaction giving rise to a local magnetic moment away from the RE site. In addition to this the series is isostructural making the REPtIn compounds an excellent series for investigate the properties of 4f electron magnetism.

2.3 Magnetic Properties of the Rare Earth Elements

Generally, the order in which electronic shells fill does not solely depend on increasing the principle quantum number n. This is clearly seen in the RE elements, which fill the 4f shell across atomic numbers $57 \rightarrow 71$ having preferentially filled the 5s, 5p and 6s shells. These shells are 'closed', as no more electrons can have the same eigenenergy and still obey the exclusion principle. A closed shell has a total angular momentum of zero. The 14 electrons being added across the Rare Earth series fill the inner 4f shell in the most energetically favorable way. This means that any measured magnetic moment of a rare earth element is due to the inner 4f electron shell being partially filled. It is also possible that the conduction band electrons will be polarised. This usually gives rise to a much smaller magnetic moment.

In the REPtIn series the rare earth atom is generally trivalent (RE^{3+}). As the metallic bonding is with the outer electrons, the magnitude of the 4f magnetic moment is relatively unaffected. It is therefore informative to compare the measured moment in a REPtIn compound with that of the free RE ion. This can be calculated using Hund's rules discussed in section 2.3.1. It is also informative to compare the maximal ordered moment M_z of the free ion, to that observed in high magnetic fields below the magnetic ordering temperature.

2.3.1 Hund's Rules for the 4f Shell

The magnetic moment of the RE^{3+} ion in the REPtIn series is given by the total angular momentum, **J**. From the discussion above it is clear that it is only the 4f electrons that will contribute to **J** as all the other shells are closed. As such, we need only calculate **J** for the unfilled 4f electron shell. This is done using Hund's rules [15], which assume Russell Saunders coupling and that the different coupling energies scale as:

$$spin - spin\ coupling > orbit - orbit\ coupling > spin - orbit\ coupling$$

where the spin-orbit (L-S) coupling is the weakest interaction. With this energy scheme, Hund's rules are:

- The spin of each $\mathbf{S}_i$ should combine to give the maximum value of $\mathbf{S}$ possible in accordance with the Pauli exclusion principle.

- While obeying the first rule, give the maximum $|L|$

- If the shell is less than half full then $|J| = |L - S|$, or else $|J| = |J + S|$ if the shell is more than half full. If the shell is exactly half full then $L = 0$ and $\mathbf{J}=\mathbf{S}$.

Hund's rules give the relationship between magnetic moment and electron number. The effective paramagnetic moment is then given by $\mu_{eff} = g_J\sqrt{J(J+1)}$ where g_J is known as the Landé g-factor given as:

$$g_J = 1 + \frac{J(J+1) + S(S+1) + L(L+1)}{2J(J+1)} \qquad (2.3.1)$$

The effective moment for the RE^{3+} series is plotted in figure 2.4.
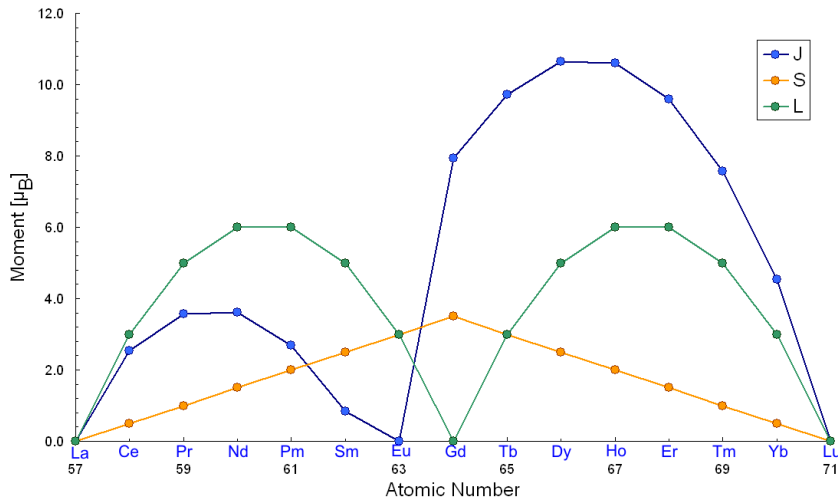
Figure 2.4: *The effective magnetic moment, $\mu_{eff} = g_J\sqrt{J(J+1)}$, of the RE^{3+} series given by Hund's rules. Experimentally this moment is compared to the effective paramagnetic moment measured.*

It should be noted that E.Balcar and S.Lovesey [16] argue that jj coupling is a better model for RE elements, although the literature is unclear for which atomic number (Z) one should use either L-S or jj coupling. In jj coupling the spin-orbit interaction is stronger, such that the spin and angular momentum quantum numbers are first added to form individual j_n values.

$$
\begin{aligned}
j_n &= \sum_{n\ electrons} s_n + l_n \\
\mathbf{J} &= \sum_{n\ electrons} \boldsymbol{j}_n
\end{aligned}
$$

However, it is possible to transform from the LS to jj coupled scheme using a unitary transformation.

2.3.2 The RKKY Interaction

The RKKY interaction [17] (named after its developers, Ruderman, Kittel, Kasuya and Yosida) describes long range spin correlations, where a standard overlap integral is not sufficient. It uses indirect exchange via the conduction electrons to produce a correlation of electronic spin between 4f electrons. Due to the localised nature of the 4f electrons direct exchange is weak making the RKKY indirect exchange dominant. This interaction is described using a Heisenberg-type hamiltonian, in which the kinetic energy of the conduction electrons is included. The coupling strength of the RKKY interaction oscillates with distance decaying to zero according to a power law. In real alloys this decay is also modulated by some function of the mean free path of the conduction electron. The general form of the exchange strength coefficient is given below in figure 2.5. From this it can be seen that the nature of magnetic order depends on the atomic distance between the Rare Earth atoms. In the REPtIn structure it is possible to get ferromagnetic interactions with nearest neighbours and antiferromagnetic interactions with next nearest neighbours.
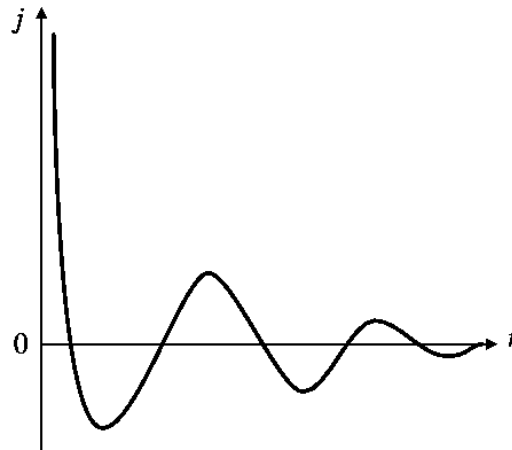
Figure 2.5: *The radial dependence of the RKKY exchange coefficient [18].*

2.3.3 Magnetic Frustration

Magnetic frustration [19] arises when there is no unique ground state. This is often seen when magnetic atoms occupy the corners of an equilateral triangle. The geometry of this situation means that the interaction energy, J, can not be simultaneously minimised for all antiferromagnetically coupled magnetic moments (see figure 2.6). This is seen in the REPtIn series as the RE^{3+} ions occupy the 3g site.
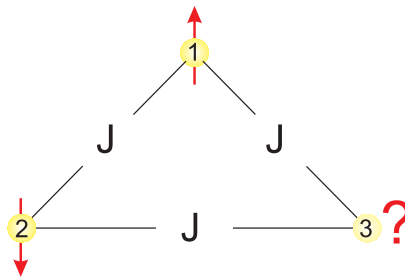
Figure 2.6: *A simple diagram showing geometric frustration. The magnetic moments (red) order along the easy-axis. Moment (1) orders antiferromagnetically with (2) minimising the interaction energy J. This causes 'frustration' as moment (3) can not simultaneously minimise its energy with (1) and (2).*

2.3.4 Canting

A non-collinear structure has its magnetic moment oriented away from a unique axis of magnetic alignment. A non-collinear structure is reported in many of the REPtIn alloys. For example, Baran *et al.* [1] implement a canted magnetic structure when modelling neutron powder diffraction data for HoPtIn and DyPtIn. Their work is discussed in detail in section 2.5. This model introduces a small antiferromagnetic component in the hexagonal plane creating a fan-like structure. Canting in the REPtIn alloys is still observed in high applied fields, where it would be reasonable to assume that the applied magnetic field would be strong enough to overcome any anisotropy aligning the moments along the field.

2.3.5 de Gennes Scaling

As previously described, it is the 4f wavefunctions, which give rise to the highly localised magnetic moment of a RE ion. Because of this, there is no overlap of the 4f wavefunction with a neighboring RE site. This means the onset of magnetic order can not be due to direct exchange, but is due to an indirect ordering mechanism, such as the RKKY interaction. This allows the magnetic moment of a RE site to be correlated with its neighbours using the spin of the conduction electrons. An interaction mediated in this way will depend on the wavevector of the conduction electron and the magnitude of the coupling between the conduction electron spin, and the magnetic moment of the RE site. It can be shown, using a mean field approximation, that theoretical ordering temperature of RE compounds should be proportional to the *de Gennes* scaling factor. The de Gennes factor is given as [5]:

$$G = (g_J - 1)^2 J(J + 1) \qquad (2.3.2)$$

where J is the total angular momentum and g_J is the Landé g factor. This model assumes that the magnetic susceptibility of the conduction electron gas remains constant across the rare earth series. This assumption is valid for the REPtIn series.

Although this is an idealised model, experimental results are often in good agreement. The REPtIn series exhibits de Gennes scaling as seen in figure 2.7. The de Gennes scaling parameter does not indicate the nature of the magnetic order, but simply the transition temperature. This implies that the conduction band structure does not change across the series, and that any magnetic order mediated in this way would be similar in nature. This is curious, as the type of the magnetic order changes from antiferromagnetic for the Eu, Tb, Tm and Yb compounds to ferromagnetic for the Nd, Sm, Gd, Dy, Ho and Er compounds. This information on magnetic ordering temperature is tabulated in table 2.3 in the overview section at the end of this chapter.
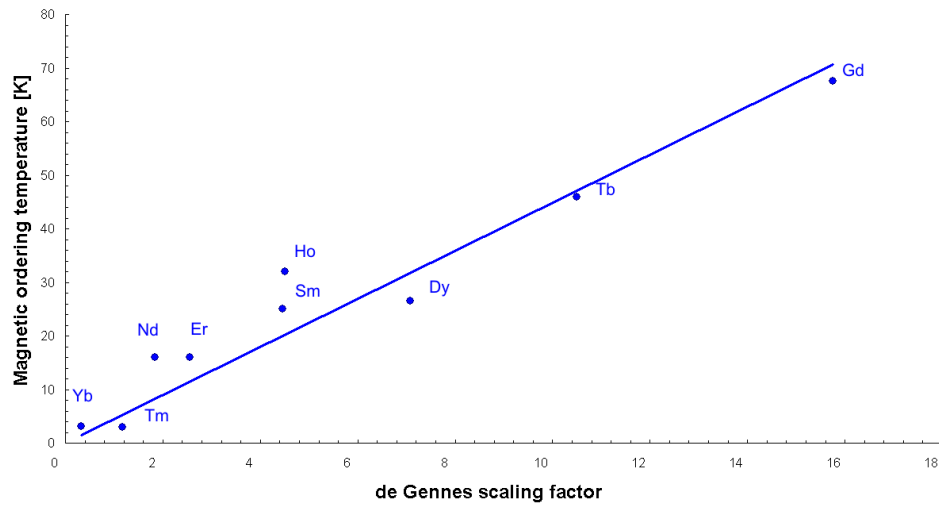
Figure 2.7: *Plot of the de Gennes scaling factor, $G = (g_J - 1)^2 J(J + 1)$, against the magnetic ordering temperature for some REPtIn alloys. The Rare Earth element label indicate the corresponding transition temperature. These values are reproduced in table 2.3 together with the reference from which the experimental value has been taken.*

2.4 Crystalline Electric Field Splitting

The crystalline electric field (CEF) is the electric potential generated by the array of ions that make up the crystal lattice. This is a non-homogeneous,

non-isotropic electric field with the same site symmetry as the RE lattice site. A free ion (i.e. where there is no perturbing potential or field applied) has full rotational symmetry and all electrons in the same sub-shell have the same energy [20]. When this ion is placed into a solid, the spherical symmetry will be reduced to the point-group symmetry of that site. This partially lifts the (2J+1) degeneracy. The strength of the energy spitting depends on the symmetry and strength of the crystal field.

The energy of the crystal field splitting has to be compared to the energy scales of the electron-electron interaction and that of the Russel-Saunders ($L-S$) coupling. For the 4f ions the energy scale of the crystal field is much less than that of spin orbit coupling. This allows us to treat the crystal field splitting as a perturbation of the $L-S$ coupling restricting any CEF model to the $|\mathbf{J}|$ manifold.

As the CEF is anisotropic, the energy splitting will give rise to an energetically preferred orientation for the magnetic moments. This will be observed experimentally, as the magnetic moment is restricted to an energetically preferential direction or plane. As such, this is either an easy-axis or an easy-plane magnet.

A CEF model for a given RE ion starts by considering the classical electric potential, which is added to the system Hamiltonian. This generally has the form

$$V_{CEF}(\mathbf{r}) = \int \frac{e\rho(\mathbf{R})}{|\mathbf{r} - \mathbf{R}|} d\mathbf{R} \qquad (2.4.1)$$

where $\rho(\mathbf{R})$ is the charge density of the surrounding electrons and ions. For the 4f electrons this can be expanded in terms of spherical harmonics up to $l = 6$, or using Racha algebra and Wigner coefficients. However, the mathematical procedure usually adopted is to use the so called "operator equivalent technique". Stevens [21] showed that 2.4.1 can be cast into a form that uses simple operators of the angular momentum components J_x, J_y, J_z provided we remain within a given J manifold. The operators act on a given state $|J, m_j >$ in the same way as the potential operator 2.4.1 does on x, y, z under the symmetry operations of the point group of the Wyckoff site. This means that the

matrix elements of V_{CEF} are proportional to those using the Stevens operators. The contribution of the CEF to the RE Hamiltonian then becomes

$$H_{CEF} = \sum_i \sum_{lm} B_l^m O_l^m(\boldsymbol{J}_i) \qquad (2.4.2)$$

where O_l^m are the Stevens operators [21]. For f-electrons these run to a maximum of $l = 6$. The Stevens operators are listed in figure 2.8 below.

$$O_2^2 = \frac{1}{2}(J_+^2 + J_-^2)$$

$$O_2^1 = \frac{1}{2}(J_z J_x + J_x J_z)$$

$$O_2^0 = 3J_z^2 - X$$

$$O_2^{-1} = \frac{1}{2}(J_z J_y + J_y J_z)$$

$$O_2^{-2} = \frac{1}{2i}(J_+^2 - J_-^2)$$

$$O_4^4 = \frac{1}{2}(J_+^4 + J_-^4)$$

$$O_4^2 = \frac{1}{4}\left[(7J_z^2 - X - 5)(J_+^2 + J_-^2) + (J_+^2 + J_-^2)(7J_z^2 - X - 5)\right]$$

$$O_4^0 = 35J_z^4 - (30X - 25)J_z^2 + 3X^2 - 6X$$

$$O_4^{-2} = \frac{1}{4i}\left[(7J_z^2 - X - 5)(J_+^2 - J_-^2) + (J_+^2 - J_-^2)(7J_z^2 - X - 5)\right]$$

$$O_4^{-4} = \frac{1}{2i}(J_+^4 - J_-^4)$$

$$O_6^0 = 231J_z^6 - (315X - 735)J_z^4 + (105X^2 - 525X + 294)J_z^2 \\ -5X^3 + 40X^2 - 60X$$

$$O_6^6 = \frac{1}{2}(J_+^6 + J_-^6)$$

Figure 2.8: *The Stevens operators used to evaluate CEF splitting within a J manifold. Note:* $X = J(J+1)$ *and* $J_\pm = J_x \pm iJ_y$ *[5].*

The B_l^m coefficients are usually determined from experiments, such as specific heat or inelastic neutron spectroscopy. They can also be calculated from polarised neutron data such as magnetisation density measurements.

2.5 REPtIn- A Literature Review

In this section the previous research on the theme compounds, HoPtIn and DyPtIn, will be reviewed. A brief outline of the REPtIn series as a whole is given. This is best illustrated with two further examples, GdPtIn, due to it having a half-full 4f shell, and with TbPtIn, a strong antiferromagnet with possible frustration effects.

2.5.1 Magnetic Properties of DyPtIn

Two research groups, namely Watson *et al.* [3] and Baran *et al.* [1] have magnetically characterised powder samples of DyPtIn using a SQUID magnetometer. In the paramagnetic regime the inverse susceptibility follows a simple Curie-Weiss law, with a paramagnetic Curie temperature of $T_{para}^{Dy} = 32$ K (Baran *et al.*). Both groups found DyPtIn to have a $T_c^{Dy} \sim 38$ K. Baran *et al.* reports an effective paramagnetic moment of $\mu_{eff} = 10.7\mu_B/$Dy, whereas Watson *et al.* calculates much less, $\mu_{eff} = 9.16\mu_B/$Dy. These should be compared to the effective free moment given by Hunds rules of $\mu_{eff}^{Hund} = 10.62\mu_B/$Dy.

Watson *et al.* extrapolated the spontaneous ferromagnetic moment at T = 0 K of $\mu_{sat} = 4.34\mu_B/$Dy, whereas Baran *et al.* measured $\mu_{sat} = 6.8\mu_B/$Dy at 1.7K, with both measurements being taken in a field of 5T. This should be compared to the maximal ordered moment of $\mu_{sat}^{calc} = 10\mu_B/$Dy. The reduction in the observed moment is speculatively attributed to CEF effects by Baran *et al.*.

Further to these powder studies Morosan *et al.* [2] have performed extensive single crystal work. They also measured $\mu_{eff} = 10.7\mu_B/$Dy for the effective paramagnetic moment, in agreement with Baran's powder work.

Morosan *et al.* determine $T_c^{Dy} = 26.5$ K using specific heat data. They attribute the large difference in T_c compared to Watson as the effects of measurement of a polycrystalline sample.

The direction dependent single crystal magnetisation investigation was carried out by Morosan *et al.* [2]. It shows strong anisotropy, which is characteristic of the REPtIn series. A 5.5 T field applied in the ab-plane at T=2K

gives a saturated magnetic moment of $\mu_{a-b} = 4.98\mu_B/\text{Dy}$. When the field is applied along the c-axis, a moment of $\mu_c = 6.88\mu_B/\text{Dy}$ is measured, which is in excellent agreement with measurements on powder samples. This indicates that the ferromagnetic ordering is an easy axis (c-axis) alignment. However, no explanation is offered as to why the moment is reduced compared to the free atom value. A plot of the magnetisation data taken by Morosan *et al.* [2] is reproduced in figure 2.9.
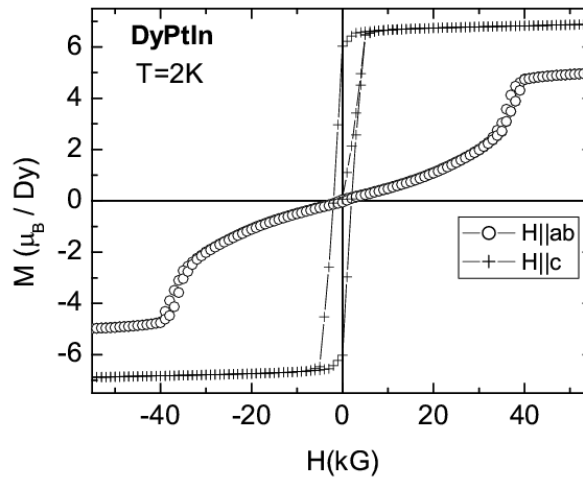
Figure 2.9: *Anisotropic, field dependent magnetisation hysteresis loops for DyPtIn at T=2K. From [2].*

Baran *et al.* [1] have performed neutron diffraction measurements at two temperatures, T=50 K and T=1.5 K with good quality samples. The low temperature data shows new magnetic peaks at low angles, which were fitted using two different magnetic phases. The first phase is ferromagnetic with the moment orientated along the c-axis and with a magnetic moment of magnitude $\mu_c^{neutron} = 6.6\mu_B/\text{Dy}$. The second phase is located within the the ab-plane and is anti-ferromagnetic in nature with a propagation vector of $\boldsymbol{k} = [\frac{1}{2}, 0, \frac{1}{2}]$. The magnitude of the moment within the a-b plane is refined to be $\mu_{a-b}^{neutron} = 4.9\mu_B/\text{Dy}$. They achieve a very good fit to the data, reporting a $\chi^2 = 2.82$. This model allows the moments to cant away from the c-axis, which is refined to be $\theta = 37\,\text{deg}$. The total moment is the vector sum of the ab-plane

and c-axis components, and is given as $\mu_{total}^{neutron} = 8.2\mu_B/\text{Dy}$. As the observed moment is much lower than the expected maximal moment, this could indicate that the wrong model has been implemented. A model that allows the moment to be free to cant away from its easy-axis should be checked against symmetry requirements for the magnetic point group. The authors do not comment whether this symmetry analysis was performed. This is examined in chapter 4, where the results from neutron scattering from powdered samples is reported. The antiferromagnet structure is reproduced in figure 2.10. Baran *et al.* attribute this effect to CEF splitting, but they do not attempt to evaluate any of the B_l^m coefficients.
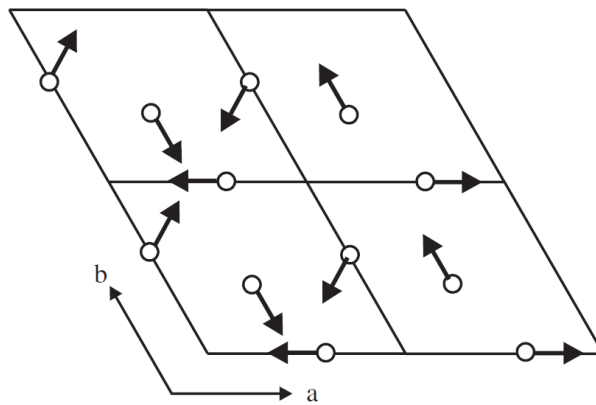
Figure 2.10: *Antiferromagnetic component of the model used to fit 1.6 K neutron data taken by Baran et al. for DyPtIn [1].*

Both Morosan *et al.* [2] and Baran *et al.* [1] comment that there are points of inflection in the temperature dependent magnetisation data. Baran *et al.* report that the zero-field cooled curve has two maxima at 17.9 K and 7.3 K. Baran *et al.* speculate that this indicates a two-step magnetic transition, the first being ferromagnetic and the second being the antiferromagnetic component seen in the neutron diffraction, which onsets below T=17.9 K. Further work would be required to ascertain the exact temperature dependence of the magnetic transitions.

2.5.2 Magnetic Properties of HoPtIn

HoPtIn was also investigated by Morosan *et al.* [2] and Baran *et al.* [1]. Morosan used single crystals grown in indium flux to measure the anisotropic magnetic properties up to 5.5T. As seen for the DyPtIn compound, the paramagnetic phase is Curie-Weiss like with an effective moment of $\mu_{eff} = 10.5\mu_B$/Ho. This effective moment is close to that given by Hunds rules, $\mu_{eff}^{Hund} = 10.6\mu_B$/Ho. Below $T_c = 23.5$ K (Morosan *et al.*) HoPtIn is a strong ferromagnet showing similar anisotropy compared to DyPtIn. The maximum ordered moment measured at T=2 K and 5.5T along the c-axis is $\mu_c = 7.81\mu_B$/Ho having saturated at a relatively low field of $\sim$ 1T. The magnetisation in the basal plane does not appear to saturate in a field of 5.5 T, reaching a maximum value of $\mu_{ab} = 4.3\mu_B$/Ho at T=2 K. Neither of these values are close to the theoretical maximally ordered moment of $\mu_{sat}^{calc} = 10\mu_B$/Ho. Strong anisotropy is present up to fields of 5.5 T with $\mu_c > \mu_{ab}$.

Baran *et al.* [1] report on neutron diffraction measurements at two temperatures, 1.5K and 40K. The 40 K data is modelled excellently with a single phase and no apparent impurities. As with the DyPtIn data, the diffraction pattern is refined with a canted structure, which uses an antiferromagnetic in-plane phase. This is again modelled using a propagation vector of $\boldsymbol{k} = [\frac{1}{2}, 0, \frac{1}{2}]$. The magnitude of the moment within the a-b plane is refined to be $\mu_{a-b}^{neutron} = 3.5\mu_B$/Ho with the moment along the c-axis being $\mu_c^{neutron} = 7.4\mu_B$/Ho at T=1.5 K. The magnitude of the magnetic moment at 2K is $\mu_{total}^{neutron} = 8.2\mu_B$/Ho, substantially less than that predicted. The angle between the c-axis and the magnetic moment is refined to be $\theta = 35°$.

Whilst Baran's model seems to give a good fit with a low $\chi^2 = 8.59$, it should be noted that there is clearly a non-indexed magnetic peak at $2\theta \sim 40\,$deg, as seen in figure 2.11. The authors do not comment on this.
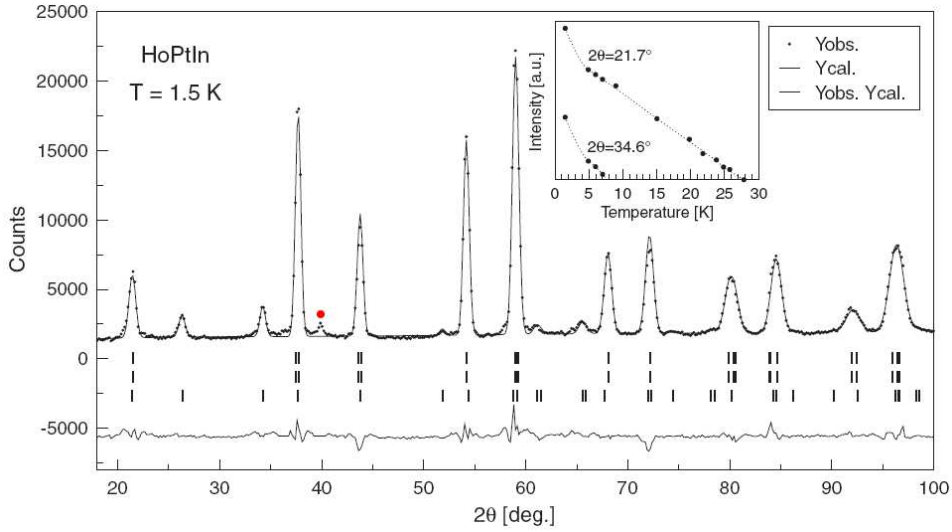
Figure 2.11: *Neutron diffraction pattern of HoPtIn at T=1.5 K. Note the non-indexed magnetic peak at $\sim 40 \deg$, marked with a red circle in the figure. From [1].*

The onset of magnetic order again seems to be multi-staged, as in DyPyIn. Baran plots the temperature dependence of two peaks at $2\theta = 21.7 \deg$ and $2\theta = 34.6 \deg$. This can be seen in the small insert within figure 2.11. Baran concludes that the $2\theta = 21.7 \deg$ peak is composed of both the ferromagnetic and antiferromagnetic contributions, whilst the $2\theta = 34.6 \deg$ is purely antiferromagnetic. This indicates that the antiferromagnetic phase is only present below T=8 K, below which the magnetic moments cant away from the c-axis. The $2\theta = 21.7 \deg$ appears at T=27 K indicating the Curie temperature.

Stephens *et al.* [4] used the phonon blank technique to separate the magnetic contribution to the specific heat. This data clearly shows the onset of magnetic order at $T_c \sim 33$ K, which is in disagreement with that reported by Morosan *et al.* [2] and Baran *et al.* [1]. The magnetic contribution to the specific heat is shown in figure 2.12. The sharp peak at T=7 K indicates the onset of a second magnetic phase, which supports the findings of Baran *et al.* [1]. The current research on HoPtIn has not yet yielded a satisfactory answer to the question of reduced ordered moment, and the highly anisotropic
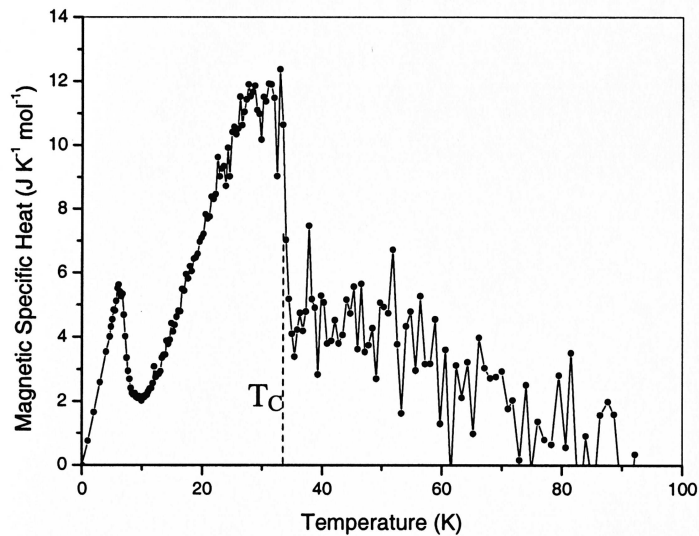
Figure 2.12: *The magnetic contribution to the specific heat for HoPtIn showing two peaks at $T_c = 33$ K and T=7 K [4].*

nature of the magnetic system. To explain these characteristics an appropriate theoretical model still needs to be developed.

2.5.3 Characteristics of the REPtIn Series

The REPtIn series as a whole exhibits some general characteristics and intriguing physics. Those that order magnetically seem to have a reduced ordered moment, despite measuring most of the free moment in the paramagnetic regime. To illustrate this general trend figure 2.13 has been produced. Figure 2.13 shows the size of the magnetic moment measured as a *percentage* of that expected for the ordered moment. This value can then be compared to the size of the effective moment measured in the paramagnetic regime, also displayed as a percentage of that expected from Hund's rules. As the reported values for these measurement vary, care has been taken to cite the source from which the values were taken. These values are recorded in table 2.3, which requires a KEY (table 2.4) to explain the notation used.
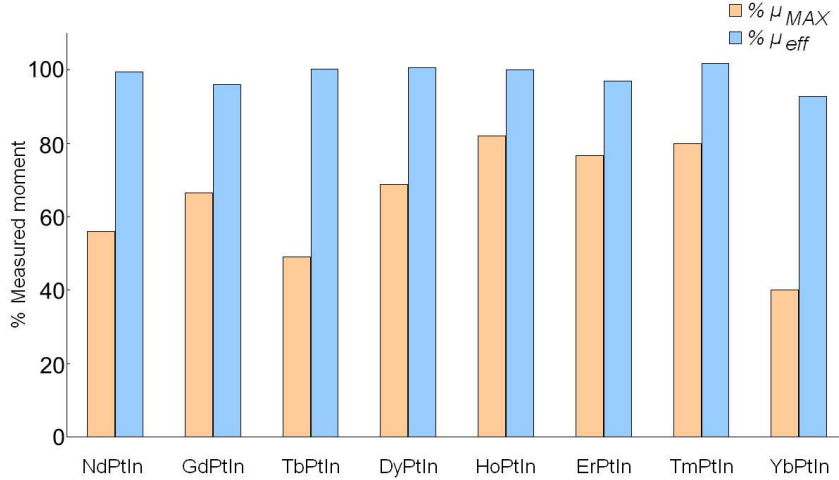
Figure 2.13: *Chart showing the percentage of the ordered magnetic moment (orange) and the percentage of the effective moment experimentally measured (blue). The values used for this plot come from table 2.3, the citations for the $\%\mu_{eff}$ data are: Nd[22][N], Sm[23][M], Gd[2][M], Tb[3][M], Dy[2][M], Ho[1][M], Er[24][M], Tm[25][N], Yb[26][M]. The citations for the $\%\mu_{MAX}$ data are: Nd[22][MS], Gd[2][MS], Tb[6][MS][Avg], Dy[1][MS], Ho[1][MS], Er[24][MS], Tm[2][MS], Yb [26][MS]*

.

On examination of figure 2.13 the reduction in ordered moment is immediately clear. For the eight compounds displayed nearly 100% of the effective moment is observed from magnetic susceptibility results (blue). However, once the REPtIn compound orders magnetically, this moment is greatly reduced. The reduction in moment ranges from $\sim 20\%$ (HoPtIn) to $\sim 60\%$ (YbPtIn). This effect is as yet unexplained in the literature.

One hypothesis [4] is that the RE moments induce a moment on the Pt site. The Pt site is located at the centre of the equilateral triangle made up of RE ions. This triangle does not have a point of inversion. This could feasibly give rise to a Dzyaloshinskii-Moriya interaction for which the induced moment is correlated to that of the RE site. This type of induced moment can be detected using spin polarised neutrons and a high quality single crystal to construct a magnetisation density map.

Another general feature of the REPtIn series is the strong magnetic anisotropy. The moments are not readily saturated even in high fields, if at all. The anisotropy observed is often attributed to the CEF, but no group has attempted to determine the crystal field coefficients. This explanation is problematic, as strong anisotropy is also observed in the compound GdPtIn. GdPtIn has a half-filled 4f shell ($L = 0$), which is spherically symmetric. A spherically symmetric shell does not have a preferred orientation, so there should be no anisotropy and the shell remains degenerate [5]. This is clearly not the case on inspection of figure 2.14 which shows single crystal magnetisation data, measured by Morosan *et al.* [2]. The strong anisotropy is present up to applied field strengths of 4 Tesla. This indicates that there are magnetic correlations with an energy scale exceeding that usually attributed to CEF splitting. For example, a saturated moment of $6.8\mu_B$ within a field of 4 Tesla has a potential energy of ~ 1.57 meV, which corresponds to a temperature of $17K$. The ordering temperature for GdPtIn is $T_c = 74K$, which is over four times their anisotropy values. Morosan *et al.* [2] discuss a model whereby the easy-axis is [1 2 l] direction, although comment that this has limited applicability to GdPtIn.
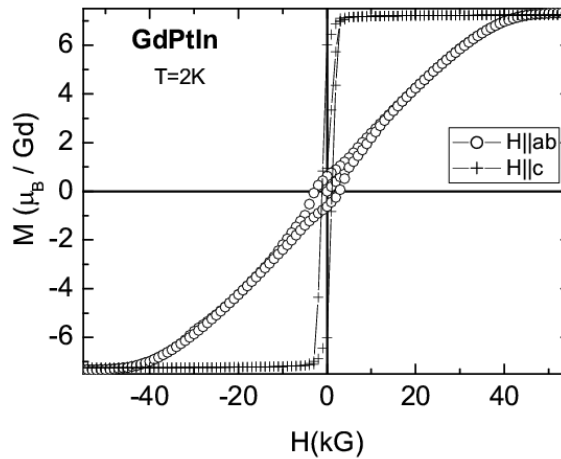
Figure 2.14: *Anisotropic, field dependent magnetisation hysteresis loops for a single crystal sample of GdPtIn at T=2K [2].*

2.5.4 Summary of Background and Motivation

In this chapter the interesting physics observed in the REPtIn series has been introduced. Despite this series being the subject of focus for several research groups, for many years no adequate explanation for the results reported has been put forward. In fact the problem seems to deepen with every new measurement. At the time of starting this PhD research there were seven clear question for the RePtIn series that require further experimental study. These are:

1. What mechanisms give rise to magnetic order in the REPtIn compounds? The fact that they follow de Gennes scaling implies a conduction band mediated correlation, but the magnetic order randomly switches between antiferromagnetic and ferromagnetic.

2. What mechanism causes the reduction in ordered moment seen across the series?

3. What mechanism relieves the magnetic frustration in the antiferromagnetic compounds?

4. What is the extent of the CEF splitting for the RE^{3+} ion?

5. What mechanism causes the strong magnetic anisotropy measured?

6. Is the magnetism localised on the RE^{3+} site or could the complex RE-Pt structure induce magnetisation elsewhere?

7. In the compounds that show a multi-stepped magnetic order, what is the temperature dependence of this ordering mechanism? Also, are the order parameters for these steps independent or coupled?

These questions were the focus of the work undertaken for this PhD. It was decided to first tackle questions 6 and 7. As the antiferromagnetic compounds are likely to be the most complex, it is logical to start this process with some ferromagnetic compounds. Specifically, these problems were investigated by

solving the magnetic structure for DyPtIn and HoPtIn using both powder and single crystal neutron scattering, which is the research presented in this thesis.

For DyPtIn and HoPtIn the magnetic ordering seems to be a two-step process where two order parameters are involved. To model this transition new experimental results were required for these compounds as they go through their magnetic ordering temperatures. This is best achieved using neutron diffraction measurements of powder samples at several temperatures. Neutron diffraction data can be analysed to extract important parameters, such as unit cell dimensions, unit cell volume and atomic positions. From these measurements it is possible to determine the magnetic structure using symmetry analysis. It would also be possible to check the propagation vector proposed by Baran *et al.* and check their magnetic model. The hot neutron diffractometer D20 [27] at the ILL[1] was selected for this initial study. The results and conclusions are reported in chapter 4. Before these results are presented, it is important to introduce the physics behind neutron scattering from crystalline solids, and to explain how the neutron interacts with a magnetic moment. This is discussed in the next chapter, which is self-contained but will be referred to throughout this remainder of this thesis.

2.5.5 Tabulation of Results for the REPtIn Series.

The final section of this chapter presents table 2.3, in which the experimental findings of many authors have been amalgamated. This is designed to illustrate the variety in ordering temperatures reported for the REPtIn series. This table contains the source of the reported result as a citation next to the value quoted. Further to this, the method with which the measurement has been taken, can be seen with the aid of the KEY, which is given in table 2.4.

---

[1]Institut Laue-Langevin, Grenoble, France

REPtIn	Magnetic Order	θ_{para} [K]	T_C or T_N [K]	μ_{eff} [μ_B]	μ_{MAX} [μ_B]	μ_{eff}^{Theory} [μ_B]	μ_{MAX}^{Theory} [μ_B]
LaPtIn	nm	-	-	-	-	0	0
CePtIn	pm	-73 [28]^{MS}	-	2.58 [28]^{MS}	-	2.54	2.14
PrPtIn	pm	-29 [23]^{MS}	-	3.53 [23]^{MS}	-	3.58	3.20
NdPtIn	fm	17 [22]^{MS}	16 [22]^{M}	3.6 [22]^{MS}	1.8 [22]$^{N}_{c}$, 0.35 [22]$^{N}_{ab}$	3.62	3.27
SmPtIn	fm	-	25 [23]^{M}	-	0.2 [23]^{M}	0.84	0.71
GdPtIn	fm	-	89 [3]^{M}, 67.5 [2]^{Cp}	6.82 [3]^{MS}, 7.62 [2]^{MS}	4.66 [3]^{M}, 7.0 [2]^{M}	7.94	7.00
TbPtIn*	afm	39 [6]$^{MS}_{ab}$, 23.3 [6]$^{MS}_{c}$, 49.5 [3]^{MS}	46 [6]$^{M}_{ab}$,	9.74 [6]$^{MS}_{Avg}$, 8.31 [3]^{MS}	5.86 [6]$^{M}_{110}$, 6.45 [6]$^{M}_{120}$, 0.92 [6]$^{M}_{001}$, 4.42 [3]^{M}	9.72	9.00
DyPtIn	fm	32.8 [1]^{MS},	37.1 [1]^{M}, 38 [3]^{M}, 26.5 [2]^{Cp}	10.7 [1]^{MS}, 9.16 [3]^{MS}, 10.7 [2]^{MS}	6.8 [1]^{M}, 4.34 [3]^{M}, 6.88 [2]$^{M}_{c}$, 4.98 [2]$^{M}_{ab}$	10.63	10.00
HoPtIn	fm	25.0 [1]^{MS},	23.1 [1]^{M}, 27.2 [1]^{N}, 23.5 [2]^{Cp}	10.6 [1]^{MS}, 10.5 [2]^{MS}	8.2 [1]^{M}, 7.81 [2]$^{M}_{c}$, 4.3 [2]$^{M}_{ab}$	10.6	10.00
ErPtIn	fm	13.3 [24]^{MS}	15.0 [24]^{M}, 13.1 [24]^{N}, 8.5 [2]^{Cp}, 16 [22]^{N}	9.3 [24]^{MS}, 10.1 [2]^{MS}	6.9 [24]^{M}, 6.2 [24]^{N}, 7.5 [2]$^{M}_{c}$, 2.77 [2]$^{M}_{ab}$	9.59	9.00
TmPtIn	afm	6.5 [25]^{MS}	3.5 [25]^{Cp}, 3.0 [2]^{Cp}	7.65 [25]^{MS}, 7.7 [2]^{MS}	4.5 [25]^{M}, 5.59 [25]^{N}, 2.26 [2]$^{M}_{c}$, 4.42 [2]$^{M}_{ab}$	7.57	7.00
YbPtIn	afm	-16 [26]^{MS}	1.7 [26]^{M}, 3.1 [26]^{Cp}, 3.4 [29]$^{M}_{ab,c}$	4.21 [26]^{MS}, 4.3 [2]^{MS}	1.6 [26]^{M}	4.54	4.00
LuPtIn	nm	-	-	0	-	0	0

Table 2.3: *A summary of magnetic data reported in the literature for the REPtIn series. Please see the key, table 2.4, on the next page for further information. *The TbPtIn magnetisation values used field up to 14T.*

Column	Title	Description
3	'θ_{para}'	The paramagnetic ordering temperature, extrapolated from inverse susceptibility data.
4	'T$_C$ or T$_N$'	The Curie or Néel ordering temperature.
5	'μ_{eff}'	The effective moment in paramagnetic region, calculated from the inverse susceptibility.
6	'μ_{MAX}'	The maximal ordered moment. Note some authors extrapolate this value to T=0 K, while others report this value at T=2 K.
7	'μ_{eff}^{Theory}'	The theoretical free moment, given by Hunds rules.
8	'μ_{MAX}^{Theory}'	The maximal ordered moment, given by $g_J J$.

Subscript	Superscript	Measurement detail.
	MS	Magnetic susceptibility.
	Cp	Specific heat.
	N	Neutron data.
	MS	Magnetisation.
c		Single crystal measurement taken along the c-axis.
ab		Single crystal measurement taken in the ab plane.
[h,k,l]		Single crystal measurement taken in the [h,k,l] direction.
Avg		An average value has been taken by the cited author.

Table 2.4: *KEY for table 2.3*

Chapter 3

Theory of Neutron Scattering

3.1 Introduction

As neutron scattering experiments form the bulk of this thesis, a background section is now included discussing scattering theory strictly relevant to the measurements taken. This is particularly important for the form factor analysis performed in section 5, for which the 'multipole expansion' introduced in section 3.4.3 is used.

Neutron scattering experiments utilise the intrinsic properties of the neutron to probe matter. A neutron has zero net charge, so it is not scattered by the atomic electrostatic potential. Scattering occurs via strong nuclear forces, which have a range of $\sim 10^{-15}$ m. The neutron's mean free path is relatively long for most solids, so scattering is 'weak' allowing the bulk properties of a sample to be measured. As the interaction is weak, most theory to describe scattering is based on perturbation theory, usually restricted to a first order approximation.

The neutron is a fermion with a spin-$\frac{1}{2}$ resulting in a magnetic moment. This gives rise to magnetic scattering from partially filled electronic orbitals. Expressions for the nuclear and magnetic neutron scattering will be discussed in the following sections.

3.2 Scattering Cross-Sections

A scattering experiment is set up as shown in figure 3.1 with the incident neutrons having wavevector $\mathbf{k_i}$ and those having been scattered from the target having a wavevector $\mathbf{k_f}$.
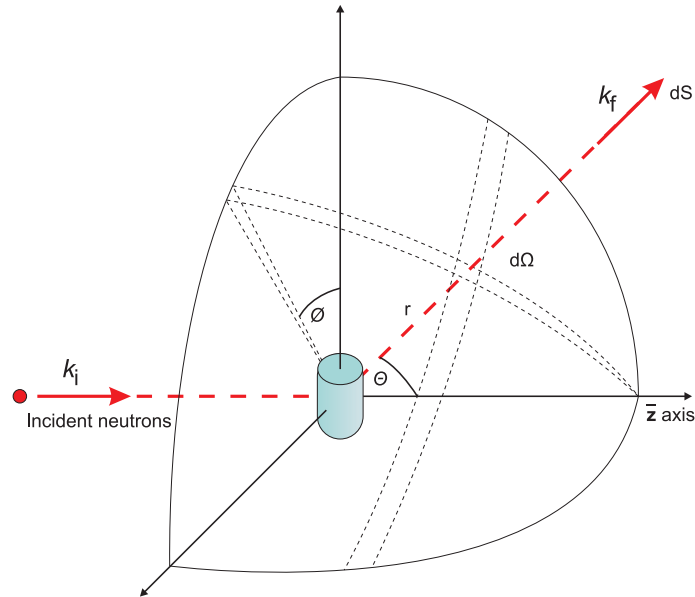
Figure 3.1: *T*he coordinate system for a neutron scattering experiment. The neutron beam is incident on the target with the wavevector $\boldsymbol{k_i}$ parallel to the z axis.

A detector at a given set of angles (Θ, ϕ) and a distance r away from the sample will count the scattered neutrons. This quantity is dependent on the incident flux, Φ, the area of the detector and the energy of the incident and scattering neutrons. To quantify the absolute scattering power of a sample we

define the differential scattering cross section to be:

$$\frac{d\sigma}{d\Omega} = \frac{\text{number of neutrons scattered per second into the solid angle } d\Omega}{\Phi \, d\Omega}$$

(3.2.1)

which is clearly independent of incident flux or detector area as we have divided through by these quantities. A similar cross section is defined when the energy is also analysed, for example in inelastic or time-of-flight experiments:

$$\frac{d^2\sigma}{d\Omega dE'} = \frac{\substack{\textit{number of neutrons scattered per second into the} \\ \textit{solid angle } d\Omega \textit{ with energy in the range } E' \mapsto E' + dE'}}{\Phi \, d\Omega dE'}$$

(3.2.2)

A single scattering event induces a transition in the system from a state labelled λ to one labelled λ'. The initial and final states of the scattering body may be identical, in which case $\lambda = \lambda'$. The scattering event is described by an interaction potential V. As such, the *'number of neutrons scattered per second into the solid angle $d\Omega$'* is the sum of all scattering processes that result in a final wavevector, $\mathbf{k_f}$, in the direction of $d\Omega$ per second. This is:

$$\left(\frac{d\sigma}{d\Omega} \right)_{\lambda \to \lambda'} = \frac{1}{\Phi \, d\Omega} \sum_{\mathbf{k_f} \ in \ d\Omega} W_{\mathbf{k_i}, \lambda \to \mathbf{k_f}, \lambda'}$$

(3.2.3)

The sum of these processes is equal to the probability of the system going to a given state, multiplied by the density of states. This is described within perturbation theory and it is then known as Fermi's golden rule:

$$\sum_{\mathbf{k_f} \ in \ d\Omega} W_{\mathbf{k_i}, \lambda \to \mathbf{k_f}, \lambda'} = \frac{2\pi}{\hbar} p_{\mathbf{k_f}} \left| < \mathbf{k_i}, \lambda \mid V \mid \mathbf{k_f}, \lambda' > \right|^2$$

(3.2.4)

the density of states, $p_{\mathbf{k_f}}$, is derived via box-normalisation as the neutron is in an unbound state. By substitution of 3.2.4 into 3.2.3 the partial differential cross section becomes:

$$\left(\frac{d\sigma}{d\Omega} \right)_{\lambda \to \lambda'} = \frac{k'}{k} \left(\frac{m}{2\pi\hbar^2} \right)^2 \left| < \mathbf{k_i}, \lambda \mid V \mid \mathbf{k_f}, \lambda' > \right|^2$$

(3.2.5)

where m is the neutron mass. The next step is to formulate an expression for

the potential V. This is dependent on the type of scattering being considered. In the next section two types of scattering, nuclear and magnetic, are discussed, which lead to very different matrix elements.

3.3 Elastic Nuclear Scattering

The first approximation is to treat V as a point-like potential, from which the neutron is isotropically scattered. This is s-wave (spherical) scattering giving the scattered neutron a wavefunction with the general form:

$$\psi_s = -\frac{b}{r}e^{ikr} \tag{3.3.1}$$

b is called the scattering length and is an experimentally determined quantity. It is a characteristic physical property of the scattering nucleus fully parameterising the scattering. It does not depend on angle and can be either real or complex. A complex component to b represents the absorption of neutrons to form a compound nucleus. Continuing this approximation, the potential V is assumed to be very short range allowing a three dimensional delta function to be used at the nuclear position. This is known as the Fermi pseudopotential and it is derived to be:

$$V(r) = \frac{2\pi\hbar^2}{m}\sum_i b_i\delta(\boldsymbol{r} - \boldsymbol{R_i}) \tag{3.3.2}$$

For elastic scattering, the initial and final states of the system are equivalent in energy, and $|\mathbf{k_i}| = |\mathbf{k_f}|$. As such, 3.2.5 becomes:

$$
\begin{aligned}
\frac{d\sigma}{d\Omega} &= \left(\frac{m}{2\pi\hbar^2}\right)^2 |< \mathbf{k_i} \mid V \mid \mathbf{k_f} >|^2 \\[2mm]
&= \left(\frac{m}{2\pi\hbar^2}\right)^2 \left|< \mathbf{k_i} \mid \frac{2\pi\hbar^2}{m} \sum_i b_i \delta(\mathbf{r} - \mathbf{R_i}) \mid \mathbf{k_f} >\right|^2 \\[2mm]
&= \left|< e^{-i\mathbf{k_f}\cdot\mathbf{r}} \mid \sum_i b_i \delta(\mathbf{r} - \mathbf{R_i}) \mid e^{i\mathbf{k_i}\cdot\mathbf{r}} >\right|^2 \\[2mm]
&= \left|\sum_i b_i \int_{all\ r} e^{-i\mathbf{k_f}\cdot\mathbf{r}} \mid \delta(\mathbf{r} - \mathbf{R_i}) \mid e^{i\mathbf{k_i}\cdot\mathbf{r}} dr\right|^2 \\[2mm]
&= \left|\sum_i b_i e^{i\boldsymbol{\kappa}\cdot\mathbf{R_i}}\right|^2
\end{aligned}
$$

here $\boldsymbol{\kappa}$ is the scattering vector defined by $\boldsymbol{\kappa} = \mathbf{k_f} - \mathbf{k_i}$, $\mathbf{R_i}$ is the position of the ith nucleus. Clearly the intensity at the detector is dependent on the scalar product $\boldsymbol{\kappa} \cdot \mathbf{R_i}$. This can be manipulated into a form consistent with definitions in crystallography. As $\mathbf{R_i}$ is the position of the ith nucleus, the function $\sum_i b_i\, e^{i\boldsymbol{\kappa}\cdot\mathbf{R_i}}$ has the periodicity of the crystal lattice. It can be split into $\mathbf{R_i} = \mathbf{R_l} + \mathbf{r_a}$ where l labels a lattice point, and a labels the fractional coordinate of the atom in the unit cell. This is:

$$
\frac{d\sigma}{d\Omega} = \left|\sum_{\substack{atoms\ in\\ unit\ cell}} b_a e^{i\boldsymbol{\kappa}\cdot\mathbf{r_a}} \times \sum_{lattice} e^{i\boldsymbol{\kappa}\cdot\mathbf{R_l}}\right|^2 \tag{3.3.3}
$$

The second summation over lattice points gives the geometric scattering conditions. From [30] this can be re-written as

$$
\left|\sum_{lattice} e^{i\boldsymbol{\kappa}\cdot\mathbf{R_l}}\right|^2 = N\frac{(2\pi)^3}{V} \sum_{\mathbf{G}_{hkl}} \delta(\boldsymbol{\kappa} - \mathbf{G}_{hkl}) \tag{3.3.4}
$$

where V is the unit cell volume. Clearly constructive interference will only occur when $\boldsymbol{\kappa}$ equals a reciprocal lattice vector, $\mathbf{G}_{hkl}$ This is equivalent to

Bragg's law. This does not, however, give any information on the intensity of the Bragg reflection. This is described by the first summation in equation 3.3.3 and is known as the *structure factor*.

The structure factor determines the intensity of a specific (hkl) reflection. It is usually defined as $F(\boldsymbol{\kappa})$ and contains all the information on the relative atomic positions of different species within the unit cell. If one writes the location of the atoms within the unit cell in terms of their position from the origin, then the structure factor becomes:

$$
\begin{aligned}
F(\boldsymbol{\kappa}) &= \sum_{\substack{atoms\ in \\ unit\ cell}} b_a e^{i\boldsymbol{\kappa}\cdot\boldsymbol{r_a}} \\
&= \sum_{\substack{atoms\ in \\ unit\ cell}} b_a e^{i2\pi(hx+ky+lz)}
\end{aligned}
$$

In a real scattering experiment it is important to modify this expression to include other physical processes. The temperature induced motion of the scattering center is described by the Debye-Waller factor, which models the thermal vibration of the nucleus. This has the form $e^{-2W(\boldsymbol{\kappa})}$. Corrections for absorption (T) and extinction (E) are also required, especially in single crystal diffraction. These corrections can be inserted into the expression for the differential cross section as:

$$
\frac{d\sigma}{d\Omega} = N\frac{(2\pi)^3}{V} \sum_{\mathbf{G}_{hkl}} \delta(\boldsymbol{\kappa} - \mathbf{G}_{hkl}) \left| F(\mathbf{G}_{hkl}) \right|^2 \; E \; T \; e^{-2W(\boldsymbol{\kappa})} \tag{3.3.5}
$$

For a more complete derivation of these quantities see Lovesey [30], Squires [31], or books on fundamental crystallography, for example C. Giacovazzo *et al.* [32].

3.4 Magnetic Scattering

Atoms with partially filled electronic shells have a permanent magnetic moment, as described in the magnetism section 2.3.1. A neutron is a spin-$\frac{1}{2}$ par-

ticle with its angular momentum described by the Pauli spin matrices. The incident neutron does not generate a magnetic field as its net charge is zero. Therefore the potential energy of the scattering event is that of the *electron cloud ↔ neutron moment* interaction.

The electronic distribution is described by the radial wavefunctions, which are generally found using self consistent numerical calculations, such as the Hartree Fock [33] method. The electronic wavefunctions for the atom is described by the *form factor*, which is discussed in the next section.

3.4.1   Spin in Matrix form

Any multi-electron wavefunction of an atom can be expressed as a sum of products of normalised, orthogonal eigenfunctions and complex coefficients, $\Psi = \Sigma c_n \psi_n$. The spin of a neutron is described as *spin up* or *spin down* with reference to a chosen axis of quantisation. Mathematically this is formulated in a two dimensional spin-space in which α and β are the basis vectors. These two dimensional vectors are orthonormal as $\alpha^T \alpha = \beta^T \beta = 1$ and $\beta^T \alpha = \alpha^T \beta = 0$ where:

$$\alpha = \begin{pmatrix} 0 \\ 1 \end{pmatrix}, \quad \beta = \begin{pmatrix} 1 \\ 0 \end{pmatrix}, \tag{3.4.1}$$

The spin operators describe the act of measuring the system, and are called the Pauli matrices. The three Pauli matrices plus the identity matrix are all linearly independent, so any spin wavefunction could be represented by a summation of the Pauli matrices. The Pauli matrices are:

$$\hat{\sigma}_I = \begin{pmatrix} 1 & 0 \\ 0 & 1 \end{pmatrix}, \quad \hat{\sigma}_x = \begin{pmatrix} 0 & 1 \\ 1 & 0 \end{pmatrix}, \quad \hat{\sigma}_y = \begin{pmatrix} 0 & -i \\ i & 0 \end{pmatrix}, \quad \hat{\sigma}_z = \begin{pmatrix} 1 & 0 \\ 0 & -1 \end{pmatrix} \tag{3.4.2}$$

Using these, the magnetic moments of a neutron and an electron are given by the following magnetic moment operators:

$$\hat{\boldsymbol{\mu}}_n = -\gamma \mu_N \hat{\boldsymbol{\sigma}} \quad \hat{\boldsymbol{\mu}}_e = -2\gamma \mu_B \hat{\boldsymbol{s}} \tag{3.4.3}$$

where μ_N and μ_B have their normal definitions. Further to this we can define the raising or lowering matrices. These are shown below and are important when considering spin-flip transitions.

$$\sigma^+ = \begin{pmatrix} 0 & 1 \\ 0 & 0 \end{pmatrix} \quad \sigma^- = \begin{pmatrix} 0 & 0 \\ 1 & 0 \end{pmatrix} \tag{3.4.4}$$

3.4.2 Magnetic Interaction Energy

As with nuclear scattering the state of the scattering body + neutron goes from $|\lambda, \mathbf{k_i} >$ to $|\lambda', \mathbf{k_f} >$. However, the polarisation of the scattered neutron may also change so the matrix element in 3.2.5 is modified to be:

$$< \lambda', \sigma_f, \boldsymbol{k_f} | V_M | \boldsymbol{k_i}, \sigma_i, \lambda > \tag{3.4.5}$$

The derivation of the magnetic interaction potential, V_M, requires some involved algebra for which Lovesey ([30], [34]) is followed. The potential V_M is the scalar product of the magnetic moment of the neutron with the magnetic field, $\mathbf{H}$, given by $V_M = -\hat{\boldsymbol{\mu}}_n \cdot \mathbf{H} = -\gamma \mu_N \hat{\boldsymbol{\sigma}} \cdot \mathbf{H}$. The evaluation of $\mathbf{H}$ can be split into two contributions. One from the electron spin and one from its orbital movement:

$$\begin{aligned} \mathbf{H_S} &= curl\left(\frac{\boldsymbol{\mu}_e \times \mathbf{R}}{|\mathbf{R}|^3}\right) \\ \mathbf{H_L} &= \frac{-e}{c}\left(\frac{\mathbf{v_e} \times \mathbf{R}}{|\mathbf{R}|^3}\right) \end{aligned} \tag{3.4.6}$$

where $\mathbf{R}$ is the vector distance from the electron to the point at which the interaction is evaluated. The electron velocity, $\mathbf{v_e}$, is derived from the $Id\mathbf{l}$ current element in the Biot-Savart law. Furthermore, these equations can be expressed in terms of the electron momentum operator, $\hat{\mathbf{p}_e}$:

$$\begin{aligned} V_M &= -\gamma\mu_N\hat{\boldsymbol{\sigma}} \cdot (\mathbf{H_S} + \mathbf{H_L}) \\ &= \gamma\mu_N\left(2\mu_B\hat{\boldsymbol{\sigma}} \cdot curl\left(\frac{\hat{\boldsymbol{s}} \times \hat{\mathbf{R}}}{|\mathbf{R}|^3}\right) - \frac{e}{2m_e c}\left(\hat{\mathbf{p}_e} \cdot \frac{\hat{\boldsymbol{\sigma}} \times \mathbf{R}}{|\mathbf{R}|^3} + \frac{\hat{\boldsymbol{\sigma}} \times \mathbf{R}}{|\mathbf{R}|^3} \cdot \hat{\mathbf{p}_e}\right)\right) \end{aligned}$$

This can be further manipulated into the form, for which the magnetic interaction operator $\hat{\mathbf{Q}}_\perp$ is defined, and the unit of magnetic scattering length, r_0, becomes apparent. Using this the partial differential cross section becomes:

$$
\begin{aligned}
\left(\frac{d^2\sigma}{d\Omega dE'}\right) &= \overbrace{\left(\frac{m}{2\pi\hbar 2}\right)^2 (2\gamma\,\mu_N\mu_B 4\pi)^2}^{r_0^2} \frac{k'}{k} \sum_{\sigma\sigma'\lambda\lambda'} p_\sigma p_\lambda \\
&\times\ < \sigma\lambda|(\hat{\boldsymbol{\sigma}}\cdot\hat{\mathbf{Q}}_\perp)^+|\sigma'\lambda' >< \sigma'\lambda'|(\hat{\boldsymbol{\sigma}}\cdot\hat{\mathbf{Q}}_\perp)|\sigma\lambda > \\
&\times\ \delta(E_\lambda - E_{\lambda'} + \hbar\omega) \qquad\qquad\qquad (3.4.7)
\end{aligned}
$$

with

$$
\hat{\mathbf{Q}}_\perp = \sum_i e^{\boldsymbol{\kappa}.\boldsymbol{r}_i}\left(\hat{\boldsymbol{\kappa}}\times(\boldsymbol{s}_i\times\hat{\boldsymbol{\kappa}}) - \frac{i}{\hbar\kappa}(\boldsymbol{p}_i\times\hat{\boldsymbol{\kappa}})\right) \qquad (3.4.8)
$$

where $\hat{\boldsymbol{\kappa}}$ is the unit scattering vector and the sum over $'i'$ is for the unpaired electrons of the scattering body. $\hat{\mathbf{Q}}_\perp$ is related to the magnetisation of the scattering system. It clearly only gives a contribution from magnetic components, which are perpendicular to the scattering vector $\boldsymbol{\kappa}$. By transforming the sum over r_i to an integral over r and after some further manipulation, the operator $\hat{\mathbf{Q}}_\perp$ is related to the real space magnetisation density $\mathbf{M}(\boldsymbol{r})$ by:

$$
\hat{\mathbf{Q}}_\perp = \frac{1}{2\mu_B}\int dr\ e^{\boldsymbol{\kappa}.\boldsymbol{r}}\left(\hat{\boldsymbol{\kappa}}\times(\mathbf{M}(\boldsymbol{r})\times\hat{\boldsymbol{\kappa}})\right) \qquad (3.4.9)
$$

The task now is to evaluate the $\hat{\mathbf{Q}}_\perp$ operator for each initial and final state and perform the weighted sum over all possible states. $\hat{\mathbf{Q}}_\perp$ is called the *magnetic interaction operator*, as it describes the scattering due to the fourier transform of the real-space magnetisation density. For RE atoms the calculation of $\hat{\mathbf{Q}}_\perp$ requires the evaluation of matrix elements of the type $< \theta JM|\hat{\mathbf{Q}}_\perp|\theta'J'M' >$ where θ stands for 'any other relevant parameters to fully describe the quantum state'.

To further develop $\hat{\mathbf{Q}}_\perp$ the radial part of the atomic electron distribution of the partially filled shell is needed. This has the general form:

$$
< j_K(\boldsymbol{\kappa}) >= \int_0^\infty |\Psi(\boldsymbol{r})|^2 j_K(\boldsymbol{\kappa}) \qquad (3.4.10)
$$

where $\Psi(\boldsymbol{r})$ is the electronic wavefunctions for the scattering shell found using self consistent calculations, like the Hartree-Fock method. $j_K(\boldsymbol{\kappa})$ are spherical bessel functions of order K. The electron distribution can be parameterized with an analytical approximation using seven coefficients, generally denoted A,a,B,b,C,c,D. The coefficients are tabulated in reference [35]. The analytical approximation has the form:

$$< j_K(\boldsymbol{s}) >= (Ae^{-a \cdot s^2} + Be^{-b \cdot s^2} + Ce^{-c \cdot s^2} + D)s^2 \qquad (3.4.11)$$

where $s = \frac{sin(\theta)}{\lambda}$. There is no need to multiply by s^2 for $K \neq 0$.

The order (K) to which the expansion is evaluated depends on the experimental setup and the nature of the results required. This is generally done in one of two ways: either the *dipole approximation*, or the *multipole expansion* are used. These methods are discussed in the next sections.

The four radial integrals for Ho^{3+} are plotted below in figure 3.2, along with the dipole approximation, discussed in section 3.4.4
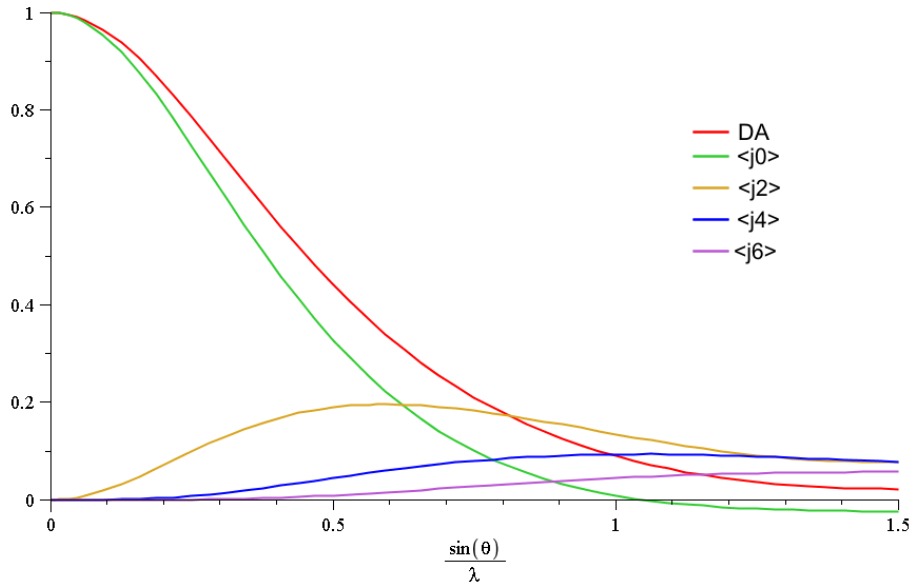
Figure 3.2: *The four radial integrals for Ho^{3+} with the dipole approximation (DA) plotted in red.*

3.4.3   Multipole Expansion

The multipole expansion can be calculated using different methods, but was shown by Lovesey and Rimmer [34] that it can be simplified by using the methods of Racha algebra, Clebsch Gordan coefficients and spherical harmonics.

The total angular momentum of a particle is composed of its orbital angular momentum, L, and its intrinsic spin, S. Any particle (or system) will have a total angular momentum, J, with a projection onto one 3-component axis given as M. The $(2J + 1)$ M values are the eigenvalues of the rotational group operators. If two systems, each with their own J (and M values) are coupled, the eigenstates of the coupled system can be found using Clebsch-Gordan coefficients.

Let the first system (1) have a total angular momentum j_1 and m_1 values ranging from $-j_1, -j_1 + 1, .., 0, .., j_1$. A second independent system is labelled with subscript '2'. Then the product states need to be found, $|j_1, m_1 > |j_2, m_2 >$, and the eigenvalues of the new product state be constructed. The final product state is labelled $|J, M, j_1, j_2 >$, and it is related to the product state by a Clebsch-Gordan coefficient, which is calculated for every unique combination of m_1, m_2. This is expressed as:

$$|J, M, j_1, j_2 >= \sum_{m_1 m_2} \underbrace{(j_1 \; m_1, j_2, m_2 | JM)}_{Clebsch-Gordan} \; |j_1, m_1 > |j_2, m_2 > \qquad (3.4.12)$$

and gives the eigenstates in $|J, M, j_1, j_2 >$ as a linear combination of the products of the subsystem states. To simplify notation the explicit j_1, j_2 dependance of the product state is omitted, and is shown as $|JM_J >$. The multipole expansion developed uses the Clebsch-Gordan coefficients and the methods of irreducible tensor algebra to describe the scattering event between momentum states of the scattering body, $|JM_J >$, and that of the neutron system. As such, the multipole expansion gives the full form of the electronic scattering distribution, over the whole range of $\boldsymbol{\kappa}$. This can be used to model the anisotropic magnetisation density which requires calculation of the probability coefficients for the angular momentum states. The coefficients are expressed

as:

$$|\lambda> = \sum_i \sum_M a_M |JM>_i \qquad (3.4.13)$$

where the explicit notation M_J is now simplified to M, and the sum over 'i' is for different RE sites. The determination of the a_M coefficients is performed by comparison to experiment. The determination of the a_Ms show which quantum states contribute to the magnetic moment. The standard normalisation condition applies, whereby $\sum_M |a_M|^2 = 1$. The multipole expansion is derived in chapter 11 of Lovesey [30], for which the matrix elements appearing in 3.4.7 become:

$$
\begin{aligned}
& < \theta J M | \hat{\mathbf{Q}}_{\perp,q} | \theta' J' M' > \\
= \; & < \theta J M | \sum_i e^{\boldsymbol{\kappa}.\boldsymbol{r}_i} \left(\hat{\boldsymbol{\kappa}} \times (\boldsymbol{s}_i \times \hat{\boldsymbol{\kappa}}) - \frac{i}{\hbar\kappa}(\boldsymbol{p}_i \times \hat{\boldsymbol{\kappa}}) \right)_q |\theta' J' M' > \\
= \; & (4\pi)^{\frac{1}{2}} \sum_{K''Q''} Y_{Q''}^{K''}(\hat{\kappa}) \sum_{K'Q'} [A(K''K') + B(K''K')] \\
& \times \; (K'Q'JM'|JM)(K''Q''K'Q'|1q) \qquad (3.4.14)
\end{aligned}
$$

where lower case q indexes the 3-component coordinate within a spherical harmonic basis. These are defined as $q = -1, 0, 1$ where $q = 0$ is the z-direction. The final two terms in rounded brackets are Clebsch Gorden coefficients given by

$$(j_1 m_1 j_2 m_2 | j_3 m_3) = (-1)^{j_2 - j_1 - m_3} \sqrt{2j_3 + 1} \begin{pmatrix} j_1 & j_2 & j_3 \\ m_1 & m_2 & -m_3 \end{pmatrix} \qquad (3.4.15)$$

where the entity in round brackets is a 3j symbol. These are derived in Condon

and Odabaşi [36] (p149) as:

$$
\begin{pmatrix}
j_1 & j_2 & j_3 \\
m_1 & m_2 & m_3
\end{pmatrix}
$$

$$
= (-1)^{j_1-j_2-m_3} \left[\frac{(j_1 + j_2 - j_3)!(j_2 + j_3 - j_1)!(j_3 + j_1 - j_2)!}{(j_1 + j_2 + j_3 + 1)!} \right]^{\frac{1}{2}}
$$

$$
\times \sum_\kappa (-1)^\kappa \frac{\sqrt{(j_1 + m_1)!(j_1 - m_1)!(j_2 + m_2)!}}{\kappa!(j_1 + j_2 - j_3 - \kappa)!(j_1 - m_1 - \kappa)!(j_2 + m_2 - \kappa)!}
$$

$$
\times \frac{\sqrt{(j_2 - m_2)!(j_3 + m_3)!(j_3 - m_3)!}}{(j_3 - j_2 + m_1 + \kappa)!(j_3 - j_1 - m_2 + \kappa)!} \qquad (3.4.16)
$$

This derivation allows the magnetic scattering due to the 2J+1 electronic energy levels to be calculated giving details of the CEF splitting and the nature of the magnetic anisotropy.

3.4.4 The Dipole Approximation

Within the dipole approximation, it is assumed that the scattering from the electron system is spherically symmetric, as the expansion only includes the first two radial integrals, $< j_0 >, < j_2 >$.

The operator $\hat{\mathbf{Q}}$, related to $\hat{\mathbf{Q}}_\perp$ by $\hat{\mathbf{Q}}_\perp = \hat{\boldsymbol{\kappa}} \times (\hat{\mathbf{Q}} \times \hat{\boldsymbol{\kappa}})$, is shown below using the dipole approximation. The scattering originates from a Bravais lattice, with the magnetic atoms occupying lattice points described by $\boldsymbol{R}_{ld} = \boldsymbol{l} + \boldsymbol{d}$.

$$
\hat{\mathbf{Q}}^D = \frac{1}{2} g_J f(\boldsymbol{\kappa}) e^{i\boldsymbol{\kappa}\cdot\boldsymbol{R}_{ld}} \hat{\boldsymbol{J}} \qquad (3.4.17)
$$

where g_J is the Landé g-factor given in section 2.3.1. The operator $\hat{\boldsymbol{J}}$ is the total angular momentum for the scattering state, which combined with the other constant factors, $\frac{1}{2}g_J$, gives the total magnetic moment in Bohr magnetons. $f(\boldsymbol{\kappa})$ is the magnetic form factor, which describes the $\boldsymbol{\kappa}$ dependence of the magnetic scattering. In the dipole approximation this is approximated to spherical symmetry. $f(\boldsymbol{\kappa})$ is given as

$$
f(\boldsymbol{\kappa}) = < j_0 > \frac{g_S}{g} + (< j_0 > + < j_2 >)\frac{g_L}{g} \qquad (3.4.18)
$$

It can be clearly seen in figure 3.2 that for $\boldsymbol{\kappa} = 0$ equation 3.4.17 is proportional to the total magnetic moment per ion. Setting $\boldsymbol{\kappa} = 0$ is often a good test of consistency for any code modelling magnetic scattering.

It should be noted that according to the International Tables for Crystallography, Volume C, Section 6.1.2.4 [35] the dipole approximation is only valid for transition metals compounds.

3.5 Summary and Outlook

This chapter aimed to introduce the relevant theory for the analysis of data from neutron scattering experiments. The equations developed above are used to model both powder and single crystal diffraction measurements taken at the ILL. The modelling and refinement of the magnetic structure for HoPtIn and DyPtIn powder data is reported and discussed in chapter 4. Chapters 5 and 6 use the equations for the multipole expansion of the form factor and those for magnetic scattering to determine the form factor of Ho^{3+} from a HoPtIn single crystal experiment. This concludes the main background and theory sections of this thesis.

Chapter 4

HoPtIn and DyPtIn Powder Diffraction Results

4.1 Introduction

The compounds HoPtIn and DyPtIn were chosen as typical members of the REPtIn series, which are suitable for neutron powder diffraction for three reasons:

1. The two magnetic transitions are well separated in temperature allowing these phases to be refined individually.

2. Dy and Ho have relatively low absorption cross-sections when compared with the rest of the magnetically ordering REPtIn compounds.

3. HoPtIn and DyPtIn are well suited to the argon-arc melting technique for sample preparation.

As such, powder samples of HoPtIn and DyPtIn were made at Loughborough University and measured at the ILL. For this analysis the high-flux neutron spectrometer D20 [27] was used. The results and conclusions from this experiment are reported in this chapter.

4.2   D20 Experimental Details

Both samples were prepared in the argon-arc furnace at Loughborough University using high purity materials. Care was taken to reduce impurities and possible contamination. The ingots were made molten three times to achieve homogenous samples, which were then powdered and passed through a 200 micron mesh to achieve a fine powder. The powder was used in a small sample canister on D20 with a diameter of 5mm. This canister size was selected so as to reduce absorption, but still give a strong signal. All data sets were processed for refinement by ILL software LAMP [37] (Large Array Manipulation Program), where dead detectors were removed and and normalisation corrections applied.

The HoPtIn sample was measured at $\lambda = 2.4$Å for an exact comparison to the data taken by Baran *et al.* Diffraction patterns were taken at two temperatures, T=100 K and T=2 K.

The DyPtIn sample was measured at $\lambda = 2.4$Å and at $\lambda = 1.87$Å. The $\lambda = 2.4$Å scans were for a short measurement time, as the temperature was ramped from T=2 K to T= 80K. This resulted in 120 diffraction patterns. The $\lambda = 1.87$Å measurements were taken between T=50 K and T=2 K at temperatures concentrating around the magnetic transitions. The temperature for these measurements was allowed to become stable at the set-point. A total of 20 diffraction patterns were taken at this wavelength.

4.3   DyPtIn Powder Results

4.3.1   Temperature Dependence of the Diffraction Patterns

The temperature dependence of the magnetic phase transitions can be seen in figure 4.1, for which the $\lambda = 2.4$Å data is used. As the temperature decreases the nuclear peaks at $2\theta = 21.4°$, $37.4°$, $43.3°$, $53.7°$ and $58.4°$ start to gain intensity below T∼30 K. This indicates that the first phase has a propagation vector of $\boldsymbol{k} = [0, 0, 0]$. Below T∼20 K new magnetic peaks are visible, for

which the propagation vector must be determined.
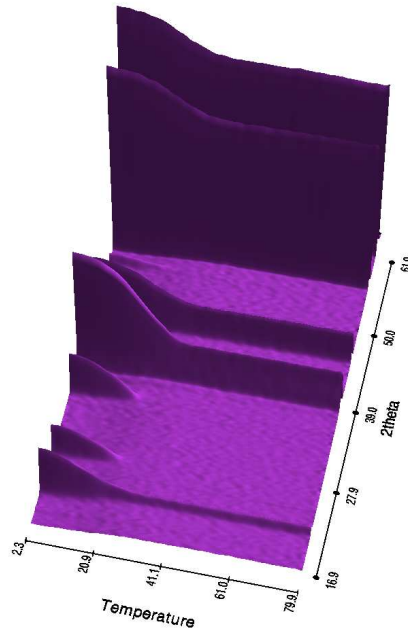
Figure 4.1: *3D plot of the temperature dependence of the low angle peaks for DyPtIn taken on D20. The two-step magnetic ordering can be seen as an initial gain in intensity on the nuclear peaks, followed by new purely magnetic peaks appearing as the temperature decreases.*

The nature of the magnetic order for the nuclear and two magnetic phases was determined using the Rietveld refinement software FullProf [38]. For this the $\lambda = 1.87$Å data was used, as the temperature was allowed to stabilise at the set point making the measurement more accurate. This data will be used to determine the exact ordering temperatures rather than that used to produce figure 4.1.

4.3.2 DyPtIn Nuclear Phase

The nuclear phase of DyPtIn was confirmed to be the space group $P\bar{6}2m$ with the Dy atom occupying the 3g site, the Indium occupying the 3f site and Platinum the 2c and 1b sites.
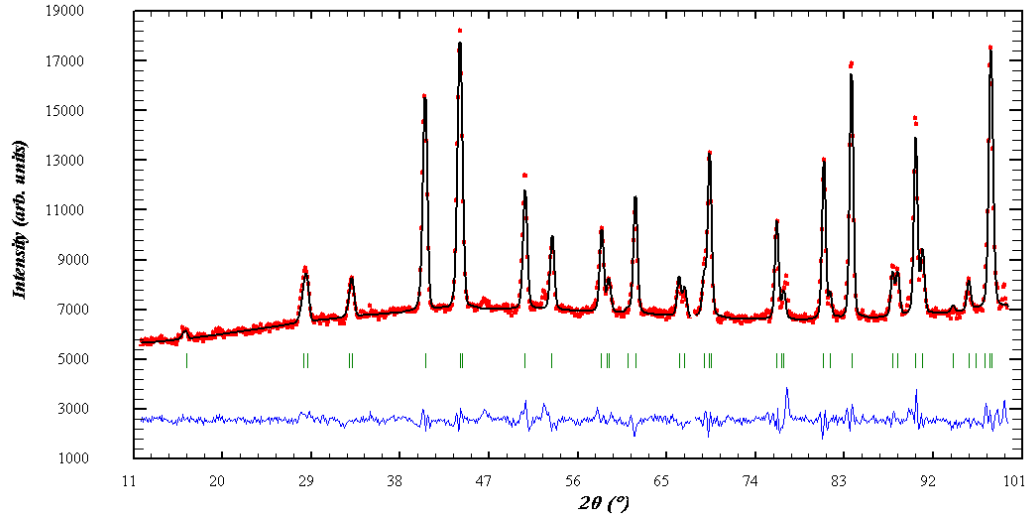
Figure 4.2: *The refinement of DyPtIn at T=50 K using FullProf.* $\chi^2 = 5.8$

Care had to be taken to implement the correct absorption correction in FullProf, for which the variable 'muR' is used. This was calculated using:

$$muR = R_{can}\ \rho_{unit}\frac{\lambda_{D20}}{\lambda_{Abs}} \sum_{atoms/unit} \sigma_i^{Abs} \qquad (4.3.1)$$

where R_{can} is the radius of the cylindrical sample canister and ρ_{unit} is the number density of one REPtIn unit. This is calculated from the mass density used and must be measured to properly account for 'voids' in the powder. muR was calculated to be $muR = 4.9$ for the Dy sample, which is highly absorbing. Because of this the absorption correction by N.N Lobanov and L. Alte da Veiga was implemented by putting $muR = -4.9$ in the .pcr file[1].

4.3.3 DyPtIn Ferromagnetic Phase

Below T=33 K the nuclear peaks start to gain intensity indicating the onset of magnetic order. The nature of the magnetic order was investigated using the irreducible representations (IR) of the propagation vector $\boldsymbol{k} = [0, 0, 0]$. There are five IR consistent with the space group. Of these five only two restrict

---

[1]'.pcr' is the extension for the input file for FullProf refinements

the moments to the c-axis, one of which is complex. To determine the correct model, all five IR were implemented and refined to give the best possible fit. Of these, only Γ_3 was a good fit to the data, which restricts the moments to the c-axis. Γ_3 is a real representation. This is consistent with the single crystal magnetisation study performed by Morosan *et al.* [2], which shows an easy-axis alignment. This model gave an excellent fit for the data sets taken at T= 33, 30, 28, 28, 27, 24, and 22 K. Figure 4.3 below shows a typical refinement for this phase, for T=24K, where the refined moment is $\mu_{24K}^{Ferro} = 4.8 \pm 0.3 \mu_B/Dy$. Below T=21 K new magnetic peaks appear, which can not be modelled with this simple ferromagnetic phase.
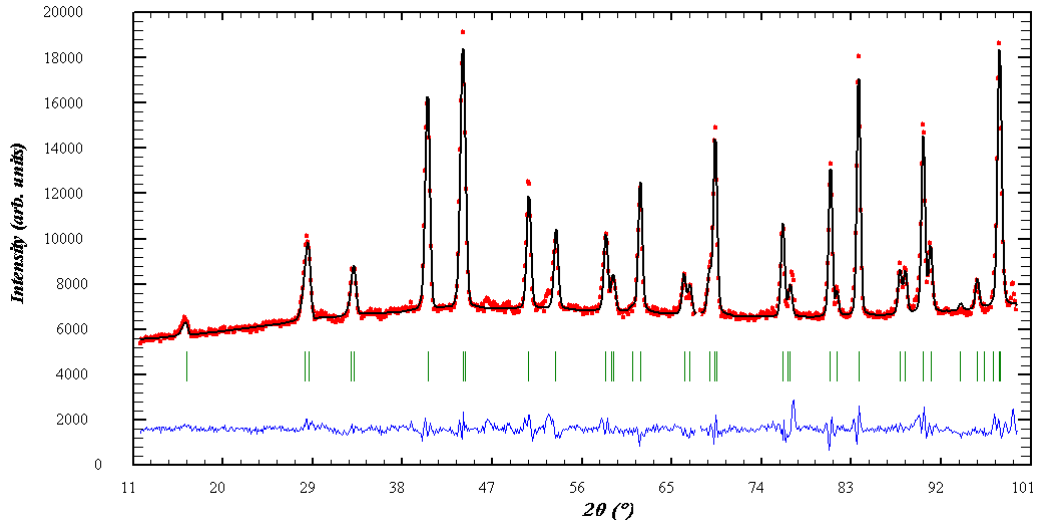
Figure 4.3: *The refinement of DyPtIn at T=24 K using FullProf.* $\chi^2 = 6.3$.

4.3.4 The Second Magnetic Phase of DyPtIn

At low temperatures and for low 2θ values new magnetic peaks appear. These are most noticeable at $2\theta = 19.6°$ and $25.8°$. These peaks were indexed and used with the software 'k_search' available as part of the FullProf suite. The output from this programme gave three 'likely' candidates for the propagation vector. These were $\boldsymbol{k}_1 = [\frac{1}{2}, 0, \frac{1}{2}]$, $\boldsymbol{k}_2 = [\frac{1}{2}, \frac{1}{2}, \frac{1}{2}]$ and $\boldsymbol{k}_3 = [\frac{1}{8}, 0, \frac{1}{2}]$. In addition to this several other possibilities were checked for viability. These were:

$$\boldsymbol{k}_4 = [\tfrac{1}{2}, 0, 0] \quad \boldsymbol{k}_9 = [0, 0, \tfrac{1}{3}] \quad \boldsymbol{k}_{14} = [\tfrac{1}{3}, 0, \tfrac{1}{2}]$$
$$\boldsymbol{k}_5 = [0, 0, \tfrac{1}{2}] \quad \boldsymbol{k}_{10} = [\tfrac{1}{3}, \tfrac{1}{3}, 0] \quad \boldsymbol{k}_{15} = [0, \tfrac{1}{3}, \tfrac{1}{2}]$$
$$\boldsymbol{k}_6 = [\tfrac{1}{2}, 0, \tfrac{1}{2}] \quad \boldsymbol{k}_{11} = [\tfrac{1}{3}, 0, \tfrac{1}{3}] \quad \boldsymbol{k}_{16} = [\tfrac{1}{2}, 0, \tfrac{1}{3}]$$
$$\boldsymbol{k}_7 = [\tfrac{1}{2}, \tfrac{1}{2}, 0] \quad \boldsymbol{k}_{12} = [\tfrac{1}{3}, \tfrac{1}{3}, \tfrac{1}{3}] \quad \boldsymbol{k}_{17} = [0, 0, 0]$$
$$\boldsymbol{k}_8 = [\tfrac{1}{3}, 0, 0] \quad \boldsymbol{k}_{13} = [\tfrac{1}{3}, \tfrac{1}{2}, 0] \quad \boldsymbol{k}_{18} = [\tfrac{1}{2}, \tfrac{1}{2}, \tfrac{1}{3}]$$
$$\boldsymbol{k}_{19} = [\tfrac{1}{3}, \tfrac{1}{2}, \tfrac{1}{2}]$$

From these $\boldsymbol{k}_1 = [\tfrac{1}{2}, 0, \tfrac{1}{2}]$ was identified as the most appropriate propagation vector. This result is in agreement with the analysis reported by Baran *et al.* [1]. This propagation vector was then used in *BasIreps* [39], which calculates the IR of the propagation vector and provides an output suitable for use in the .pcr file. The $\boldsymbol{k} = [\tfrac{1}{2}, 0, \tfrac{1}{2}]$ propagation vector separates the magnetic sites into two orbits. Orbit 1 links two atoms by symmetry, whilst orbit 2 leaves the third independent. Orbit 1 contains the atoms on the sites $(x_{RE}, 0, \tfrac{1}{2})$, and $(\overline{x}_{RE}, \overline{x}_{RE}, \tfrac{1}{2})$, while orbit 2 only contains the site $(0, x_{RE}, \tfrac{1}{2})$. There are four IR for orbit 1, and three IR for the orbit 2, all of them real. These are tabulated below in table 4.1.

Orbit 1	Site 1			Site 2		
	a	**b**	**c**	**a**	**b**	**c**
Γ_1	1	-	-	-1	-1	-
	-	1	-	-	1	-
Γ_2	-	-	1	-	-	-1
Γ_3	1	-	-	-	1	1
	1	-	-	-	-1	-
Γ_4	-	-	1	-	-	1

Orbit 2	Site 3		
	a	**b**	**c**
Γ_1	2	1	-
Γ_2	-	-	1
Γ_3	-	-1	-

Table 4.1: *The IR of propagation vector $\boldsymbol{k} = [\tfrac{1}{2}, 0, \tfrac{1}{2}]$ for the space group $P\bar{6}2m$ where the magnetic atom occupies the 3g site. This has m2m point symmetry.*

It was possible to construct twelve different magnetic structures from the different IR. This included arrangements where the moments are restricted to the **c**-axis or to within the ab-plane. The magnetic structure found by Baran *et al.* discussed in section 2.5 uses a canted moment structure. Their diagram shows the components of the magnetic moment structure in the ab-plane. The figure has been reproduced as figure 2.10 in section 2.5.1. Their moment structure corresponds to a representation of the form:

	a	b	c
Site 1	-1	-	-
Site 2	0	-1	-
Site 3	1	1	-

This representation does not appear in table 4.1, and it is inconsistent with the symmetry of the space group. As such it was necessary to identify the correct orientation of the magnetic moments. All permutations of the IR were implemented and refined to try to ascertain the combination that is realised physically. Of all the possibilities, the model implementing Γ_3 for orbit 1, and Γ_1 for orbit 2 gave the best fit. This combination of IR constructs an antiferromagnetic, in-plane phase. Using the '$\Gamma_3\Gamma_1$' model the remaining low temperature diffraction patterns were refined, all with a $\chi^2 < 7$. The T=2 K diffraction pattern and the '$\Gamma_3\Gamma_1$' model is shown below in figure 4.4.
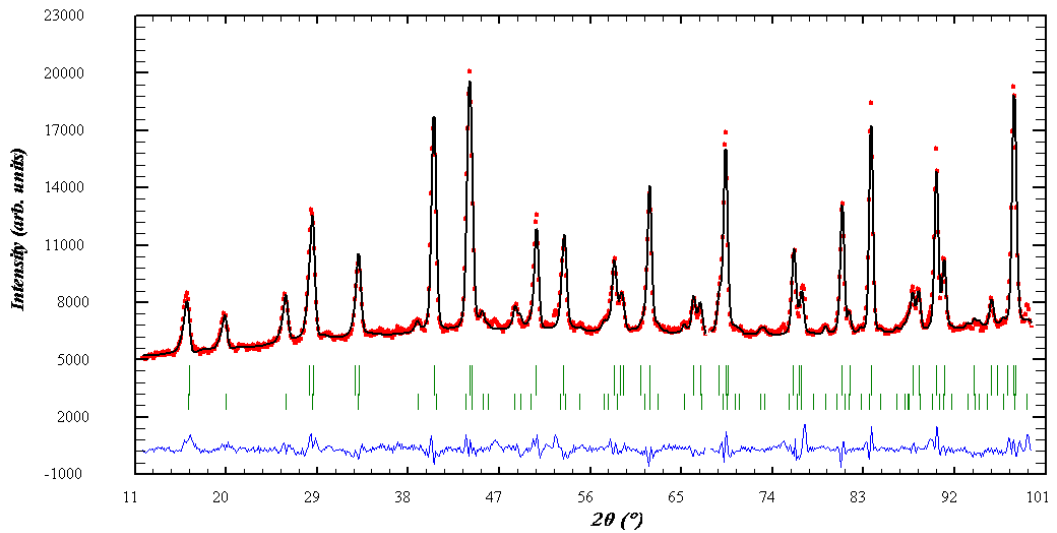
Figure 4.4: *The refinement of DyPtIn at T=2 K using FullProf. The $\chi^2 = 6.7$. The model uses three phases: nuclear, ferromagnetic and the IR $\Gamma_3\Gamma_1$ for the propagation vector $\boldsymbol{k} = [\frac{1}{2}, 0, \frac{1}{2}]$.*

4.3.5 Magnetic Structure

The magnetic structure of DyPtIn is a superposition of two phases. The first phase is a ferromagnetic structure with the moments aligned along the **c**-axis. The second phase in an in-plane arrangement, with the orientations of the moments given by Γ_3 and Γ_1 of the IR for orbit 1 and 2 respectively. Figure 4.5 below shows the magnetic structure for the ferromagnetic phase, which at T=2 K has a magnetic moment of $\mu_c = 7.3 \pm 0.3 \mu_B/Dy$.

The second phase, in the ab-plane, allows the moments on orbit 1 to be different to that on orbit 2. For T= 2K the magnetic moment for orbit 1 (O1) is $\mu_{ab}^{O1} = 2.64 \mu_B/Dy$ and that for orbit 2 (O2) is $\mu_{ab}^{O2} = 2.34 \mu_B/Dy$. This means that the total moment given by $\sqrt{(\mu_{ab})^2 + (\mu_c)^2}$ is $\mu_{Total}^{O1} = 7.68 \mu_B/Dy$ and $\mu_{Total}^{O2} = 7.78 \mu_B/Dy$. The magnetic structure in the ab-plane is shown in figure 4.6, where four unit cells are shown. The temperature dependence of the magnitude of the moment and other physical quantities extracted from these fits are presented in the next section.
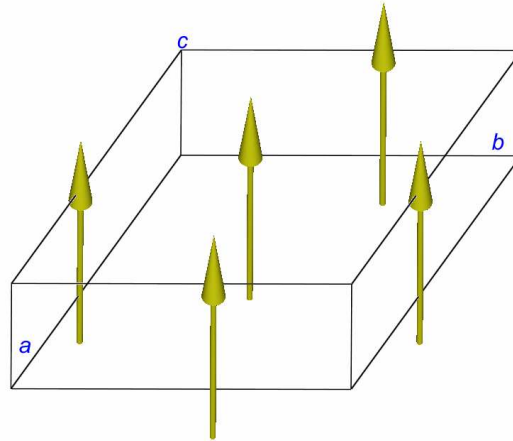
Figure 4.5: *The magnetic structure of DyPtIn at T=2 K along the c-axis. The magnetic atoms are in the $z = \frac{1}{2}$ plane.*
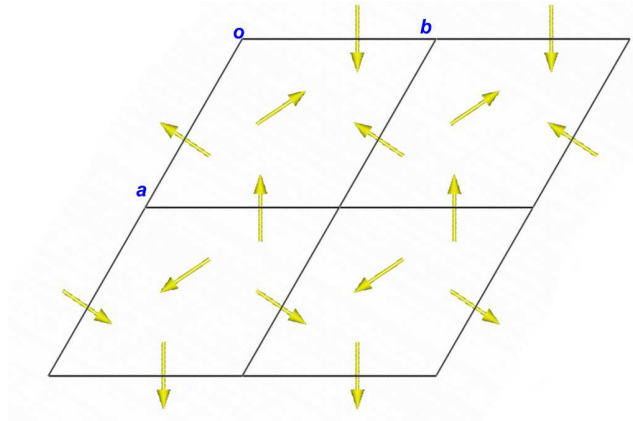
Figure 4.6: *The magnetic structure of DyPtIn at T=2 K using the IR model* 'Γ_3, Γ_1' *for the propagation vector* $\boldsymbol{k}_1 = [\frac{1}{2}, 0, \frac{1}{2}]$ *as described in the text. This propagation vector is a doubling along the* $\boldsymbol{c}$ *and* $\boldsymbol{a}$ *axis. The diagram shows four unit cells in the ab-plane.*

4.3.6 Temperature Dependent Results

The refinement of the 20 $\lambda = 1.87$Å diffraction patterns allows the exact determination of key physical parameters. The temperature dependence of the unit cell dimensions, volume and atomic positions is shown in the next series of plots. In these plots the fractional change is shown normalised to unity as T$\to$ 0 K. The temperature dependence of the magnetic phases is also plotted and discussed.

4.3.6.1 Temperature Dependence of the Lattice Parameters

The temperature dependence of the primitive cell constants **a** and **c**, and the unit cell volume are plotted in figure 4.7. Both **a** and **c** have points of inflection around T$\sim$21 K and T$\sim$32 K, which coincides with the onset of the magnetic order. As temperature increases **a** gets bigger, whilst **c** gets smaller. The fractional change in volume does not seem to vary at the same temperatures as **a** and **c**, and is arguably constant within the error bars.
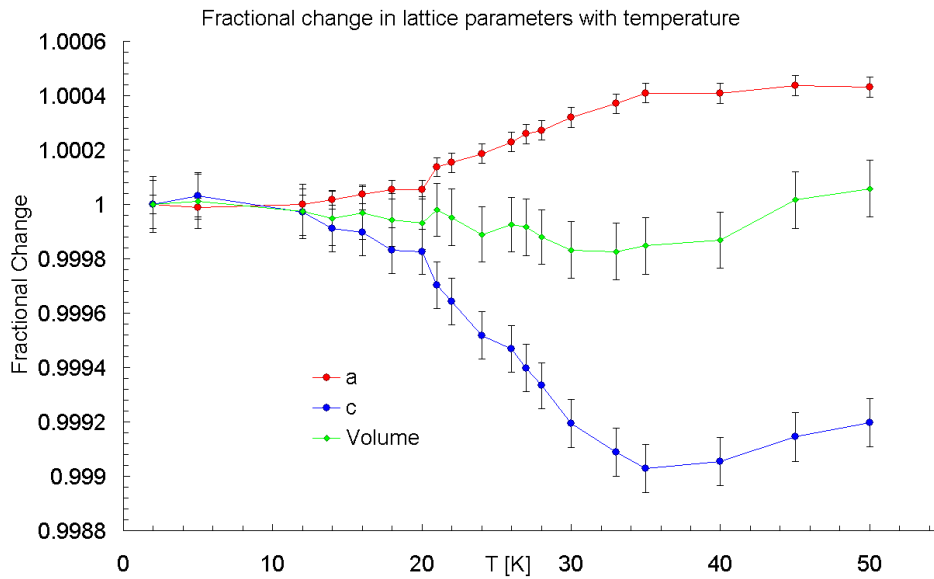
Figure 4.7: *The temperature dependence of the unit cell parameters. Note that the fractional change is plotted, normalised to unity as T→ 0. Red = **a**, Blue = **c** and Green = primitive unit cell volume*
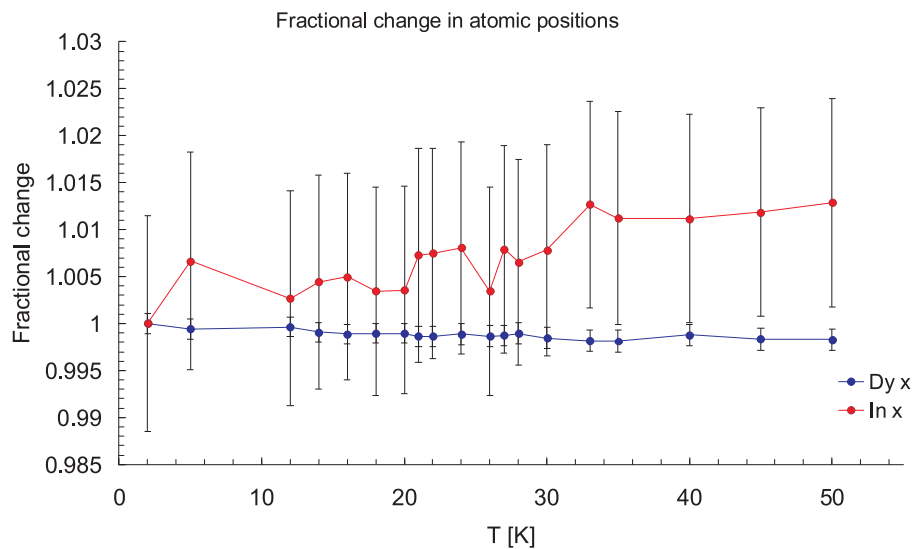
Figure 4.8: *The temperature dependence of the atomic positions of Dysprosium (Blue) and Indium (Red). Note that the fractional change is plotted, normalised to unity as T→ 0.*

The refinable atomic positions described in section 2.2 are shown in figure 4.8. The x_{Dy} position slightly decreases with increasing temperature, although it is constant within the error bars of the individual measurement. There do not appear to be any points of inflection around the temperatures of the magnetic transitions. The position of the indium site generally increases with temperature. The larger error bars make it hard to conclusively comment on any general trend, other than that the data seems to be smoother above the Curie temperature.

4.3.6.2 Temperature Dependence of the Magnetic Phases

The temperature dependence of the magnetic phase is split into two parts, the initial c-axis ferromagnetic phase followed by the second antiferromagnetic in-plane phase. The temperature dependence of the magnetic moment confined to the c-axis is plotted below in figure 4.9. This plot shows that as temperature decreases the ordered moment starts to increase below T$\sim$ 35 K until T$\sim$ 20.5 K. Exact values for the magnetic ordering temperature are determined in the next section 4.3.6.3. Below T$\sim$ 20.5 K the moment increases at a lesser rate compared to the initial phase. If this was one continuous transition the moment would be proportional to the square of the intensity. However, as there are two magnetic ordering parameters involved, a fit of this type was not used. Instead a linear fit restricted to the low temperature data points was used as an approximation. Using this, the maximal ferromagnetic moment is extrapolated to be $\mu_c = 7.47 \pm 0.08 \mu_B / Dy$ at T=0 K.
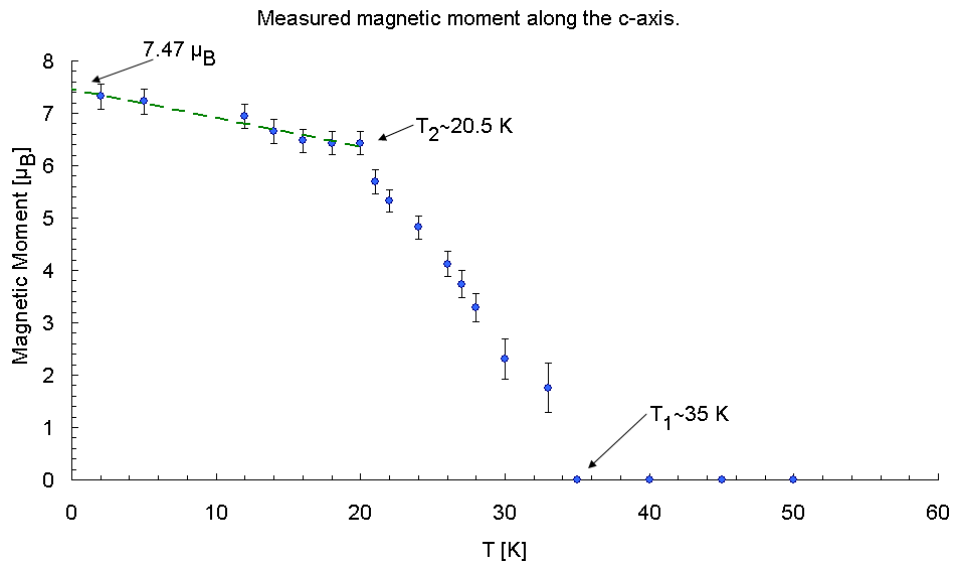
Figure 4.9: *The temperature dependence of the ferromagnetic moment, aligned along the c-axis. The green line is a linear approximation used to calculated the ordered moment.*
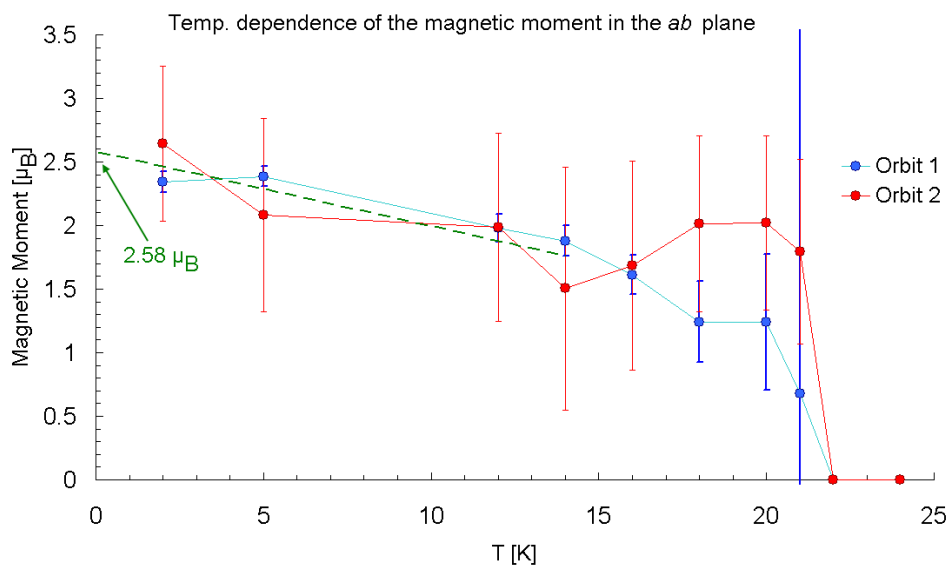
Figure 4.10: *The temperature dependence of the antiferromagnetic moment, in the ab-plane.*

The second magnetic phase allows the magnetic moments in orbit 1 to be of a different size to that in orbit 2. Figure 4.10 shows the temperature dependence of the magnitude of the moments, where the blue data points are for Orbit 1, the red for Orbit 2. The moments have not refined to the exactly the value, and there does not seem to be any trend, such as one moment being consistently greater than the other. However, as these moments agree within their error bars it is likely that they are similar in size, or possibly identical. The larger error bars indicate that the refinement is sensitive to similar local-minima in this parameter space. This means that slightly different values give equally good fits. The average of the two moments, extrapolated to T=0, is $\mu_{ab}^{av} = 2.6 \pm 0.1 \mu_B/Dy$.

The final figure is for the total moment, which has been calculated using $\mu_{total} = \sqrt{(\mu_{ab})^2 + (\mu_c)^2}$. This again shows the ferromagnetic phase, and then the total moment for the two orbits, which is shown using different colours. The total average moment is calculated to be $\mu_{total}^{av} = \sqrt{7.47^2 + 2.6^2} = 7.90 \pm 0.09 \mu_B/Dy$ at T=0 K, which is much less than the theoretical ordered moment for Dy^{3+}, $\mu_{theory} = 10 \mu_B/Dy$.
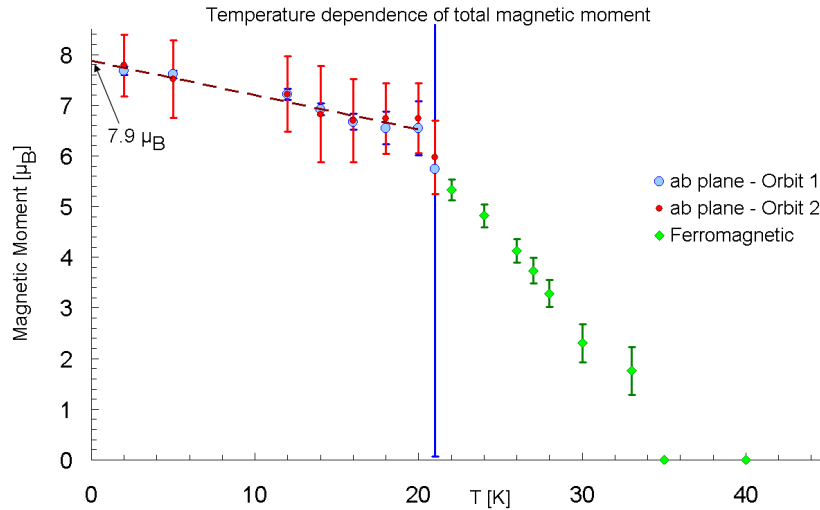
Figure 4.11: *The temperature dependence of the total magnetic moment. The red line is used to find the total moment at T=0 K. It was fitted to the averaged data set for orbit 1 and orbit 2 (not explicitly shown.)*

4.3.6.3   Determination of Magnetic Ordering Temperatures

The determination of the magnetic ordering temperatures was performed using the integrated intensity of seven low angle peaks. For this analysis linear regression was performed within three regions, corresponding to the nuclear phase and the two magnetic phases. This was roughly within the temperature ranges: $0\ K < T < 20\ K$, $20\ K < T < 30\ K$ and $30\ K < T$. The first magnetic transition, around T$\sim$30 K is denoted T_c, for the Curie temperature. The second magnetic transition is denoted T_{ab}, as below this temperature the in-plane component is present. The next graphs, labelled figures 4.12 and 4.13, show the temperature dependence of the integrated intensity of the seven low angle peaks. The identity of these peaks is summarised in table 4.2 along with the values of T_{ab} and T_c as extrapolated from the plots. The final column in this table shows the average of the values obtained. This average is used as the final value for the ordering temperatures. These are found to be $T_{ab} = 18 \pm 2$ K and $T_c = 28.1 \pm 0.3$ K.

(h,k,l)=	(1,0,0)	(0,-1,0)*	(1,-1,-1)*	(0,0,1)	(1,0,1)	(1,1,1)	(2,0,1)		
2θ	16.46	20.15	26.18	28.77	33.38	40.88	44.41	Mean	$\pm$
T_{ab}	-	-	-	18.26	17.54	17.31	17.35	17.62	0.22
T_c	29.54	22.96	22.84	29.90	30.98	30.06	30.67	28.14	1.36

Table 4.2: *The 2θ position of the seven peaks investigated, along with the Miller index. Note, those indicies identified with (*) are generated with the propagation vector $\boldsymbol{k} = [\frac{1}{2}, 0, \frac{1}{2}]$. T_{ab} and T_c are the ordering temperatures, measured in [K], defined in the main text. The last column shows the average value for the ordering temperatures.*
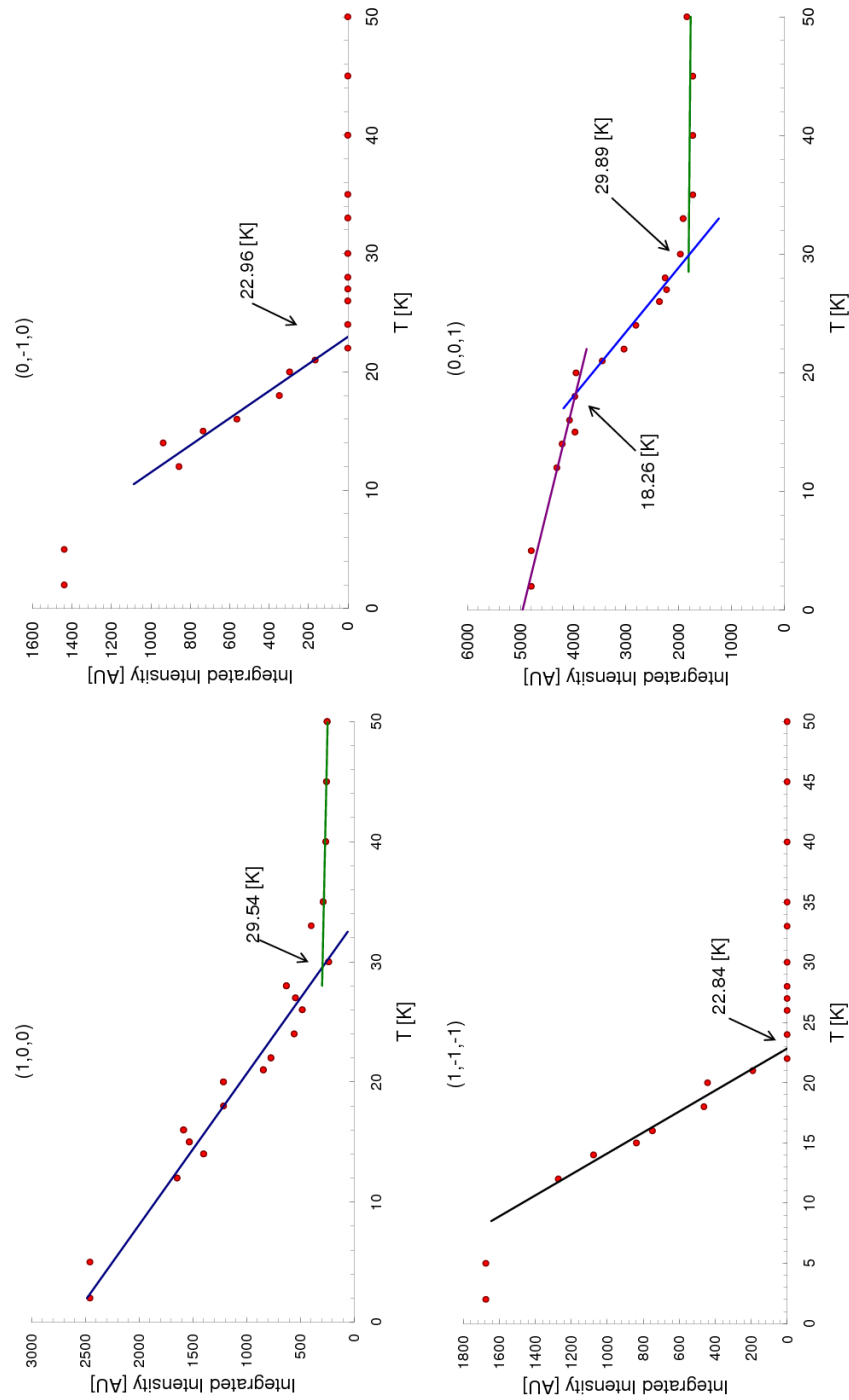
Figure 4.12: *Plots of the temperature dependence of the integrated intensity for the (1,0,0), (0,-1,0), (1,-1,-1) and (0,0,1) peaks. The linear fits and line intercepts are shown. These were used to calculate the transition temperatures. Note, AU= arbitrary units.*
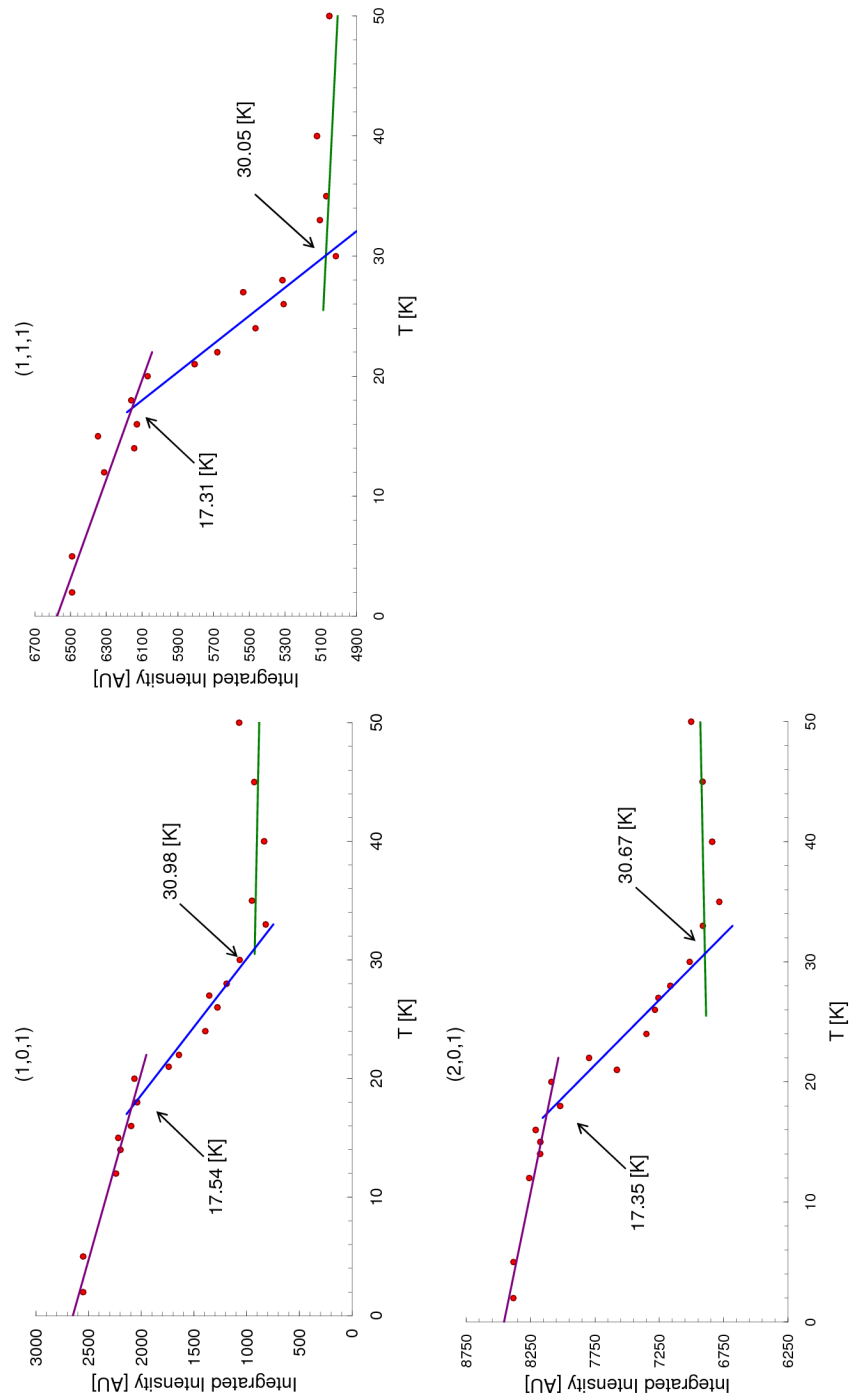
Figure 4.13: *Plots of the temperature dependence of the integrated intensity for the (1,0,1), (1,1,1) and (2,0,1) peaks. The linear fits and line intercepts are shown. These were used to calculate the transition temperatures.Note, AU= arbitrary units.*

4.3.7 Summary of DyPtIn Results

The full data set from these refinements are presented in table 4.3 and 4.4 below. In these tables the absolute values are used. The pcr file for the T=2 K data used for the FullProf refinement is included in appendix A for reference. The previous sections discussed the magnetic structure of DyPtIn, and ascertained the temperature dependence of the crystallographic parameters. These results are further commented on in the conclusions of this chapter, following the analysis of HoPtIn.

T [K]	a [Å]	±Δ	c [Å]	±Δ	Volume [Å]³	±Δ	x_{Dy} [Å]	±Δ	x_{In} [Å]	±Δ
2	7.569798	0.00019	3.83808	0.00024	190.464	0.014	0.5941	0.00044	0.25993	0.00211
5	7.56971	0.00018	3.8382	0.00023	190.466	0.013	0.59376	0.00044	0.26166	0.00214
12	7.5698	0.00017	3.83797	0.00022	190.459	0.013	0.59388	0.00042	0.26063	0.00208
14	7.56993	0.00018	3.83774	0.00022	190.454	0.013	0.59356	0.00043	0.26108	0.00208
16	7.57008	0.00017	3.83768	0.00021	190.458	0.012	0.59345	0.00042	0.26123	0.00193
18	7.57021	0.00017	3.83743	0.00022	190.453	0.012	0.59348	0.00043	0.26083	0.00196
20	7.57021	0.00017	3.83741	0.00021	190.451	0.012	0.59347	0.00043	0.26086	0.00195
21	7.57084	0.00018	3.83694	0.00022	190.46	0.012	0.59329	0.00044	0.26182	0.00205
22	7.57096	0.00019	3.83671	0.00023	190.455	0.014	0.59329	0.00047	0.26188	0.00199
24	7.57121	0.00019	3.83623	0.00023	190.443	0.013	0.59343	0.00048	0.26203	0.00202
26	7.57153	0.00019	3.83604	0.00023	190.45	0.013	0.5933	0.00048	0.26083	0.00195
27	7.57176	0.00019	3.83577	0.00023	190.448	0.014	0.59334	0.00049	0.26199	0.00192
28	7.57186	0.00019	3.83552	0.00022	190.441	0.013	0.59348	0.00048	0.26163	0.00189
30	7.57222	0.0002	3.83499	0.00024	190.432	0.014	0.59318	0.00052	0.26196	0.00202
33	7.5726	0.0002	3.83458	0.00024	190.431	0.014	0.59302	0.00052	0.26323	0.0019
35	7.5729	0.0002	3.83435	0.00024	190.435	0.014	0.59299	0.00054	0.26285	0.00204
40	7.57289	0.0002	3.83445	0.00024	190.439	0.014	0.59337	0.00053	0.26283	0.00194
45	7.5731	0.00021	3.8348	0.00025	190.467	0.014	0.59313	0.00054	0.26301	0.00194
50	7.57306	0.0002	3.835	0.00024	190.475	0.014	0.59309	0.00053	0.26328	0.00194

Table 4.3: *The refined values for the crystallographic parameters of HoPtIn. In_x and Dy_x are the refinable atomic positions.*

T [K]	mu_c [μ_B]	±Δ	μ^{O1} [μ_B]	±Δ	μ^{O2} [μ_B]	±Δ	μ^{Av}_{Total} [μ_B]	±Δ
2	7.32	0.25	2.34	0.08	2.64	0.61	7.73	0.37
5	7.22	0.25	2.39	0.08	2.08	0.76	7.56	0.47
12	6.94	0.23	1.98	0.11	1.99	0.74	7.22	0.43
14	6.66	0.23	1.88	0.12	1.51	0.96	6.87	0.58
16	6.48	0.22	1.61	0.16	1.69	0.82	6.68	0.46
18	6.43	0.23	1.24	0.32	2.02	0.69	6.63	0.41
20	6.43	0.22	1.24	0.53	2.02	0.69	6.63	0.50
21	5.70	0.23	0.68	5.67	1.79	0.73	5.83	5.16
22	5.33	0.21	0	0	0	0	5.33	0.21
24	4.82	0.22	0	0	0	0	4.82	0.22
26	4.12	0.24	0	0	0	0	4.12	0.24
27	3.74	0.26	0	0	0	0	3.74	0.26
28	3.28	0.27	0	0	0	0	3.28	0.27
30	2.31	0.38	0	0	0	0	2.31	0.38
33	1.76	0.47	0	0	0	0	1.76	0.47
35	0	0	0	0	0	0	0	0
40	0	0	0	0	0	0	0	0
45	0	0	0	0	0	0	0	0
50	0	0	0	0	0	0	0	0

Table 4.4: *The refined values for the magnetic phases of DyPtIn. μ_c is the ferromagnetic magnetic moment, restricted to the c-axis. μ^{O2} and μ^{O1} are the magnetic moments for orbit 1 and orbit 2 of the $\boldsymbol{k} = [\frac{1}{2}, 0, \frac{1}{2}]$ magnetic phase, which is restricted to the ab-plane. μ^{Av}_{Total} is the averaged total magnetic moment per Dy site.*

4.4 HoPtIn Powder Results

4.4.1 HoPtIn Nuclear Phase

The HoPtIn sample was measured at T=80 K at $\lambda = 2.4$Å. The high temperature measurement was refined with the $P\bar{6}2m$ space group and in the same manner as the DyPtIn sample discussed previously. The refinement of this phase left several low intensity peaks un-indexed. These are attributed to impurities within the sample. The un-indexed peaks were fitted using a pure Platinum phase and a $HoInPt_4$ phase. The pure Pt phase crystallises in the $Pm-3m$ space group with Pt atoms on the 1a, 3c, and 1d sites. The $HoInPt_4$ phase forms in the $P6_3/mmc$ space group, with the Pt on the 4f site, Ho on the 2c site and In on the 2a site. That these impurity phases could be present is not unexpected, due to the nature of the sample fabrication. For example, the molten ingot may not have formed a completely homogenous melt leaving a Platinum-rich region, where these impurities formed. As this sample contained impurity phases, it was decided to only take one further measurement at T= 2K. The refinement of the nuclear phase is shown below in figure 4.14.
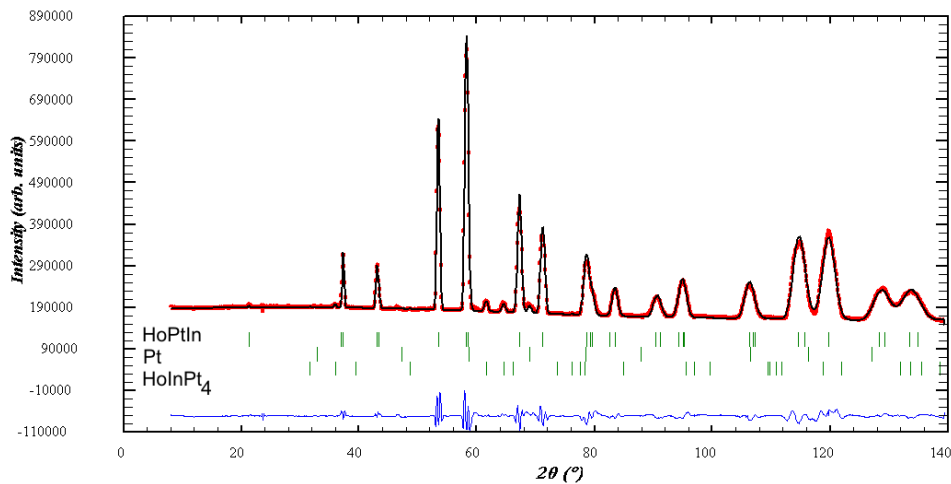
Figure 4.14: *The refinement of HoPtIn nuclear phase at T=80 K. This refinement required two additional phases, that of Pt and HoInPt$_4$. The impurity phases are indicated to the left of the green index-marks. $\chi^2 = 1462$.*

4.4.2 HoPtIn Magnetic Phase

The magnetic phase of HoPtIn was identified to be the same as the one seen in DyPtIn. The model used implements a ferromagnetic moment aligned to the c-axis, and an antiferromagnetic ab-plane structure. The ferromagnetic component, which is described using the propagation vector $\boldsymbol{k}_1 = [0, 0, 0]$, refined to $\mu_c = 3.80 \pm 0.05 \mu_B/Ho$. The moments described by Γ_3 and Γ_1 for orbit 1, and orbit 2 were $\mu_{ab}^{O1} = 1.03 \pm 0.05 \mu_B/Ho$ and $\mu_{ab}^{O2} = 1.8 \pm 0.2 \mu_B/Ho$ respectively. This gives a total average moment of $\mu_{Total}^{Av} = 4.04 \pm 0.08 \mu_B/Ho$, which is much less than predicted, $\mu_{Theory}^{Max} = 10 \mu_B/Ho$. A reduced moment has also been reported in this compound by Baran *et al.* [1] of $\mu_{Total}^{Baran} = 8.2 \mu_B/Ho$. The reduction reported here is over $4\mu_B/Ho$ less than reported by Baran *et al.* and may indicated that the model is not correctly implemented. However, a better fit with this data set could not be found, which indicates that the impurities in this sample are affecting this refinement. The refinement of the antiferromagnetic phase, within the ab-plane, attributes a smaller moment to the magnetic sites on Orbit 1 than that on Orbit 2. The magnetic structure in the ab-plane is shown in figure 4.16 below, in which the smaller moment is visible.

4.5 Conclusions and Discussion of Powder Data

The research presented in this chapter has identified the magnetic order in two compounds, HoPtIn and DyPtIn. This was achieved by analysing neutron diffraction data from powdered samples.

The DyPtIn analysis showed the development of the magnetic order, and the onset of two distinct magnetic phases. The temperature dependance of the lattice parameters has been analysed and plotted, as have the atomic positions. Symmetry analysis allowed the exact orientation of the magnetic moments to be identified, using the irreducible representations of the propagation vectors $\boldsymbol{k}_1 = [0, 0, 0]$, and $\boldsymbol{k}_2 = [\frac{1}{2}, 0, \frac{1}{2}]$. This showed that the ground state has a magnetic structure with a large component along the c-axis, and an additional smaller component in the ab-plane. These components were found to be $\mu_c =$
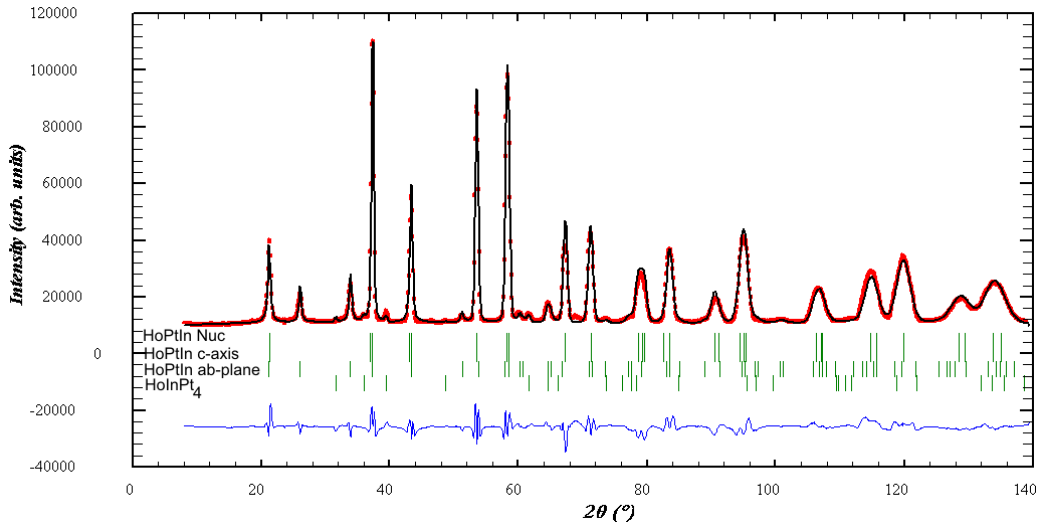
Figure 4.15: *The refinement of HoPtIn magnetic phase at T=2 K. This refinement required four phases. The first is the nuclear phase of HoPtIn. The second and third are the magnetic phases of HoPtIn, split according to their propagation vector. The third is the impurity phase HoInPt$_4$ identified previously. The phases are indicated to the left of the green index-marks.* $\chi^2 = 7143$

$7.47\pm0.08\mu_B/Dy$ and $\mu_{ab}^{av} = 2.6\pm0.1\mu_B/Dy$, respectively, at T=0 K. The total average moment is calculated to be $\mu_{total}^{av} = 7.90\pm0.09\mu_B/Dy$ at T=0 K. This is much less than the theoretical ordered moment for Dy^{3+}, $\mu^{theory} = 10\mu_B/Dy$.

This reduced moment is also reported by other authors, as discussed in the literature review in section 2.5.1. Baran *et al.* [1] determine a similar structure from their neutron diffraction experiments, although the magnetic structure they determine is not consistent with the IR of the propagation vector. However, they report magnetic moments of $\mu_c^{Baran} = 6.6\mu_B/Dy$ and $\mu_{a-b}^{Baran} = 4.9\mu_B/Dy$ giving a total of $\mu_{total}^{Baran} = 8.2\mu_B/Dy$.

The temperatures of the magnetic transitions for DyPtIn have been determined by analysing the integrated intensity of seven magnetic peaks. These are found to be T$_c = 28.1 \pm 0.3$ K and T$_{ab} = 18 \pm 2$ K. Morosan *et al.* determined T$_c^{Morosan} = 26.5$ K using specific heat data. This is similar to the value that is found when using neutrons.

Both Morosan and Baran comment that there are points of inflection in
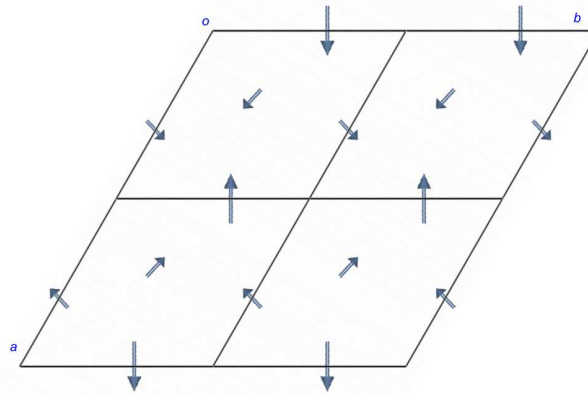
Figure 4.16: *The magnetic structure of HoPtIn in the ab-plane. The moments visibly smaller are those linked by Orbit 1 of the IR used. This diagram shows 4 unit cells.*

the temperature dependent magnetisation data at around T=17.9 K and T= 7.3 K. Baran speculates that the antiferromagnetic component onsets below T_{ab}^{Baran}=17.9 K. This is in excellent agreement with that found in this study. The point of inflection at T=7.3 K is not evident in this neutron data.

The HoPtIn analysis at T=2K found the c-axis component of the magnetic moment to be $\mu_c = 3.80 \pm 0.05 \mu_B/Ho$ and that in the ab-plane to be $\mu_{ab}^{av} = 1.40 \pm 0.06 \mu_B/Ho$. This gives a total average moment of $\mu_{Total}^{Av} = 4.04 \pm 0.08 \mu_B/Ho$ which is much less than the maximum theoretical moment, $\mu_{Theory}^{Max} = 10 \mu_B/Ho$. This is a greater reduction in observed moment than previously reported, and indicates a problem with impurities in the HoPtIn sample. Baran reports a total moment of $\mu_{total}^{Baran} = 8.2 \mu_B/Ho$ at T=2K using neutron diffraction.

The total ordered magnetic moments of DyPtIn and HoPtIn have been found to be reduced when compared to the theoretical maximum given by Hunds rules. This is a property observed in many members of the REPtIn series, for which there has been no adequate physical explanation. Clearly further work is needed to determine the magnetic interactions that cause this reduced moment. This will require the determination of magnetisation density within the unit cell, and the calculation of the the crystal field splitting. For

the latter type of analysis, spin-polarised neutrons are used, which requires a high quality single crystal of adequate size. This experiment is discussed in the next chapter.

Chapter 5

HoPtIn Single Crystal Results

Two main theories to explain the effects observed in the REPtIn series are described in section 2.5.3. The first, an induced moment on the platinum $1b$ site, requires a spin-density measurement of the unit cell to establish it. The second, a canted moment due to an antiferromagnetic in-plane component would be seen in single crystal diffraction. This data would also confirm the nature of the magnetic structure, as there is disagreement between that proposed by Baran *et al.* and that determined in the previous chapter. To this end a set of single crystal experiments were performed at the Institut Laue-Langevin (ILL).

Ideally a single crystal of DyPtIn would be best, as it would compliment the in-depth analysis performed on the powder sample, reported in the previous chapter. However, the quality of the single crystal samples meant that HoPtIn had to be chosen instead. This system is similar to DyPtIn, and seems to magnetically order in the same way. Also, Dy^{3+} and Ho^{3+} have the same theoretical ordered moment, $10\mu B$, making this a suitable substitution. The experimental details of these investigations are detailed in this chapter, along with results and conclusions.

5.1 HoPtIn Crystal Growth

When HoPtIn is cooled from the melt, small crystallites are visible on the surface of the ingot. This suggests that a single crystal could be 'pulled' from the melt. This was implemented using the tri-arc furnace. In this method a rotating metal rod was pulled from molten material in the correct stoichiometry. The rod was pulled at a rate of $mm/hour$ allowing a small, narrow crystal to grow. This method is highly time intensive and was met with limited success.

A second option for crystal growth, reported in the literature [6], is the 'flux technique'. In this method molten Ho, Pt and indium are allowed to cool slowly in an excess of indium. As the solution cools, HoPtIn crystallites form in the indium suspension. The excess indium is then etched away. This technique demands specialist equipment and expertise, for which a collaboration was initiated between Loughborough University and Emilia Morosan at Rice University, USA. Morosan was able to supply several high quality single crystals, which were used for the D3 [40] and D9 [41] experiments.

5.2 HoPtIn Orient Express

The quality of the tri-arc and the indium flux crystals was checked using Orient Express [42] at the ILL. The tri-arc crystals were of much poorer quality than those grown in indium flux. Therefore the tri-arc samples were not used in these experiments. A flux grown crystal of dimensions $0.6mm \times 8mm$ was selected. A neutron Laue photograph of this crystal is shown in figure 5.1 below.

5.3 The Hot Neutron Diffractometer D9

D9 [41] uses non-polarised neutrons for the characterisation of single crystal samples. The incident beam is monochromatic and highly focused with a wavelength $\lambda = 0.8386$Å. An area detector analyses the intensity of the Bragg peak profile for a given (hkl) reflection, which allows the temperature dependence of the peak-profiles to be accurately measured.
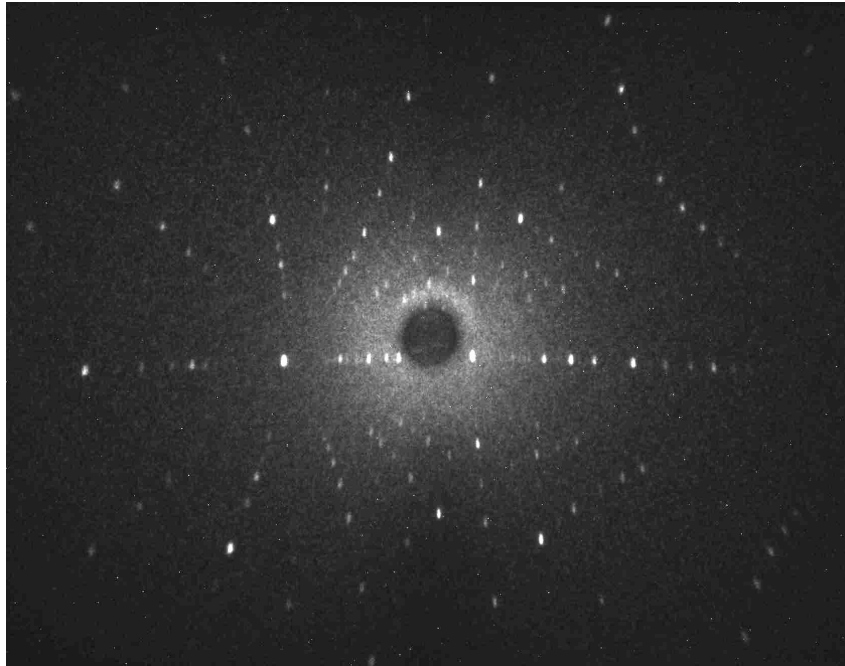
Figure 5.1: *Laue photograph of the single crystal used for D3 and D9 experiments at the ILL.*

5.3.1 D9 Experimental Details

The crystal used was a small uniform hexagonal rod, which was mounted by hand with the c-axis orientated vertically, as seen in figure 5.2. The UB (orientation) matrix was constructed from several strong reflections confirming the space group $P\bar{6}2m$. 872 reflections were measured at at T=74 K. The system was then cooled to T=2 K as at this temperature an antiferromagnetic propagation vector has been reported [1] in powder work.

The propagation vectors $\boldsymbol{k} = [\frac{1}{2}, 0, \frac{1}{2}]$, $\boldsymbol{k} = [0, \frac{1}{2}, \frac{1}{2}]$, $\boldsymbol{k} = [0, 0, \frac{3}{2}]$, $\boldsymbol{k} = [\frac{-1}{2}, \frac{1}{2}, \frac{3}{2}]$, $\boldsymbol{k} = [\frac{3}{2}, \frac{1}{2}, \frac{1}{2}]$, $\boldsymbol{k} = [\frac{3}{2}, \frac{1}{2}, \frac{1}{2}]$ were investigated around the peaks (0 0 1), (0 1 1) and (2 0 0). No extra observable peaks were found with these parameters. This is unexpected and not consistent with the analysis performed on the powder samples, reported in the previous chapter.

The temperature dependence of the integrated intensity of the ferromagnetic peak (2 1 0) was also investigated to determine the magnetic ordering

temperature. This is reported in subsection 5.3.2.3.

The final day on D9 was spent measuring 774 reflections at T=2 K.The data was processed using the ILL software 'racer', which was fine-tuned to give appropriate integrated intensities for the peak shapes measured.

Figure 5.2: *HoPtIn single crystal mounted on D9*

5.3.2 D9 HoPtIn Results and Analysis

For both the T=2 K and T=74 K data the Cambridge Crystallographic Sub-routine Library (CCSL) [43] was used for data reduction and refinement of the nuclear structure and magnetic phase. The final crystallographic input files (.cry) are included in appendix B.

5.3.2.1 D9 HoPtIn T=74 K

Of the 872 reflections measured at 74K 18 were rejected due to poor intensity owing to slight orientation errors. The data was run through the CCSL sequence of programs '$arrnge$' $\rightarrow$ '$absmsf$' $\rightarrow$ '$sflsq$'. This process grouped the crystallographically equivalent reflections and fitted the data using a least-squares method. The best fit gave a $\chi^2 = 14.1$ and a $R^2 = 2.9$ when refined using the modulus of the structure factor. A lower χ^2 was possible by imple-

menting anisotropic temperature factors, rather than the isotropic ones used in the final fit. These fits were rejected as the anisotropic temperature factors quickly became non-physical. The final refined parameters for the T=74 K data are recorded below in table 5.1. Ho_x and In_x are the refinable atomic

Variable	Refined Value	Error ($\pm$)	Units
SCALE	8.466	0.061	-
HoITF	0.025	0.053	-
InITF	0.391	0.098	-
Pt_1ITF	0.288	0.051	-
Pt_2ITF	0.877	0.079	-
Ho_x	0.5928	0.00031	[Å]
In_x	0.25982	0.00067	[Å]
MOSC	5.5	2.7	$[rad^{-1}]$

Table 5.1: *The refined values from the CCSL program 'SFLSQ'. This is for the T=74 K data.*

positions, ITF is the isotropic temperature factor and MOSC is the mosaic spread for the extinction correction. The domain radius was set to 50[nm].

5.3.2.2 D9 HoPtIn T=2 K

The 774 reflections measured were grouped into 99 sets of equivalent reflections. These were fitted using the CCSL software 'maglsq' which refines both the magnetic and structural phases. The model implemented used the dipole approximation 3.4.4 for the form factor of Holmium, and the direction of the moment was refined. The direction of the moment is defined by two angles, '$THET$' and 'PHI', as used in a spherical coordinate system. However, CCSL restricts PHI to 30° due to symmetry requirements. The magnitude of the moment is refined as two free parameters '$HoMu$' and '$HoDMu$' due to the way the dipole approximation is implemented in CCSL. '$HoMu$' is related to the spin, S and '$HoDMu$' to the orbital angular momentum L. These can be summed as $M_J = M_L + M_S$ to work out the total moment. The refined parameters are tabulated below, in table 5.2. The best fit with this model gave a $\chi^2 = 6.31$ and a $R^2 = 2.704$

Variable	Refined Value	Error $\pm$	Units
SCAL	8.18	0.045	-
Ho ITF	-0.081	0.055	-
In ITF	0.41	0.11	-
Pt_1 ITF	0.146	0.053	-
Pt_2 ITF	0.692	0.074	-
THET	-1.8	1.5	$^{\circ}$
Ho MU	7.893	0.067	μ_B
HoD MU	2.5	0.43	μ_B
MOSC	2.57	0.82	$[rad^{-1}]$

Table 5.2: *The refined values from the CCSL program 'MAGLSQ'. This is for the T=2 K data.*

The refined value of $THET = -1.8$ is unexpectedly small as a canted magnetic structure, with $THET = 25°$ has been reported for a powder investigation (see section 2.5.2). Several checks were implemented to make sure the solution was not a false minimum. A second model was implemented where the moments were confined to the c-axis. The refined values only differed from the ones above in the third decimal place, with the goodness of fit statistics being $\chi^2 = 6.27$ and a $R^2 = 2.82$. The total moment measured for the best fit was $\mu_{Ho} = 10.4 \pm 0.4\mu_B$. This agrees with that expected within the error bar, as the maximal moment is $\mu_{Ho}^{max} = 10.0\mu_B$. This could indicate that an incorrect model has been implemented. Symmetry analysis of the irreducible representations using BasIreps [1] of the $\boldsymbol{k} = [0,0,0]$ propagation vector shows that an antiferromagnetic phase is allowed, whilst being restricted to the c-axis. This magnetic representation is described by a complex phase factor, which was implemented with CCSL. The program refined the moments of the second antiferromagnetic phase to zero, and offered no better fit to the one already obtained.

---

[1]Author: Juan Rodríguez-Carvajal (LLB 2004)

5.3.2.3 D9 HoPtIn Temperature Dependence

The integrated intensity data for the (2 1 0) peak shows the temperature dependence of the magnetic phase and is plotted in figure 5.3. The onset of magnetic order is at $T_c = 20.4$ K. Morosan *et al.* find $T_c = 23.5$ K from specific heat analysis of a single crystal sample, grown in the same way as the one used here. This is further discussed in the discussion section of this chapter.
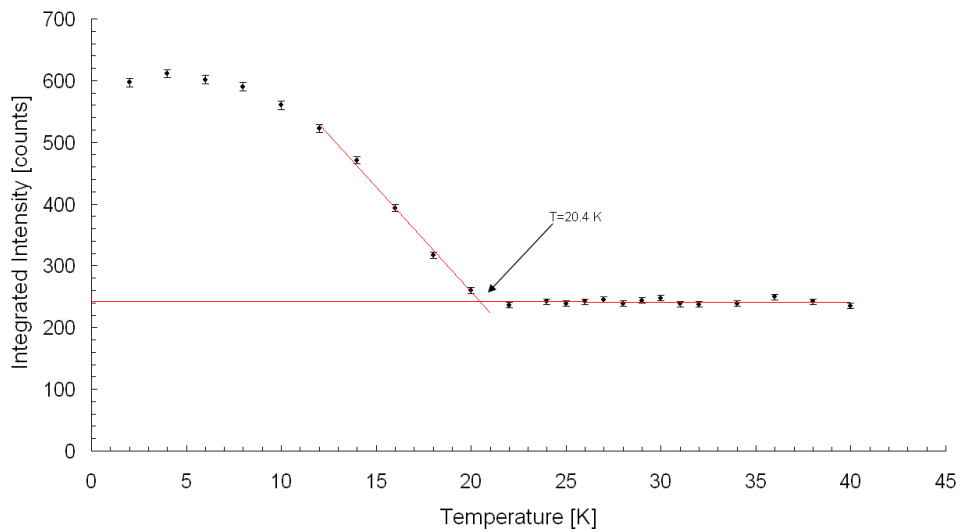
Figure 5.3: *The temperature dependence of the integrated intensity of the (2 1 0) peak measured on D9. The lines of best fit are shown in red, used to indicate the ordering temperature, T=20.4 K.*

5.4 The Spin Polarised Hot Neutron Diffractometer D3

D3 uses a continuous beam of polarised neutrons to determine a quantity known as the *flipping ratio*, R [44]. This requires the neutrons to have two polarities, up and down.
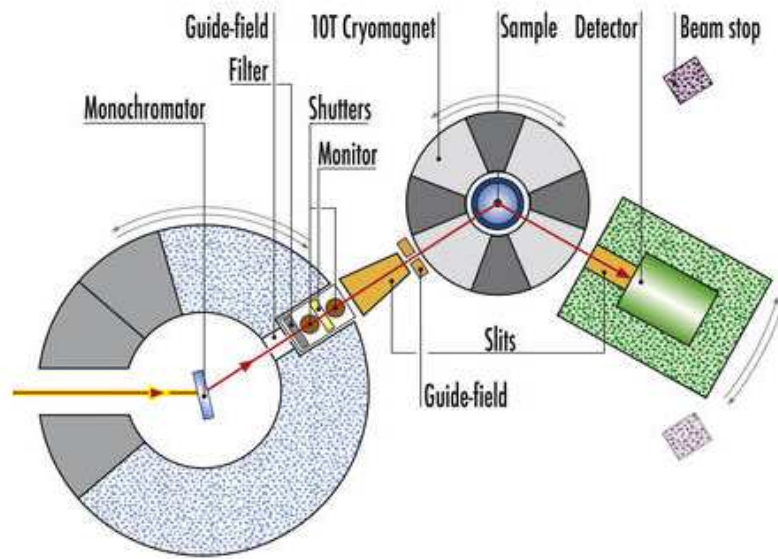
Figure 5.4: *D3 high field experimental setup showing spin polarising filters and guide field. Courtesy of the ILL.*

5.4.1 D3 Experimental Details

The sample was successfully mounted on D3 and oriented with a new UB matrix. The reflections with large structure factors were selected and arranged to minimise angular movement of the detector between measurements. The field was ramped to 9 Tesla, and the system set to T=74 K. 226 reflections were measured, although the measuring time was increased for those with a lower structure factor to ensure good statistics.

While cooling to 2K in the 9 Tesla field the sample snapped. Inspection of the crystal revealed that the rod had snapped into two pieces of about 1/3 and 2/3 of the original. The larger piece ($5[mm] \times 0.6[mm]$) was remounted. At 2K a field of 2 Tesla was applied which, according to magnetisation measurements is sufficient to fully saturate the sample in the c-direction. At T=2 K 267 reflections were measured with good statistics. As the crystal had already been torn from its mount due to the high magnetic field, it was decided to only measure in-plane reflections on this experiment. This would not hinder

the intended magnetisation density analysis as none of the atoms have the same (x,y) position, so there would be no ambiguity when viewing the a-b plane.

5.4.2 D3 Results

The 74K and 2K data sets were each grouped into equivalent reflections and a few select points removed where the sample or detector was slightly misaligned.

For a magnetisation density map reconstruction CCSL could not be used as it can not yet analyse non-centrosymmetric structures in a standard manner. A non-centrosymmetric structure does not have the inversion symmetry operator $(-x, -y, -z)$. This means the phase of the structure factor, φ is not restricted to $\varphi = 0, \pi$. Rather, φ is a non unique complex number. Because of this the magnetisation density can not be found using the usual fitting and Fourier transform. To complete this analysis *maximum entropy* [45] [46] calculations are required. For this a collaboration was initiated with Dr Janusz Waliszewski at the University of Bialystok, Poland. Using a non-uniform prior he constructed the magnetisation density for the unit cell.

Figure 5.5 shows a contour plot of the magnetisation density in the $z=\frac{1}{2}$ plane. The contour map shows that the magnetisation is highly localised on the RE sites. Full 3d rendering shows some minute oscillations away from the RE site, but not of the magnitude expected if there were an induced moment on the Pt site. This indicates that the Pt-RE interactions are negligible. The magnetisation density of the (001) plane shows no magnetism within the error bars of the measurement. This means that the Pt-In layer is non magnetic, and there is no induced magnetism away from the $z=\frac{1}{2}$ plane. From the magnetisation density map it is clear that an appreciable moment on the Pt site, which is at position (0,0,z) on the diagram, is not present.

The next part of the analysis is to examine the form factor of HoPtIn. For this SQUID magnetisation data is required for normalisation. The magnetic characterisation of the single crystal used in the D9 and D3 experiments is detailed in the next section.
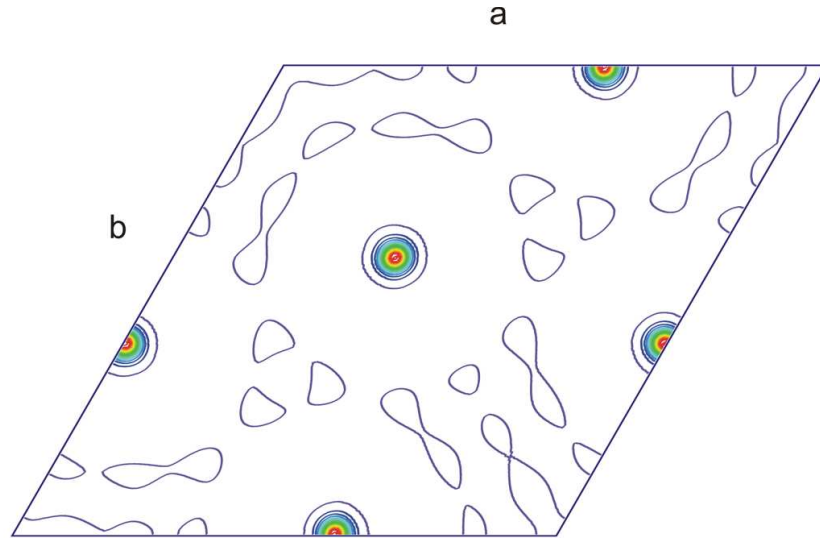
Figure 5.5: *Maximum entropy reconstruction of the magnetisation density within the unit cell in the ab plane at $z = \frac{1}{2}$. Red=maximum density, blue the lowest.*

5.4.3 HoPtIn SQUID Data

A 2.06 mg section of single crystal was mounted so that the applied field was parallel to the c-axis. It was inserted into a MPMS 5.5 Tesla SQUID magnetometer. Sixteen isotherms were taken for full magnetic characterisation. Isotherms were specifically taken at T=74 K and T=2 K to extract the moment to which the form factor should be normalised. For this, linear regression was performed on the high field region of the Arrott plots. The normalisation value was then found by solving the equation of the line for the field values used on the D3 experiment. The linear regression has the form $M^2 - a\frac{M}{B} - b = 0$ where a and b are the gradient and M-intercept respectively. The fitted vales of a and b can be read from figures 5.7 (blue diamonds) and 5.6 (green circles) for the T=2 K and T=74 K isotherm respectively. Using this method, the T=74 K, B=9 T data should be normalised to $M = 4.40\mu_B/$Ho, and the T=2 K, B= 2T data to $M = 8.85\mu_B/$Ho. The complete Arrott plots are shown in figures 5.7 and 5.6, including the linear regression fits.

The ordered magnetic moment as a function of temperature is show in figure

5.9. This data is extrapolated from the high-field part of the Arrott plots for $B = 0$. The maximal ordered moment at T=2 K is $\mu_c = 8.6\mu_B/Ho$ again showing a reduced ordered moment. This value is in reasonable agreement with that measured by Morosan *et al.* of $\mu_c = 7.81\mu_B/Ho$ [2], which was also a single crystal measurement. The small discrepancy could be due to slight misalignment of the small sample in the SQUID magnetometer. This value is also in approximate agreement with that found by Baran *et al.* [1] using neutron powder diffraction. Baran reports $\mu_c^{neutron} = 7.4 \pm 0.2\mu_B/Ho$ at T=1.5 K, for the component aligned to the c-axis. All of these measurement are inconsistent with that found form the D9 analysis using CCSL. At T=2 K the ordered was refined to be $\mu_c^{D9} = 10.39\mu_B/Ho$. Why this single crystal data should show the full Ho^{3+} moment, but powder and SQUID magnetisation does not is intriguing. Clearly further single crystal work is required, to ascertain if this was a bad measurement, or that there is a physical explanation for this result.

The magnetisation data can be extrapolated to $M = 0$ to yield a Curie temperature of $T_c = 31.1$ K. This is also shown in figure 5.9. A discussion on the wide range of reported Curie temperatures is included in the next section.

The inverse susceptibility plotted in figure 5.8 shows a linear Curie-Weiss law with a paramagnetic Curie temperature of $\Theta = 28.3$ K. The value for the paramagnetic Curie temperature also widely varies in the literature, however this result is in approximate agreement with Baran *et al.* measurement of $\Theta = 25$ K. [1].
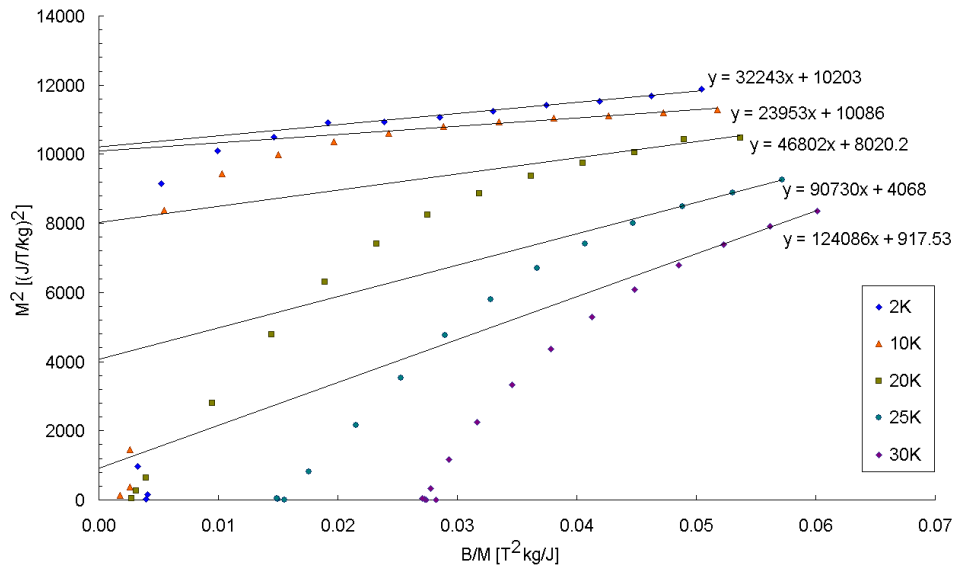
Figure 5.6: *Low temperature Arrott plots and fits for a single crystal of HoPtIn, oriented with* **B**||**c**.
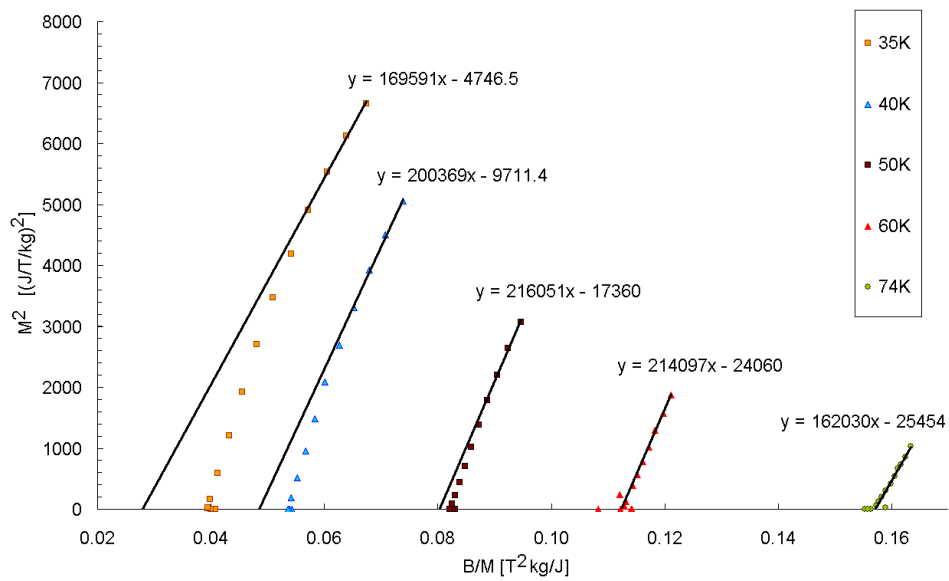
Figure 5.7: *Arrott plots above* T_c *and fits for a single crystal of HoPtIn, oriented with* **B**||**c**.
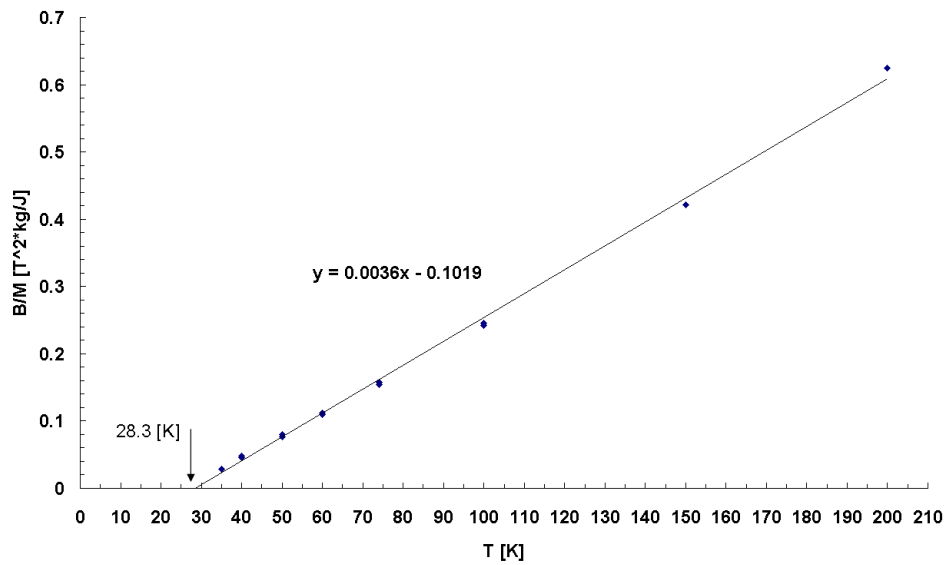
Figure 5.8: *The inverse magnetic susceptibility for a single crystal of HoPtIn, oriented with* **B**||**c**. *Θ = 28.3 is marked with an arrow. The susceptibility values were obtained from the Arrott plot fits as shown above.*
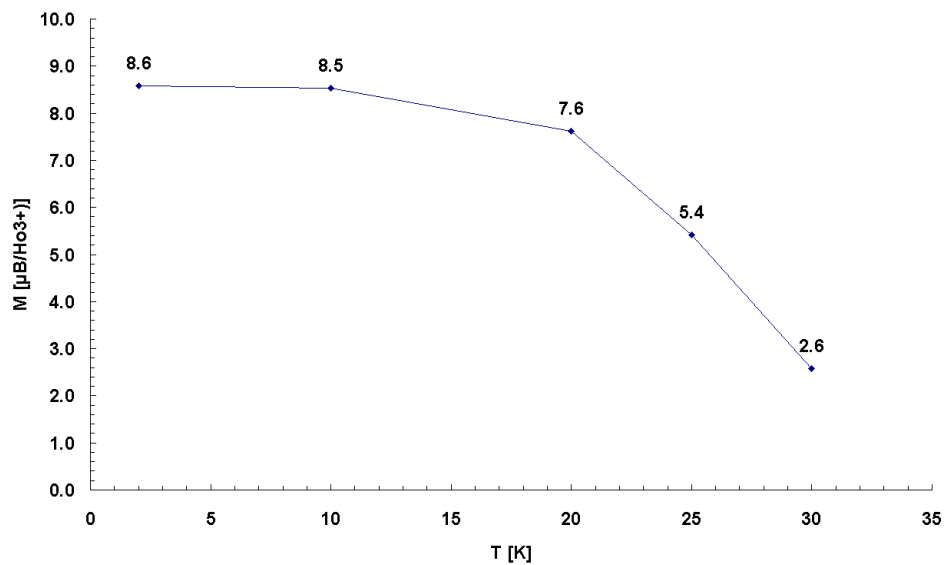
Figure 5.9: *The high field magnetisation for a single crystal of HoPtIn, oriented with* **B**||**c**. *The data was extrapolated from the Arrott plot fits as shown above. The labels next to the data points show the moment per* Ho^{3+} *in* μ_B.

5.4.4 Summary and Conclusions

The results presented in this chapter show that several of the reported theories explaining the magnetic effects observed in the REPtIn series may not be correct.

The magnetisation density map shows a highly localised moment on the Ho^{3+} site and no appreciable magnetisation density elsewhere within the unit cell. This indicates that there is no large induced moment on the Pt site, as suggested by Stephens *et al.*[4].

The 2K D9 analysis does not show a canted, reduced magnetic moment, as reported by Baran *et al.* [1], and determined in the previous chapter. In fact, this single crystal analysis shows a Ho^{3+} moment of $\mu_{Ho} = 10.4 \pm 0.4 \mu_B$, aligned parallel to the c-axis, which is the opposite to the findings of the powder data analysis. Why there should be a large difference between single crystal data and powder data is unclear.

It is also evident that the ordering temperature of HoPtIn is very sensitive to the quality of the sample and the onset criteria used. The temperature dependence of the (2,1,0) peak gives a $T_c = 20.4$K whilst the SQUID magnetisation data gives $T_c = 31$K. The values for T_c reported in the literature vary widely. Some values are shown in table 2.3 below for reference. This could indicate that the ground state and excited states of the Ho^{3+} ion are only separated by a small energy gap, and external factors can strongly influence the onset of magnetic order.

It is also unclear as to the nature of the second magnetic ordering, seen in powder neutron work by Baran *et al.* [1] and clearly seen in specific heat work done by Stephens *et al.* [4]. This was previously thought to be the onset of an in-plane antiferromagnetic phase with a propagation vector $\boldsymbol{k} = [\frac{1}{2}, 0, \frac{1}{2}]$. However this is not supported by single crystal work, where this vector was not found. The powder diffraction investigation of HoPtIn and DyPtIn presented in the previous chapter made a thorough investigation of all possible commensurate propagation vectors. This research also found $\boldsymbol{k} = [\frac{1}{2}, 0, \frac{1}{2}]$ was the the best candidate, and that the other propagation vectors were not suitable. Why the $\boldsymbol{k} = [\frac{1}{2}, 0, \frac{1}{2}]$ propagation vector should provide a suitable

Author	Experiment	Sample	Reference	T_c $[K]$
Baran *et al.*	Neutron	Powder	[1]	27
Stephens *et al.*	Magnetic Specific Heat	Powder	[4]	33
Morosan *et al.*	Specific Heat	SC	[2]	23
D.E.Pooley	SQUID $\boldsymbol{H}||c$	SC	I. I.(2,1,0)	20.4

Table 5.3: *The range in reported magnetic ordering temperature for HoPtIn. More detailed information is available in the literature review section. 'I. I.(2,1,0)' is the ordering temperature determined using the integrated intensity of the (2,1,0) peak, as discussed in section 5.3.2.3.*

model for powder diffraction data, but is not seen single crystal measurements is not clear.

The results reported in the chapter have raised some interesting questions. To help explain these observations, data on the the magnetic ground state of HoPtIn is desirable. It is possible to calculate the CEF splitting of the 4f degeneracy from the flipping ratio data taken on D3. This type of analysis is made more difficult as the structure is non-centrosymmetric. To determine the anisotropic form factor, and characterise the CEF scheme, the development of code for data analysis is required. This involves coding the full multipole expansion of the form factor, as described in section 3.4.3. The code for this calculation was written and fully tested, and is described in chapter 6.

Chapter 6

Form Factor Analysis for HoPtIn

6.1 Motivation for Form Factor Analysis

The magnetisation density analysis of HoPtIn showed highly localised Ho^{3+} moments. As there are no adequate explanations for the 'reduced moment' observed in the REPtIn series, and an induced moment on the Pt site now seems to be unlikely, the effects of the crystal field parameters must be investigated. For some compounds, for example where the point symmetry is cubic, this analysis is well documented and straightforward. However, the $m2m$ point symmetry of the Ho^{3+} site means that the full crystal field hamiltonian must be used, as described in section 2.4.

The standard way to calculate the extent of crystalline electric field (CEF) splitting is to perform an inelastic neutron scattering experiment. If measurements are made at several temperatures, at the appropriate neutron energy, it should be possible to extract the energy level scheme [47]. This can then be used to fit the CEF B-coefficients, determining the CEF splitting. This type of measurement was performed by Kristin Neumann (private communication) at several temperatures on HET at ISIS. The neutron spectrum for T=38, 55 and 90 K is plotted below in figure 6.1, in which HoPtIn is in the paramagnetic phase.
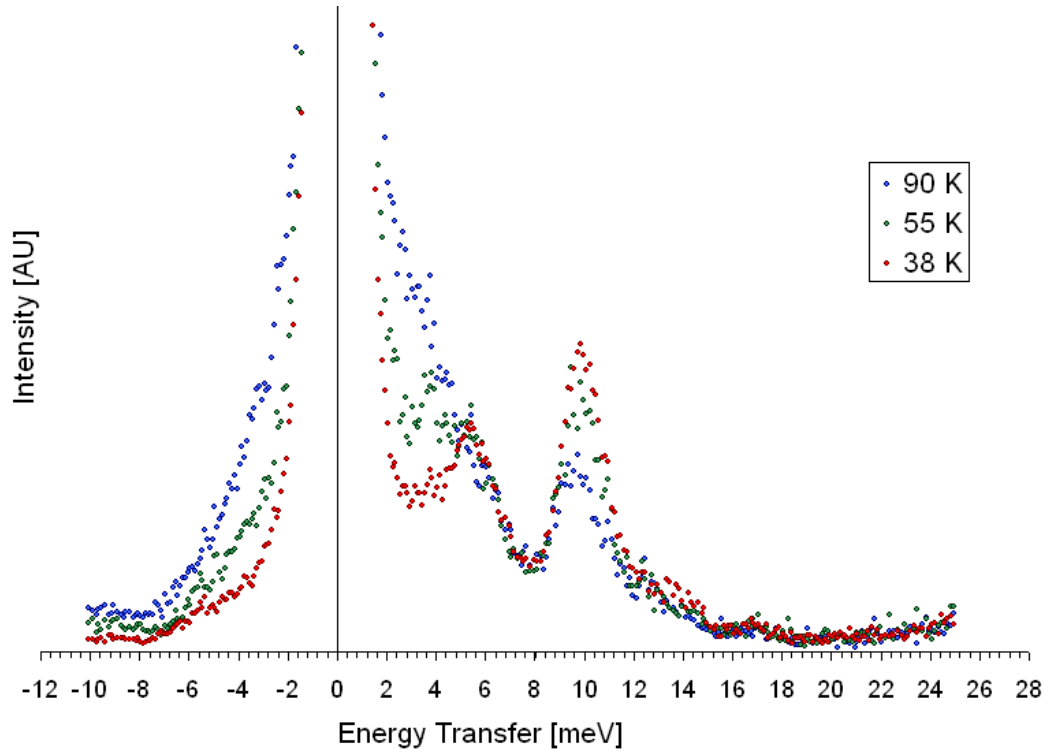
Figure 6.1: *The inelastic spectrum of HoPtIn at incident energy = 30 meV. T=38, 55 and 90 K. [K. Neumann, private communication]*

This spectrum does not contain many peaks, and the information one can gather is minimal. There is possibly a broadening around the elastic peak and two further peak at 5.5 meV and 10 meV. As the CEF hamiltonian requires 6 coefficients, and the Ho^{3+} is in a $J = 8$ state, there are 136 independent coefficients in the model for the CEF splitting. Any attempt to fit this model to such featureless data is impossible. The low temperature data, where HoPtIn has ordered ferromagnetically, shows more structure than the high temperature data. This is plotted below in figure 6.2. In this plot there are three peaks located at 8 meV, 11 meV and 15 meV. However, the peaks at 8 meV and 11 meV are the same peak, split by the internal magnetic field. The addition of the internal magnetic field further complicates the analysis, and it was not possible to gain any definite information about the CEF slitting from this data.
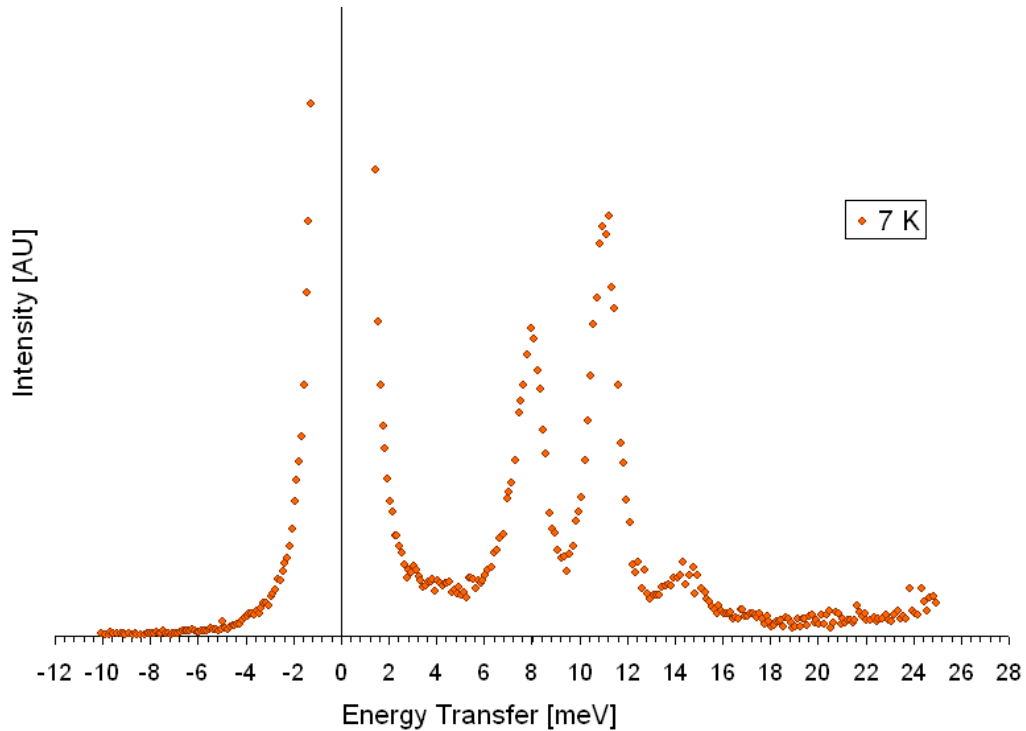
Figure 6.2: *The inelastic spectrum of HoPtIn at incident energy = 30 meV. T=7 K. [K. Neumann, private communication]*

As such, polarised neutron measurements on a single crystal sample are the only way to determine the CEF splitting accurately [48] [49] [50] [51]. However, as this structure is non-centrosymmetric the magnetic and nuclear structure factors are complex, thus further complicating this analysis. It should be noted that once the CEF slitting has been determined from polarised neutron analysis, the energy splitting should exactly fit this inelastic data.

The key difference between the analysis done so far and the determination of the CEF splitting is that the multipole expansion discussed in section 3.4.3 must be implemented. This chapter is concerned with the coding of a refinement programme using the multipole expansion to determine the a_M coefficients. This includes the extraction of the isotropic form factor for Ho^{3+} from the flipping ratio data.

C_{2v}	E	C_2	σ_v	$\sigma_{v'}$
Γ_1	1	1	1	1
Γ_2	1	-1	1	-1
Γ_3	1	1	-1	-1
Γ_4	1	-1	-1	1

Table 6.1: *The character table for C_{2v} point symmetry.*

6.2   Analysis of Ho³⁺ in C_{2v} Symmetry

The wavefunction for the multipole expansion of the $4f$ shell is expressed in terms of spherical harmonics, Y_{lm} shown below:

$$\Psi_{4f} = \sum_{l=0}^{6} \sum_{m=-l}^{+l} a_{lm} Y_{lm}(\theta, \phi) \tag{6.2.1}$$

The spherical harmonics that contribute to the electronic hamiltonian preserve the symmetry of the point group of the Wyckoff site. This symmetry can be analysed to greatly simplify the combination of allowed electronic eigenfunctions.

The Ho³⁺ ion is located on a Wyckoff site with C_{2v} ($m2m$) symmetry. This symmetry has 4 possible irreducible representations given in the character table 6.1 below.

The character of the symmetry operation can be used in conjunction with the spherical harmonics to determine which combinations of the a_{lm} are non zero. Any state $|J, m_J>$ (or combinations of states) with $a_{lm} = 0$ by symmetry will not appear in the final electronic hamiltonian. For HoPtIn, for which $J = 8$, the free atom has a 17-fold degeneracy, the following results are obtained.

Γ_1 is generated by 5 eigenstates

$$(1) = \frac{1}{\sqrt{2}}(|8,8> +|8,-8>)$$

$$(2) = \frac{1}{\sqrt{2}}(|8,6> +|8,-6>)$$

$$(3) = \frac{1}{\sqrt{2}}(|8,4> +|8,-4>)$$

$$(4) = \frac{1}{\sqrt{2}}(|8,2> +|8,-2>)$$

$$(5) = |8,0>$$

Γ_2 is generated by 4 eigenstates

$$(1) = \frac{1}{\sqrt{2}}(|8,8> -|8,-8>)$$

$$(2) = \frac{1}{\sqrt{2}}(|8,6> -|8,-6>)$$

$$(3) = \frac{1}{\sqrt{2}}(|8,4> -|8,-4>)$$

$$(4) = \frac{1}{\sqrt{2}}(|8,2> -|8,-2>)$$

Γ_3 is generated by 4 eigenstates

$$(1) = \frac{1}{\sqrt{2}}(|8,7> +|8,-7>)$$

$$(2) = \frac{1}{\sqrt{2}}(|8,5> +|8,-5>)$$

$$(3) = \frac{1}{\sqrt{2}}(|8,3> +|8,-3>)$$

$$(4) = \frac{1}{\sqrt{2}}(|8,1> +|8,-1>)$$

Γ_4 is generated by 4 eigenstates

$$
\begin{aligned}
(1) &= \frac{1}{\sqrt{2}}(|8,7> - |8,-7>) \\
(2) &= \frac{1}{\sqrt{2}}(|8,5> - |8,-5>) \\
(3) &= \frac{1}{\sqrt{2}}(|8,3> - |8,-3>) \\
(4) &= \frac{1}{\sqrt{2}}(|8,1> - |8,-1>)
\end{aligned}
$$

The mixing of these basis functions with a given Γ_i remains to be determined experimentally. However, the crystal field can only ad-mix states within a given Γ_i, but not between them, as this would be incompatible with the symmetry of the point group.

The determination of the magnitude of the a_{lm} coefficients is facilitated by using the model described in the next section.

6.3   Implementation and Coding of Flipping Ratio Analysis

The analysis of the multipole expansion of Ho^{3+} requires coding of the expressions introduced in section 3.4.3. This includes spherical harmonics, 3j symbols, structure factors and refinement procedures to determine the a_M coefficients. The code was written in *Maple 12*, [1] as this platform offers robust mathematical capabilities. It should be noted that this language can be computationally demanding and slow code-execution times were an issue. Based on our current working assumptions the equations for elastic, coherent, non-spin-flip scattering from a saturated ferromagnet will be implemented within the J-manifold. The equations used are taken from section 11.6, in the book of Lovesey [30].

---

[1] ©Maplesoft, a division of Waterloo Maple Inc. 2010

The flipping ratio data, R, measured on D3 was of the form:

$$R(\boldsymbol{\kappa}) = \frac{I_+}{I_-} = \left(\frac{|F_N + F_M|}{|F_N - F_M|} \right)^2 \tag{6.3.1}$$

where $F_N(\boldsymbol{\kappa})$ and $F_M(\boldsymbol{\kappa})$ are the nuclear and magnetic structure factors, respectively, and were introduced in chapter 3. Any common factor to these expressions, such as temperature or extinction corrections, cancel out.

For HoPtIn the nuclear and magnetic structures are non-centrosymmetric. This yields complex structure factors. The additional need to identify the phase factor of the structure factors $F_{(N,M)} = |F_{(N,M)}|e^{i\varphi_{(N,M)}}$, complicates this analysis considerably. The flipping ratio model can be coded, but not in a straightforward way due to the complex structure factors. For this the parameters determined from the D9 analysis have been used. It is then possible to fit the a_M coefficients to the data set weighted by the experimental error bars. As the flipping ratio data does not have any obvious structure when plotted, it was desirable to extract the Ho^{3+} form factor from the flipping ratio data. Such a process, if possible at all, would eliminate the problem provided by the non-centrosymmetric structure. The method developed to achieve this is discussed in the next section along with the results. It may also be possible to fit the a_M coefficients to the extracted form factor, rather than the flipping ratio. Whether or not this yields a unique result depends on the structure of the form factor data and the number of a_M coefficients required. Performing the fitting of the a_M coefficients in this way offers visual identification of possible bad data points. It also allows the identification or any angular dependence of the form factor that is not due to the Ho^{3+}, such as scattering from elsewhere in the unit cell.

6.3.1 MAPLE Implementation

The Maple implementation of the flipping ratio analysis resulted in over 35 pages of code, all of which is included in appendix C.2 along with notes on the notation used. As points of interest, the coding of the 3j symbols, the matrix elements and the extraction of the form factor are discussed next.

Extraction of the Ho^{3+} form factor from R. The magnetic structure factor F_M can be cast into the form $F_M = |\boldsymbol{m}| f(\boldsymbol{\kappa}) \mathbb{F}_M$. Here $\boldsymbol{m}$ is the magnetic moment, as obtained for example from SQUID data, $f(\boldsymbol{\kappa})$ is the atomic form factor and $\mathbb{F}_M$ is the structure factor describing the position of the magnetic Ho^{3+} ions. F_N and F_M can be complex, so care must be taken when evaluating the modulus. To simplify notation $|\boldsymbol{m}| f(\boldsymbol{\kappa})$ is relabel 'X', as $\boldsymbol{m}$ is a scaling factor for which normalisation is performed. The flipping ratio becomes:

$$R(\boldsymbol{\kappa}) = \frac{I_+}{I_-} = \left| \frac{F_N + |\boldsymbol{m}| f(\boldsymbol{\kappa}) \mathbb{F}_M}{F_N - |\boldsymbol{m}| f(\boldsymbol{\kappa}) \mathbb{F}_M} \right|^2$$

$$= \left| \frac{F_N + X \mathbb{F}_M}{F_N - X \mathbb{F}_M} \right|^2 \tag{6.3.2}$$

This equation was solved for X for each reflection using the MAPLE built-in 'solve' function. As equation 6.3.2 contains a 'modulus-squared', the solution for X may not be unique. As such, each calculation was individually inspected for the correct root. The criteria for determining a 'correct' root was that the root should lay on a smooth curve. This is only valid for reflections of the type (h,k,0), as these reflections are not sensitive to the magnetic anisotropy. This 'smooth curve' should be similar in shape as that seen for the dipole approximation, which was plotted in figure 3.2, section 3.4.2. As R is a ratio, any common factors to $F_N(\boldsymbol{\kappa})$ and $F_M(\boldsymbol{\kappa})$, such as a scale factor or temperature corrections will be cancelled out. As such, the flipping ratio contains the intrinsic value of the magnetic moment from which the neutron scatters. Using this method to extract X from the flipping ratio means that X contains the size of the magnetic moment. This means that as $\boldsymbol{\kappa} \to 0$, the plot of X should tend to the magnitude of the magnetic moment for the Ho^{3+} ion. The magnitude of the magnetic moment for T=74 K and B=9 T has already been determined from the high field Arrott plot data in section 5.4.3. This was calculated to be $\mu_c^{Norm} = 4.40 \mu_B/$Ho. This provides a second criterion for selecting the correct root, that of $0 \mu_B < X < 4.5 \mu_B$.

Figure 6.3 shows four examples of the calculation for determining X. These examples illustrate the advantages and disadvantages of using this method. The four sub-figures in figure 6.3 are labelled (1) through (4) and are discussed

individually.

Sub-figure (1) shows the calculation for the (6,-3,0) reflection. This is the 'ideal' case, in which there is only one root within physical bounds, $0\mu_B < X < 4.5\mu_B$. The root was found to be $X^{(6,-3,0)} = 2.07\mu_B$/Ho. This plot also shows how the error bar was determined for X. The error on X was calculated analytically by performing a linear regression to $R_{calculated}$ around the solution for X. This was then extrapolated over the range of the error bars for the measured values of R to give $\pm\delta X$. In the plot the linear regression is shown in brown. The $\pm$ bounds for $R_{measured}$ are shown as two green lines.

Sub-figure (2) shows the (5,-2,0) reflection. For this reflection no simple roots are found. This was the case for 12 reflections, which were removed from the data set. However, it should be noted that in every instance when a root was not found, $R_{calculated}$ was within the error bar of $R_{measured}$. This implies that the reduction of the flipping ratio to the magnetic Ho^{3+} form factor can not readily be performed using the present method without the introduction of further assumptions. The reflections that did not produce a root were investigated for any systematic pattern, such as a simple κ dependence, or on the size of the $R_{measured}$ values. No such dependence was found. It would appear that the occurrence of the reflections that do not have a root are effectively random.

Sub-figure (3) shows the (7,-3,0) reflection. In this plot it is clear to see that there are two possible roots. Both of these are valid under the criteria $0\mu_B < X < 4.5\mu_B$. To determine the correct root here the full data set has to be plotted. It is only when an overview of the whole data set is given that this type of outlier can be identified. In this case, to achieve a smooth form factor the root at $X^{(7,-3,0)} = 3.49\mu_B$/Ho was used. This plot also shows the linear regression for error bar determination, which in this case has a negative gradient.

Sub-figure (4) shows the (9,-1,0) reflection. This reflection was outside of the criteria $0\mu_B < X < 4.5\mu_B$. However, a root was found within the error bar of the measurement. The value of this root is $X^{(9,-1,0)} = -0.16\mu_B$/Ho. This value was included in the data set used. The justification for this is that any fit performed used the weighting least squares method. As the weights are

$w = \frac{1}{\delta X^2}$ this measurement should be properly accounted for.

The results of this procedure are reported in the next section, where the extracted form factor is plotted and analysed.
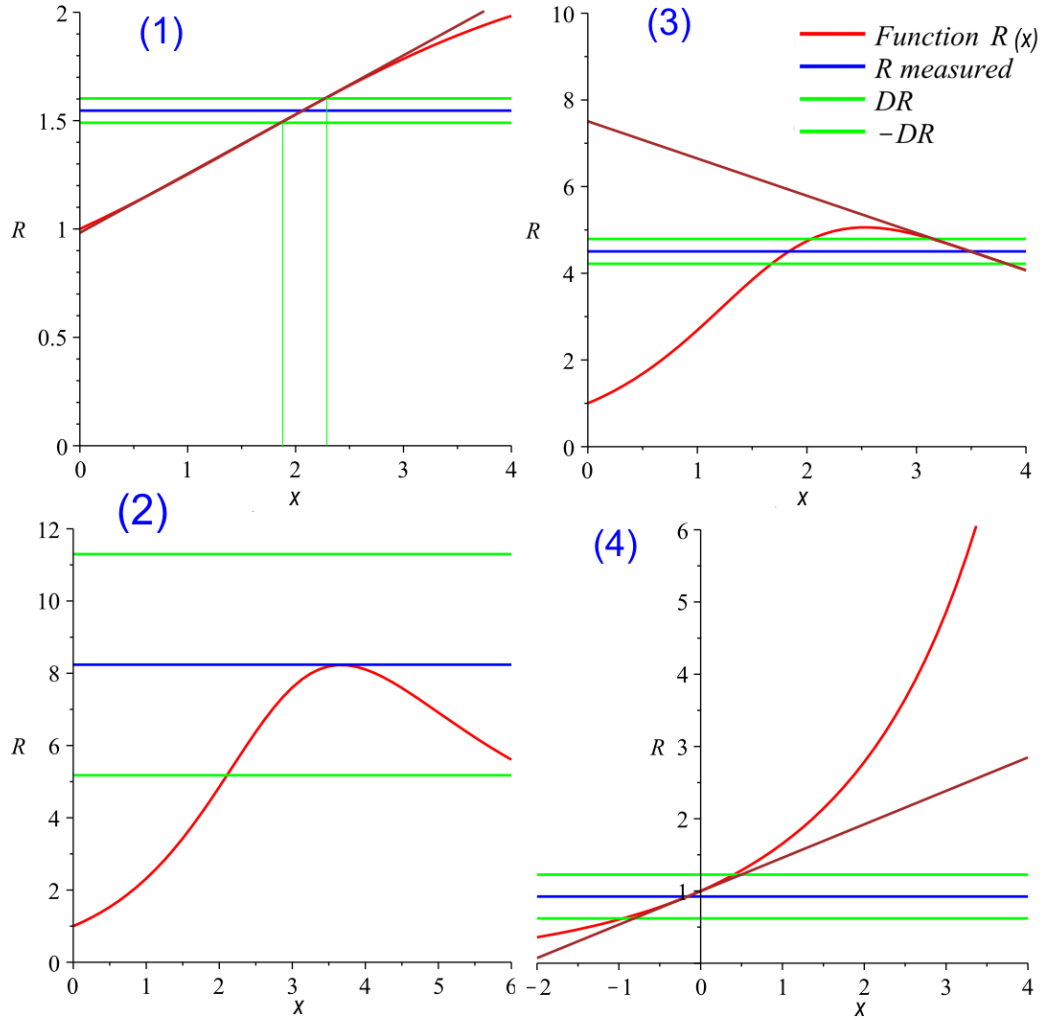
Figure 6.3: *Four example plots showing the determination of the solution for X by inspection. In these plots the double green lines indicate the upper and lower bounds of the error-bars, δR and δX. Sub-figures 1, 2, 3 and 4 are for reflections (6,-3,0), (5,-2,0), (7,-3,0) and (9,-1,0), respectively. These plots are discussed in detail in the main text.*

Coding the 3j symbols. The 3j symbols are defined in section 3.4.3, and are required to evaluate the matrix elements for magnetic scattering. The algebraic form of the 3j symbols means that certain precautions must be implemented when programming a function which evaluates them. They are defined as:

$$
\begin{aligned}
&\left(\begin{array}{ccc} j_1 & j_2 & j_3 \\ m_1 & m_2 & m_3 \end{array} \right) \\
&= \; (-1)^{j_1 - j_2 - m_3} \left[\frac{(j_1 + j_2 - j_3)!(j_2 + j_3 - j_1)!(j_3 + j_1 - j_2)!}{(j_1 + j_2 + j_3 + 1)!} \right]^{\frac{1}{2}} \\
&\times \; \sum_{\kappa} (-1)^{\kappa} \frac{\sqrt{(j_1 + m_1)!(j_1 - m_1)!(j_2 + m_2)!}}{\kappa!(j_1 + j_2 - j_3 - \kappa)!(j_1 - m_1 - \kappa)!(j_2 + m_2 - \kappa)!} \\
&\times \; \frac{\sqrt{(j_2 - m_2)!(j_3 + m_3)!(j_3 - m_3)!}}{(j_3 - j_2 + m_1 + \kappa)!(j_3 - j_1 - m_2 + \kappa)!}
\end{aligned}
\tag{6.3.3}
$$

The 3j symbols have to be coded in such a way as to never attempt to evaluate a negative factorial. The first terms containing factorials in equation 6.3.3 are:

$$
\underbrace{(j_1 + j_2 - j_3)!}_{(1)} \underbrace{(j_2 + j_3 - j_1)!}_{(2)} \underbrace{(j_3 + j_1 - j_2)!}_{(3)}
$$

which, in order to avoid a negative factorial, require the conditions:

$$
\begin{aligned}
(1) & \quad j_1 + j_2 \geq j_3 \\
(2) & \quad j_2 + j_3 \geq j_1 \\
(3) & \quad j_3 + j_1 \geq j_2
\end{aligned}
$$

These inequalities are known as the 'triangle condition' as $j_{1,2,3}$ are restricted to certain values. The triangle condition is written as a delta function,

$$
\Delta(j_1, \; j_2, \; j_3) = \left\{ \begin{array}{ll} 1 & \textit{for a triangle of integral perimeter} \\ 0 & \textit{otherwise} \end{array} \right\}
\tag{6.3.4}
$$

6.3.4 was implemented in the Maple code as a series of IF statements. On examination of the second Clebsch Gorden coefficient in equation 3.4.14, it can be seen that gives $j_1 = K'', j_2 = K', j_3 = 1$. Condition (3) is violated for the $(K'', \ K')$ pairs $(0,3)(0,5)(0,7)(2,5)(2,7)$ and Condition (2) for the pairs $(4,1)(4,7)(6,1)(6,3)(8,1)(8,3)(8,5)$. As such, a set of IF statements within the loop over K' is advantageous to reduce computation demands. These are constructed so the code is only executed, if the triangle conditions are met.

```
if  (K''+K' >=1) and (K'+1 >=K'') and (1+K'' >=K') then
        {execute code}
end if;
```

Further to these triangular conditions, the criteria for addition of the m quantum numbers must be implemented. m_3 is the sum of the two angular momenta being coupled, so $m_3 = m_1 + m_2$. This condition can be implemented for the second Clebsch Gorden coefficient as $q = 0$, meaning $Q'' + Q'$ must equal zero. This is clearly only true when $Q'' = -Q'$ or $Q' = -Q''$. This can be implemented in the loop over Q' as

```
if  (Q'+Q''=0)  then
   {execute code}
end if;
```

Testing the scattering in the forward direction. The multipole expansion describes the scattering between two given $|J, m_J >$ states expressed as matrix elements of the type $< J, m_J | \hat{\mathbf{Q}}_\perp | J', m'_J >$. As discussed in section 3.4.4 the scattering in the forward direction is proportional to the moment of this state. For elastic scattering $|J, m_J >= |J', m'_J >$ so the matrix elements should be proportional to the m_J value for that state. For Holmium, $J = 8$ giving 17 possible m_J values. These were plotted as a function of scattering vector and are shown below in figure 6.4. It is clear to see that the scattering contribution, as $\boldsymbol{\kappa} \to 0$, is proportional to the magnetic moment of the given state. The maximal ordered moment from matrix element $< 8, 8 | \hat{\mathbf{Q}}_\perp | 8, 8 >$ is $10 \mu_B$ as expected.
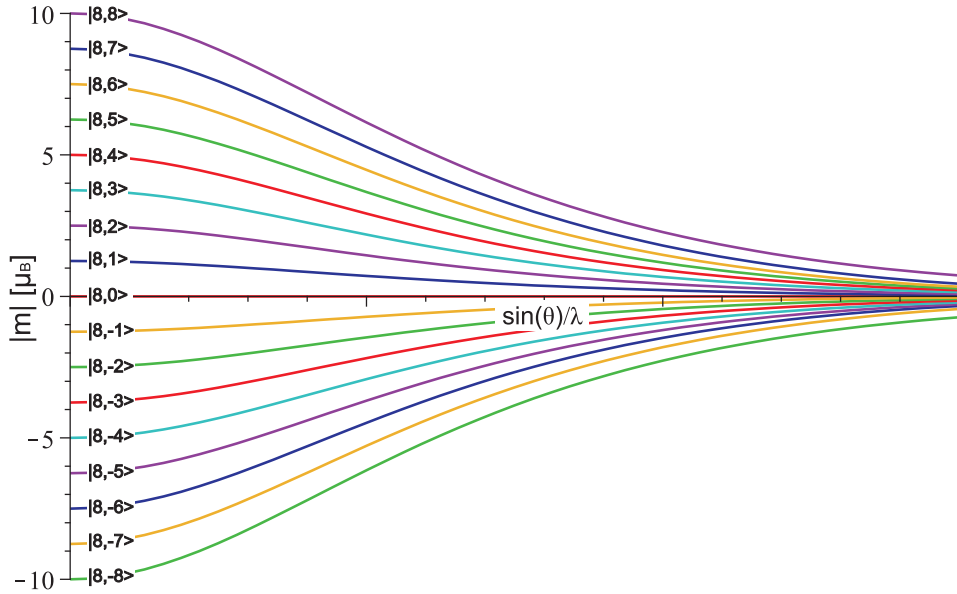
Figure 6.4: *The $sin(\theta)/\lambda$ of the multipole matrix elements. The magnitude of the scattering is proportional to the moment of the scattering state.*

6.3.2 Flipping Ratio Analysis Results

The 74K data for the D3 experiment is reported below. As previously discussed this data was taken for scattering within the basal plane, so all Miller indices were of the form $(h, k, 0)$. This means that of the possible 60 spherical harmonic functions, $Y_{Q''}^{K''}$, used in the full multipole expansion only those will be included that do not have a $cos(\theta)$ multiplier. This is due to the geometry of basal plane scattering where $\theta = 90°$. The consequence of this is that the Ho^{3+} form factor is isotropic, and as such a smooth, continuous function is expected. The D3 data presented below is used as a test for the code written.

6.3.2.1 Flipping Ratio Model

Fitting the flipping ratio data requires the refinement of the 16 a_M coefficients. This proved problematic for the least-squares refinement, as there were many local minima all with similar χ^2 values. Because of this, it was not possible to pick one unique a_M-scheme over another, and thereby one irreducible rep-

resentation. Plotted below in figure 6.5 is one of the best fits obtained for the flipping ratio at T=74 K. It is clear to see that the lower R-value points are fitted well. Nearly all measured points (red) below R=5 are well fitted within the error bar. This is not true for those reflections with higher R value where several points are poorly fitted. There does not seem to be any systematic reason for this, such as a simple κ dependance. Because of these difficulties a new approach had to be adopted. The aim of this approach was to extract the Ho^{3+} form factor from the flipping ratio data. For this the method introduced and described in section 6.3.1 was used, in which a solution for 'X' is determined.
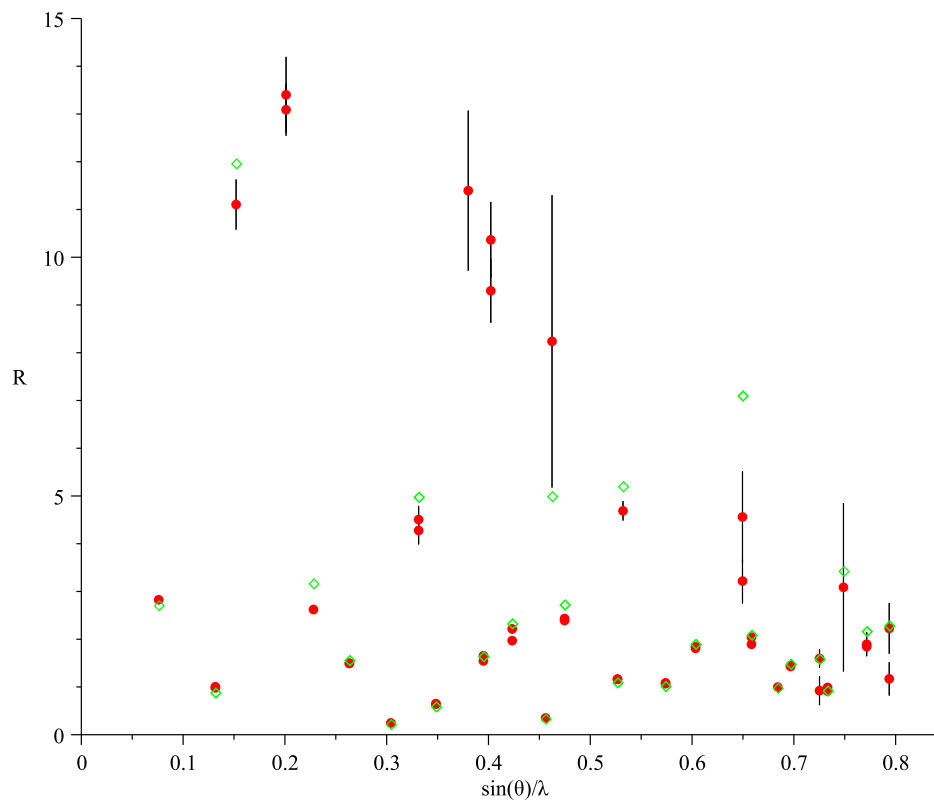
Figure 6.5: *Plot of the measured (red circles) and calculated (green diamonds) flipping ratio values, R, at 74K. The green diamonds were calculated using* $\Gamma_1 + \Gamma_2$' *from table 6.2 below. The experimental error bars are shown as black lines.*

m_J	-8	-7	-6	-5	-4	-3	-2	-1	0	1	2	3	4	5	6	7	8	χ^2
$\Gamma_1+\Gamma_2$	-	0.33	-	0.65	-	0.22	-	0.65	-	-	-	-	-	-	-	-	-	30.8
$\Gamma_3+\Gamma_4$	-	-	0.24	-	0.81	-	0.54	-	-	-	-	-	-	-	-	-	-	41.2

Table 6.2: *The normalised values for the a_m coefficients used to produce figures 6.6 and 6.7. These are constructed to be consistent with the possible wavefunctions found in section 6.2 by considering the IR of the point group.*

6.3.2.2   Multipole Form Factor Analysis

The form factor is assumed to be that of the Ho^{3+} site only. The solution for X was found by inspection of each data point, as discussed previously. It should be noted that some data points had no solution within physical values, and some had no solution at all. However, this method of solving for 'X' is advantageous as it allows the form factor to be extracted despite the problems caused by the non-centrosymmetric structure. That not all reflections could be included may indicate that the model is not fully appropriate, but that it is a good first approximation. Further to this, once the form factor is calculated from this reduced data set, the fitted model can be used to calculate the flipping ratio for the *full* data set. In the following form factor analysis 15 data points out of 50 were not included.

The contribution of each $|J, m_J >$ state to the scattered intensity is described by one a_M coefficient only. The optimal coefficients obtained by fitting to the form factor data are shown below. As an example a second a_M-scheme constructed to be consistent with a different irreducible representation is tabulated. The difference between the goodness of fit between $\Gamma_1+\Gamma_2$ and $\Gamma_3+\Gamma_4$ (derived in section 6.2) is small. The two different form factors produced with these sets of a_M coefficients are plotted in 6.6 and 6.7. The form factor has been normalised to the magnetisation value taken from the 74 K isotherm at high fields, which was plotted in section 5.4.3 in figure 5.7.
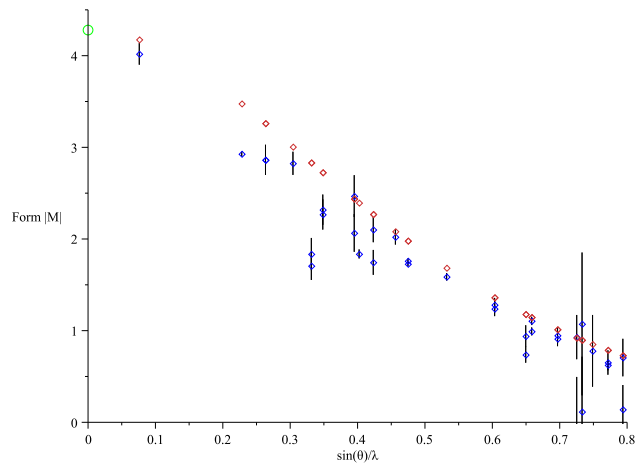
Figure 6.6: *Plot of the Ho^{3+} form factor extrapolated from the measured flipping ratio data. The model (red diamond) was calculated using 'Γ$_1$ + Γ$_2$' from the table. The measured form factor (blue) shows the experimental error bars as black lines.*
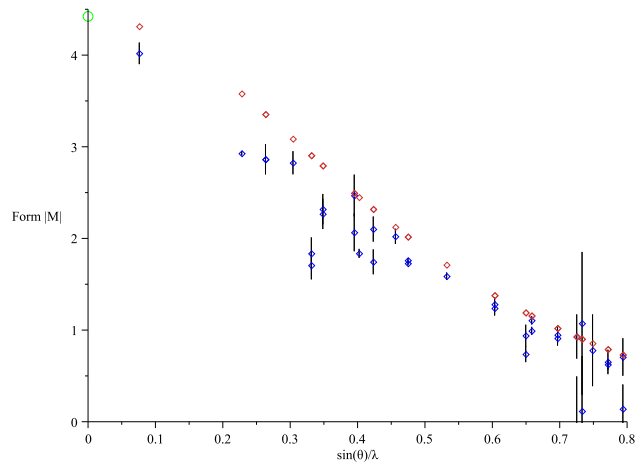
Figure 6.7: *This model (red diamond) was calculated using 'Γ$_3$ + Γ$_4$' from the table and is shown to demonstrate the difficulty in determining the correct set of a_M coefficients.*

6.3.2.3   Approximation for Form Factor Analysis

The analysis of the Ho^{3+} form factor using the full multipole expansion did not provide a unique solution. This is because the least-squares fit of the a_M coefficients is an under-determined problem. To further the form factor analysis a second model was developed that has fewer independent parameters. This model is reported in a book chapter by O. Moze [47]. This simplified model groups together all the coefficients appearing in form of the radial functions, $< j_n >$, seen in the multipole expansion to just three. This new model has the form:

$$X = |\boldsymbol{\mu}_c|(f(\boldsymbol{\kappa}) = |\boldsymbol{\mu}_c| < j_0(\boldsymbol{s}) > +f_2 < j_2(\boldsymbol{s}) > +f_4 < j_4(\boldsymbol{s}) > +f_6 < j_6(\boldsymbol{s}) >)$$

$$(6.3.5)$$

where $s = \frac{sin(\theta)}{\lambda}$ and f_2, f_4, f_6 are the model parameters. $\boldsymbol{\mu}_c$ is the moment used for normalisation calculated earlier to be $\mu_c^{Norm} = 4.40\mu_B/Ho$. Another advantage of this model is that it is automatically normalised to the correct value as $< j_2(\boldsymbol{s}) >, < j_4(\boldsymbol{s}) >$ and $< j_6(\boldsymbol{s}) >$ all equal zero at $\frac{sin(\theta)}{\lambda} = 0$. This model does not give any information on the CEF parameters, or the magnetic anisotropy. However, it does provides the weight, with which the individual radial functions contribute to the magnetic Ho^{3+} form factor. Using the 'NonlinearFit' routine within *MAPLE* the three coefficients were refined to be:

$$
\begin{aligned}
f_2 &= & \text{-9.136} & \quad \pm 0.183 \\
f_3 &= & 72.078 & \quad \pm 3.162 \\
f_4 &= & \text{-142.3778} & \quad \pm 10.865
\end{aligned}
$$

The fit produced with this model is displayed below in figure 6.8. For this fit, $\chi^2 = 2.9$. Overall the fit seems to be a good approximation to the data set. The points with the small error bars are fitted well, and the general trend is well described. It can bee seen that the experimental data is very close to the normalisation value as $\frac{sin(\theta)}{\lambda} \to 0$.

Using this model for the form factor, the flipping ratio can be calculated and compared to the experimental data. A plot of this is shown below for
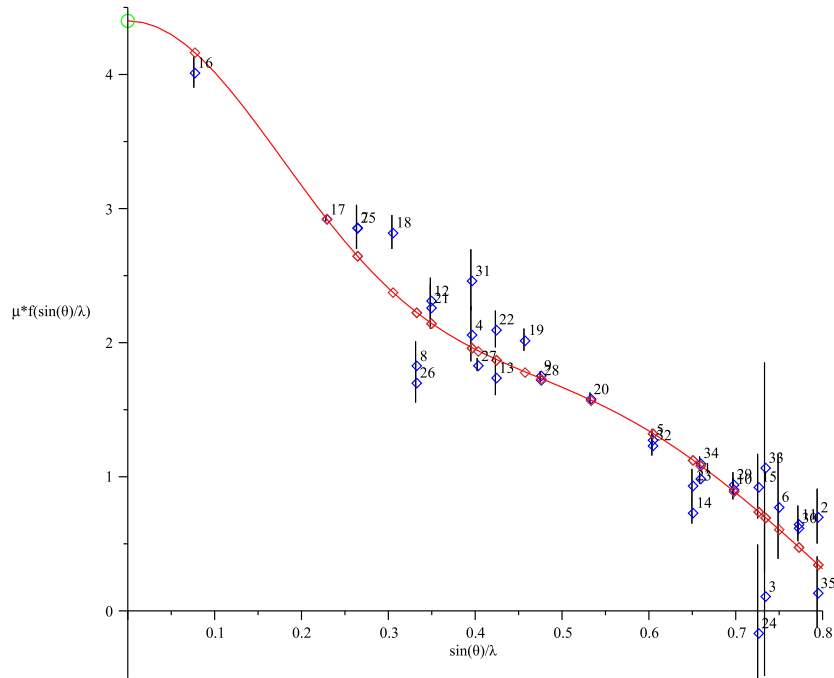
Figure 6.8: *This model (red diamonds and red line) was calculated using the coefficients f_2, f_4, f_6 and the simple model described above. The experimental data is shown in blue. The green circle indicates the normalisation value, $\mu_c^{Norm} = 4.40\mu_B/Ho.$*

the T=74 K data in figure 6.9. The data points with a R value less than R=5 are well fitted within the error bar. This is not true for those reflections with higher R values, where there are several points in disagreement. This disagreement is surprising, as the form factor should produce a good model. To try to determine the reason behind the badly modelled data points, the κ dependence was investigated. This investigation did not reveal any angular dependence for the badly fitted data points. The data used to produce figure 6.9 is tabulated in appendix D. This table also includes the difference between the measured and observed flipping ratio data, the modulus of the nuclear and magnetic structure factors and the calculated form factor for completeness.
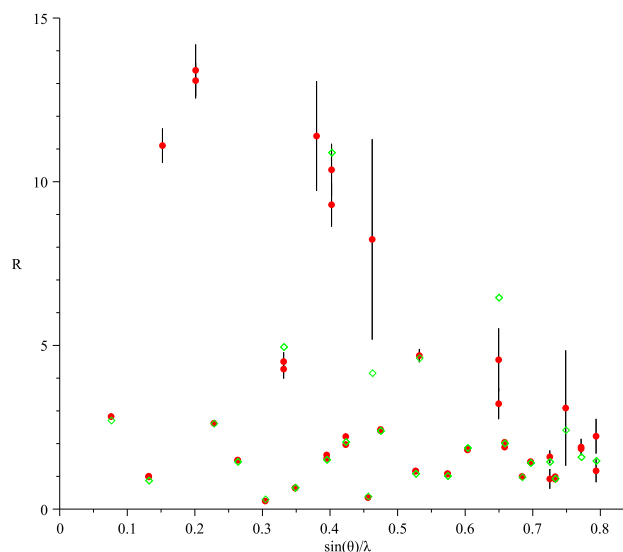
Figure 6.9: *The flipping ratio calculated using the model form factor. The red dots are the measured values with error bars.*

6.3.3 Summary and Conclusions

The code for analysing anisotropic form factors has been written and tested. This involves the calculation of the multipole expansion of the form factor, and the use of least-squares fitting routines. The fitting of the flipping ratio data did not yield a conclusive and unique crystal field configuration. To continue the analysis a new method for the calculation of the form factor from the flipping ratio measurements was developed. This analysis allowed the $\frac{sin(\theta)}{\lambda}$ dependence of the Ho^{3+} form factor to be plotted.

Further attempts to fit the full multipole expansion to the Ho^{3+} form factor were non-conclusive. Because of this, the model was further simplified to be a function of three independent coefficients. This provided a good model fitting the experimental data well. The best fit had a $\chi^2 = 2.9$. This model showed that the form factor calculated from the flipping ratio agrees well with the magnetic moment calculated from the high field Arrott plots. The Ho^{3+} model form factor was then used to re-examine the flipping ratio data. This was found to model the data points with a low flipping ratio well. Those with a higher value (larger than 5) were poorly fitted. The reason for this is unknown and

further analysis is required.

It should be noted that a complete data set at T=2 K was taken. the analysis of this data is further complicated by the internal field of the magnetic order. This analysis can only be completed satisfactorily once the CEF splitting has been fully characterised.

Chapter 7

Conclusions

At the start of this PhD research there were several physical questions for the REPtIn series, for which no adequate answer had been found. These were listed succinctly in the opening chapter of this thesis in section 2.5.4. The analysis of neutron scattering data from samples of HoPtIn and DyPtIn allowed several conclusions to be drawn, which are discussed next.

7.1 DyPtIn

The temperature dependence of the lattice parameters was determined, along with the atomic positions. This showed that the cell expands along **a** whilst contracting along **c**. This results in a constant cell volume within the error bars. This indicates that effects such as magnetostriction are present, but probably not significant. The temperature dependant data clearly showed a two-step magnetic transition for DyPtIn. The nature of this magnetic order was determined using symmetry analysis using two independent propagation vectors. There were found to be $\boldsymbol{k}_1 = [0, 0, 0]$, and $\boldsymbol{k}_2 = [\frac{1}{2}, 0, \frac{1}{2}]$. The first magnetic phase was determined to order at $T_c = 28.1 \pm 0.3$ K, where the moments are restricted to the c-axis. The second magnetic phase orders below $T_{ab} = 18 \pm 2$ K, with the moments confined to the ab-plane. The nature of the magnetic order in this compound is different to that reported by Baran *et al.* [1]. Their magnetic structure is inconsistent with the irreducible represen-

tations of the C_{2v} of the point group.

The analysis further confirmed the general trend of a reduced magnetic moment seen in many of the REPtIn alloys. The ordered magnetic moment was found to be $\mu_{total}^{av} = 7.90 \pm 0.09 \mu_B/Dy$ at T=0 K, which is much less than the theoretical ordered moment for Dy^{3+}, $\mu_{theory} = 10 \mu_B/Dy$. Analysis of the magnitude of the magnetic moment in the c-direction clearly indicates the two-step magnetic ordering.

7.2   HoPtIn

Powder sample neutron diffraction analysis showed that HoPtIn orders with the same magnetic structure as DyPtIn at T=2 K. The diffraction pattern refinement shows the magnetic moment to be reduced. The value determine was $\mu_{Total}^{Av} = 4.04 \pm 0.08 \mu_B/Ho$, which is much less than predicted, $\mu_{Theory}^{Max} = 10 \mu_B/Ho$. A reduced magnetic moment has also been reported by Baran *et al.* [1] of $\mu_{Total}^{Baran} = 8.2 \mu_B/Ho$. The reduction found in this work is substantially more than that reported by Baran *et al.* This was attributed to the impurity phases identified in the HoPtIn powder sample, and requires further investigation with better quality samples.

Single crystal data analysis showed the magnetic moment of HoPtIn to be $\mu_{Ho} = 10.4 \pm 0.4 \mu_B$ and orientated parallel to the c-axis at T=2K. This is inconsistent with the analysis of powder-data reported here and by Baran *et al.* [1]. The reason for this is unclear, and further work on single crystal sample is desirable to ascertain the validity of this result.

The single crystal investigation also failed to find the propagation vector determined both in this work and by Baran *et al.* [1]. A search for the propagation vector $\boldsymbol{k}_2 = [\frac{1}{2}, 0, \frac{1}{2}]$ did not yield any positive results. That the single crystal analysis should be inconsistent with the powder data analysis is intriguing, and a physical explanation is yet to be determined.

Using the flipping ratio data collected a magnetisation density map was constructed using Maximum Entropy calculations. This shows that there the magnetism is highly localised to the Ho^{3+} site, and nowhere else in the cell. This is surprising as the the Ho-Pt structure of face-sharing equilateral tri-

angles and pyramids could have induced a magnetic moment on the Pt site. However, this type of induced moment was not observed in the analysis.

As the magnetisation of HoPtIn is highly localised to the Ho^{3+} site it was possible to extract the Ho^{3+} form factor from the flipping ratio data. The initial attempts to fit the full multipole expansion to the flipping ratio data were unsuccessful. This was because there were too many free parameters in the multipole model, which required 17 coefficients to be determined. As the flipping ratio data has no clear structure when plotted, it is desirable to extract the form factor from this data. For this, a new method of data reduction was developed, whereby the problem inherent to non-centrosymmetric structures is overcome. This analysis required inspection of each reflection, to determine the correct solution for the problem:

$$R(\boldsymbol{\kappa})_{measured} = \left| \frac{F_N + X\mathbb{F}_M}{F_N - X\mathbb{F}_M} \right|^2$$

for X. In this equation $X = \boldsymbol{\mu}_c f(\boldsymbol{\kappa})$ and as such inherently contains the magnitude of the magnetic moment perpendicular to the scattering vector. The plots of the Ho^{3+} form factor against $sin(\theta)/\lambda$ showed that at low angles the value of X is within the the error bar of the value determined from high field Arrott plots. This value was determined to be $\mu_c^{Arrott} = 4.40\mu_B/Ho$. That the scattering in the forward direction is equal to the moment extracted from the high field magnetic isotherms is an excellent result. It confirms that this method of data analysis is valid, and it allows the extraction of the form factor from data taken for a non-centrosymmetric crystal. It further supports the magnetisation density analysis, that most of the magnetic moment is localised on the Ho^{3+} site.

Attempts to fit the multipole expansion to the extracted form factor were also problematic. It was again found that the problem was under-determined, and that no unique solution could be found. To further the data analysis, a simplified form factor model was developed. In this model the coefficients of the radial functions seen in the multipole expansion were grouped together, so that each term had only one coefficient for each $< j_n(\boldsymbol{\kappa}) >$. This model provided an excellent fit to the form factor, as can be seen in figure 6.8. The

model form factor was then used to re-model the flipping ratio data. The fit between experimental data and model data points is in good agreement for the data points with lower R-values. However, the points with $R > 5$ seem to be poorly fitted. A high R-value means that $F_N \simeq F_M$, and that R is very sensitive to slight changes in the structure factors.

7.3 Implications for the PtREIn series

The research presented here has made a contribution to the understanding of the REPtIn series. The powder data analysis has determined the nature of the two-step magnetic ordering in DyPtIn. This indicated that the 'reduced moment' seen in this compound is related to the second magnetic phase, that is characterised by the propagation vector $\boldsymbol{k}_2 = [\frac{1}{2}, 0, \frac{1}{2}]$.

The magnetic density analysis has shown that the magnetisation is localised on the Ho^{3+} site. This research did not validate the claim by Stephens *et al.* [4] where an induced moment on the platinum $1b$ site is required.

The model developed for form factor extraction from the flipping ratio can be used for other members of the REPtIn series. This is of importance as standard data reduction software, such as CCSL, does not offer this functionality, due to the crystal structure being non-centrosymmetric. The data analysis code written as part of this thesis can be used with any of the REPtIn compounds, with only minor modifications. Other compounds, such as TmPtIn would have fewer coefficients in the multiple model, as J=6. This would reduce the fitting problem, possibly allowing a unique solution for the crystal field parameters to be determined.

7.4 Further Work

The intension of the author was to complete the anisotropic form factor determination by returning to D3. However, this was not possible given the time constraints.

As such, this analysis requires completion, whereby the anisotropic form

factor is uniquely determined. From this the CEF parameters can be obtained, and used to model the inelastic neutron scattering data.

It would also be of interest to perform a similar single crystal experiment to that completed here on several other REPtIn compounds. From this, it should be possible to explain why the magnetic ordering switches from anti-ferromagnetic to ferromagnetic across the REPtIn series.

Appendices

Appendix A

DyPtIn *.pcr File for FullProf

The control file (.pcr) for FullProf is presented below. This file was used to fit DyPtIn at $\lambda = 1.87$Å and T=2 K. There are three phases, the nuclear and the two magnetic phases. The 'C' coefficients of the basis vectors describe the magnitude of the magnetic moment. They are not necessarily in units of μ_B, as not all the basis vectors are unit vectors.

A.1   DyPtIn T=2 K, $\lambda = 1.87$Å

```
    COMM DyPtIn 2008 T=2K
! Current global Chi2 (Bragg contrib.) =       6.866
! Files => DAT-file: dyptin_2k,  PCR-file: dyptin_2k
!Job Npr Nph Nba Nex Nsc Nor Dum Iwg Ilo Ias Res Ste Nre Cry Uni Cor Opt Aut
   1   5   3   0   3   0   0   0   0   0   0   0   0   0   0   0   0   1   1
!
!Ipr Ppl Ioc Mat Pcr Ls1 Ls2 Ls3 NLI Prf Ins Rpa Sym Hkl Fou Sho Ana
   0   0   1   0   1   0   4   0   0  -3  10   1   1   0   0   1   0
!
! lambda1 Lambda2    Ratio    Bkpos    Wdt    Cthm     muR    AsyLim   Rpolarz ->Patt# 1
 1.870000 1.870000   1.0000   73.000  4.0000  0.0000 -4.9000    48.00    0.0000
!
!NCY  Eps  R_at  R_an  R_pr  R_gl     Thmin      Step      Thmax     PSD     Sent0
 20   0.01  0.50  0.50  0.50  0.50     0.8413   0.100131   153.5413   0.000   0.000
!
! Excluded regions (LowT  HighT) for Pattern#  1
        0.00         12.00
       67.75         68.20
      100.00        180.50
!
!
      23     !Number of refined parameters
!
```

```
! Zero    Code    SyCos    Code    SySin    Code  Lambda       Code MORE ->Patt# 1
  0.32857  0.0 0.00000   0.0 0.00000   0.0 0.000000    0.00   0
!   Background coefficients/codes   for Pattern#  1
  6281.7    -406.07     4522.0      8766.6     -10048.    -13370.
      41.000     51.000     61.000     71.000     21.000     31.000
!-------------------------------------------------------------------------------
! Data for PHASE number:   1  ==> Current R_Bragg for Pattern#  1:     0.00
!-------------------------------------------------------------------------------
DyPtIn_neuc
!
!Nat Dis Ang Pr1 Pr2 Pr3 Jbt Irf Isy Str Furth        ATZ    Nvk Npr More
   4   0   0 0.0 0.0 1.0   0   0   0   0   0     1417.150    0   5   0
!
P -6 2 m                  <--Space group symbol
!Atom   Typ      X        Y        Z       Biso      Occ      In Fin N_t Spc /Codes
Pt     PT      0.00000  0.00000  0.50000  1.65369  0.08333   0   0   0   0
                 0.00     0.00     0.00    151.00    0.00
Pt     PT      0.33333  0.66667  0.00000  1.40977  0.16666   0   0   0   0
                 0.00     0.00     0.00    161.00    0.00
Dy     DY      0.59410  0.00000  0.50000  1.15361  0.25000   0   0   0   0
               131.00     0.00     0.00    171.00    0.00
In     IN      0.25994  0.00000  0.00000  2.01386  0.25000   0   0   0   0
               141.00     0.00     0.00    181.00    0.00
!-------> Profile Parameters for Pattern #  1
! Scale       Shape1      Bov      Str1     Str2     Str3   Strain-Model
  180.05       0.13782   0.00000  0.00000  0.00000  0.00000      0
    11.00000    0.000     0.000    0.000    0.000    0.000
!     U         V          W         X        Y       GauSiz   LorSiz Size-Model
   2.090157  -0.566446  2.249087  0.000000  0.000000 -1.790086  0.000000   0
     81.000   111.000   121.000    0.000     0.000   201.000    0.000
!    a         b          c       alpha     beta     gamma      #Cell Info
  7.569796  7.569796  3.838067 90.000000 90.000000 120.000000
  91.00000  91.00000 101.00000   0.00000   0.00000  91.00000
! Pref1    Pref2      Asy1     Asy2     Asy3     Asy4
  0.02496  0.00000  0.18544  0.03006  0.00000  0.00000
     0.00     0.00     0.00     0.00     0.00     0.00
!-------------------------------------------------------------------------------
! Data for PHASE number:   2  ==> Current R_Bragg for Pattern#  1:     0.00
!-------------------------------------------------------------------------------
DyPtIn MAG BasIreps G3 k=000 FERRO REAL
!
!Nat Dis Mom Pr1 Pr2 Pr3 Jbt Irf Isy Str Furth        ATZ    Nvk Npr More
   1   0   0 0.0 0.0 1.0   1  -1  -2   0   0        0.000    1   1   0
!
P -1                      <--Space group symbol for hkl generation
! Nsym   Cen  Laue Ireps N_Bas
     3    1     1    -1     1
! Real(0)-Imaginary(1) indicator for Ci
   0
```

```
!
SYMM x,y,z
BASR   0   0   1
BASI   0   0   0
SYMM -y,x-y,z
BASR   0   0   1
BASI   0   0   0
SYMM -x+y,-x,z
BASR   0   0   1
BASI   0   0   0
!
!Atom   Typ  Mag Vek   X       Y       Z       Biso    Occ      C1      C2      C3
!    C4     C5     C6     C7     C8     C9     MagPh
MDY    MDY3  1  0  0.59410 0.00000 0.50000 1.15361 1.00000    7.320   0.000   0.000
                   131.00    0.00    0.00  171.00    0.00  231.00    0.00    0.00
       0.000   0.000   0.000   0.000   0.000   0.000 0.00000
       0.00    0.00    0.00    0.00    0.00    0.00    0.00
!-------> Profile Parameters for Pattern #  1
!  Scale        Shape1      Bov      Str1      Str2      Str3   Strain-Model
  180.05        0.13782  0.00000   0.00000   0.00000   0.00000      0
    11.00000     0.000    0.000     0.000     0.000     0.000
!      U        V         W          X          Y        GauSiz   LorSiz Size-Model
    2.090157 -0.566446  2.249087  0.000000  0.000000  -1.790086  0.000000    0
     81.000   111.000   121.000     0.000     0.000   201.000     0.000
!     a         b         c        alpha      beta      gamma      #Cell Info
   7.569796  7.569796  3.838067 90.000000 90.000000 120.000000
    91.00000  91.00000 101.00000   0.00000   0.00000   91.00000
!  Pref1    Pref2     Asy1     Asy2     Asy3     Asy4
  0.02496  0.00000  0.18544  0.03006  0.00000  0.00000
     0.00     0.00     0.00     0.00     0.00     0.00
! Propagation vectors:
  0.0000000   0.0000000   0.0000000          Propagation Vector  1
   0.000000    0.000000    0.000000
!-------------------------------------------------------------------------------
!  Data for PHASE number:   3  ==> Current R_Bragg for Pattern#  1:     0.00
!-------------------------------------------------------------------------------
DyPtIn MAG BasIreps G3G1 k=505 ANTI
!
!Nat Dis Mom Pr1 Pr2 Pr3 Jbt Irf Isy Str Furth        ATZ    Nvk Npr More
   2   0   0 0.0 0.0 1.0   1  -1  -2   0   0        0.000   1   1   0
!
P -1                      <--Space group symbol for hkl generation
! Nsym   Cen  Laue Ireps N_Bas
     2     1     1    -2     2
! Real(0)-Imaginary(1) indicator for Ci
  0  0
!
SYMM x,y,z
BASR   1  0  0   0  1  0
```

```
BASI  0  0  0    0  0  0
BASR  2  1  0    0  0  0
BASI  0  0  0    0  0  0
SYMM -x,-x+y,-z
BASR  1  1  0    0 -1  0
BASI  0  0  0    0  0  0
BASR  0  0  0    0  0  0
BASI  0  0  0    0  0  0
!
!Atom  Typ  Mag Vek    X       Y       Z       Biso    Occ      C1      C2      C3
!     C4     C5     C6     C7      C8      C9      MagPh
MDY2  MDY3  1  0  0.59410 0.00000 0.50000 1.15361 4.00000  -1.510  -2.695   0.000
                        131.00    0.00    0.00  171.00    0.00  211.00  191.00   0.00
        0.000   0.000   0.000   0.000   0.000   0.000   0.00000
        0.00    0.00    0.00    0.00    0.00    0.00    0.00
MDY3  MDY3  2  0  0.00000 0.59410 0.50000 1.15361 2.00000   1.527   0.000   0.000
                          0.00  131.00    0.00  171.00    0.00  221.00    0.00   0.00
        0.000   0.000   0.000   0.000   0.000   0.000   0.00000
        0.00    0.00    0.00    0.00    0.00    0.00    0.00
!-------> Profile Parameters for Pattern #  1
!  Scale        Shape1      Bov      Str1     Str2     Str3   Strain-Model
  180.05        0.13782  0.00000  0.00000  0.00000  0.00000      0
   11.00000      0.000    0.000    0.000    0.000    0.000
!     U         V          W          X         Y        GauSiz   LorSiz Size-Model
   2.090157  -0.566446   2.249087   0.000000  0.000000 -1.790086  0.000000    0
   81.000    111.000    121.000     0.000     0.000    201.000     0.000
!    a         b          c       alpha     beta      gamma      #Cell Info
   7.569796  7.569796  3.838067  90.000000 90.000000 120.000000
   91.00000  91.00000  101.00000   0.00000   0.00000   91.00000
! Pref1   Pref2     Asy1    Asy2    Asy3    Asy4
  0.02496 0.00000  0.18544 0.03006 0.00000 0.00000
     0.00   0.00     0.00    0.00    0.00    0.00
! Propagation vectors:
   0.5000000   0.0000000   0.5000000         Propagation Vector  1
   0.000000    0.000000    0.000000
!  2Th1/TOF1   2Th2/TOF2  Pattern # 1
     12.000     100.000        1
```

Appendix B

CCSL *.cry Files

B.1   D9 T=74 K .cry file

```
N HoPtIn
Y DEP
Z-----------------------------------------------------
Y UB matrix and cell from DEP checked from logs dec 2008
Y UB matrix has to be UMBL cards as directly from D9
Z-----------------------------------------------------
Z Lattice constants
Z-----------------------------------------------------
C     7.5945    7.5945    3.8216   90.0000   90.0000  120.00
Z-----------------------------------------------------
Z Instrument Parameters and UB matrix
Z-----------------------------------------------------
D WVLN  0.8386
D GEOM 6
D L/R -1
D UMBL   -0.09895  -0.15051  -0.00705
D UMBL    0.11671  -0.02736  -0.00035
D UMBL   -0.00250  -0.00409   0.26157
Z-----------------------------------------------------
Z space group
Z ----------------------------------------------------------------
Z Hexagonal P-62m. SG generated by symm.op no 2 & 7
S -y, x-y, -z
S x-y, -y, -z
Z ----------------------------------------------------------------
```

```
Z atomic positions (4th number is ITF, last number is SITE occupation)
Z -----------------------------------------------------------------
A Ho      0.59280   0.00000   0.50000   0.02452
A In      0.25982   0.00000   0.00000   0.39131
A Pt1     0.33333   0.66667   0.00000   0.28766
A Pt2     0.00000   0.00000   0.50000   0.87676
Z -----------------------------------------------------------------
Z nuclear scattering factors
Z -----------------------------------------------------------------
F Ho       1   0.80100
F In       1   0.40650
F In      -1   0   -0.00539
F Pt       1   0.96000
Z -----------------------------------------------------------------
Z crystal shape for absorption and extinction
Z -----------------------------------------------------------------
G FACE  1.0  0.0  0.0  0.6
G FACE -1.0  0.0  0.0  0.6
G FACE  0.0  1.0  0.0  0.6
G FACE  0.0 -1.0  0.0  0.6
G FACE  1.0 -1.0  0.0  0.6
G FACE -1.0  1.0  0.0  0.6
G FACE  0.0  0.0  1.0  6.0
G FACE  0.0  0.0 -1.0  6.0
G MODE 1
G PNTS 10 10 10
G MU 0.002
Z -----------------------------------------------------------------
Z extinction (DOMR in nm, MOSC in 1/rad) and absorption (in mm-1)
Z -----------------------------------------------------------------
E   1   50.0000    5.5497
Z ------------------LSQ fitting-----------------------------
I REJ 1
I DTYP 3
I OUTP 100
I NCYC 30 PRIN 3
I CONV 0.00001
L MODE 3
L REFI 1
L WGHT 2
```

```
L SCAL   8.46606
L VARY ALL ITF
L FIX DOMR
L VARY MOSC
L FIX ALL BIJ
```

B.2   D9 T=2 K .cry file

```
N HoPtIn
Y DEP working LBORO
Z----------------------------------------------------
Y UB matrix and cell from DEP checked from logs dec 2008
Y UB matrix has to be UMBL cards as directly from D9
Z----------------------------------------------------
Z Lattice constants
Z----------------------------------------------------
C    7.5945    7.5945    3.8216   90.0000   90.0000  120.00
Z----------------------------------------------------
Z Instrument Parameters and UB matrix
Z----------------------------------------------------
D WVLN  0.8386
D GEOM 6
D L/R -1
D UMBL   -0.09895  -0.15051  -0.00705
D UMBL    0.11671  -0.02736  -0.00035
D UMBL   -0.00250  -0.00409   0.26157
Z-------------------------------------------------------
Z space group-------------------------------------------
Z -----------------------------------------------------------
Z Hexagonal P-62m. SG generated by symm.op no 2 & 7
S -y, x-y, -z
S x-y, -y, -z
Z -----------------------------------------------------------
Z atomic positions (4th number is ITF, last number is SITE occupation)
Z -----------------------------------------------------------
A Ho     0.59303   0.00000   0.50000  -0.08146
A HoD    0.59303   0.00000   0.50000  -0.08146
A In     0.26077   0.00000   0.00000   0.41242
A Pt1    0.33333   0.66667   0.00000   0.14643
```

```
A Pt2     0.00000    0.00000    0.50000    0.69158
Z --------------------------------------------------------------
Z nuclear scattering factors
Z --------------------------------------------------------------
F Ho      1   0.80100
F HoD     1   0.00000
F In      1   0.40650
F In     -1   0   -0.00539
F Pt      1   0.96000
F Hoj0 2 0.0566 18.3176 0.3365 7.6880 0.6317 2.9427 -0.0248
F Hoj2 4 0.2188 18.5157 1.0240 6.7070 0.9251 2.1614 0.0268
Z --------------------------------------------------------------
Z Q card for Magnetic info.  HoM is form factor for Ho
Z --------------------------------------------------------------
Q Hoj0 FORM Ho
Q Hoj2 FORM HoD
Q STYP ANTI
Q PROP    0.0000    0.0000    0.0000
Q Ho MU     7.8931
Q HoD MU     2.5045
Z Atom label, THET, PHI, angle of MU to CCSL axis--
Q Ho SDIR   -1.8139  -30.0000
Q HoD SDIR    -1.8139  -30.0000
Z--- Magnetic Symmetry Descibed on MSYM and NSYM Cards-------
Q MSYM 3 1 12 -1
Q NSYM  4 1 0 0 0 1 0 0 0 1
Z --------------------------------------------------------------
Z crystal shape for absorption and extinction
Z --------------------------------------------------------------
G FACE  1.0  0.0  0.0  0.6
G FACE -1.0  0.0  0.0  0.6
G FACE  0.0  1.0  0.0  0.6
G FACE  0.0 -1.0  0.0  0.6
G FACE  1.0 -1.0  0.0  0.6
G FACE -1.0  1.0  0.0  0.6
G FACE  0.0  0.0  1.0  6.0
G FACE  0.0  0.0 -1.0  6.0
G MODE 1
G PNTS 10 10 10
G MU 0.002
```

```
Z ----------------------------------------------------------------
Z extinction (DOMR in nm, MOSC in 1/rad) and absorption (in mm-1)
Z ----------------------------------------------------------------
E   1   50.0000    2.5691
Z ------------------LSQ fitting  Setup------------------
I DTYP 3
ZI OUTP 100
I NCYC 10  PRIN 3
I CONV 0.0001
L MODE 3
L REFI 2
L WGHT 2
Z ------------------LSQ fitting  refine------------------
L SCAL   8.18001
L VARY ALL ITF
L FIX DOMR
L VARY MOSC
L VARY Ho MU
L VARY HoD MU
L VARY Ho THET
L VARY Ho THET
L RELA 1 1 Ho ITF 1 HoD ITF
L RELA 1 1 Ho THET 1 HoD THET
X SYMB Ho  0.701  0.598  0.996  0.199  1.000  0.135  0.170
X SYMB In  0.669  0.199  0.598  0.398
X SYMB Pt1  0.581  0.996  0.398  0.598
```

Appendix C

Form Factor Analysis Code

The Maple code written to least-squares-fit the anisotropic form factor is included below.

C.1 Coding Information and Notation

The flipping ratio, R, is defined as:

$$R(\boldsymbol{\kappa}) = \frac{I_+}{I_-} = \left(\frac{|F_N + F_M|}{|F_N - F_M|} \right)^2 \tag{C.1.1}$$

where $F_N(\boldsymbol{\kappa})$ and $F_M(\boldsymbol{\kappa})$ have been **coded** as:

$$
\begin{aligned}
F_N(\boldsymbol{\kappa}) &= \sum_{atoms} b_a e^{i\boldsymbol{\kappa}\cdot\boldsymbol{r_a}} \\
&= \sum_{Ho} b_{Ho} e^{i\boldsymbol{\kappa}\cdot\boldsymbol{r_{Ho}}} + \sum_{Pt} b_{Pt} e^{i\boldsymbol{\kappa}\cdot\boldsymbol{r_{Pt}}} + \sum_{In} b_{In} e^{i\boldsymbol{\kappa}\cdot\boldsymbol{r_{In}}} \\
&= b_{Ho} \left(e^{2\pi i(h\cdot x_{Ho_1}+k\cdot y_{Ho_1})} + e^{2\pi i(h\cdot x_{Ho_2}+k\cdot y_{Ho_2})} + e^{2\pi i(h\cdot x_{Ho_3}+k\cdot y_{Ho_3})} \right) \\
&+ b_{Pt} \left(e^{2\pi i(h\cdot x_{Pt_1}+k\cdot y_{Pt_1})} + e^{2\pi i(h\cdot x_{Pt_2}+k\cdot y_{Pt_2})} + e^{2\pi i(h\cdot x_{Pt_3}+k\cdot y_{Pt_3})} \right) \\
&+ b_{In} \left(e^{2\pi i(h\cdot x_{In_1}+k\cdot y_{In_1})} + e^{2\pi i(h\cdot x_{In_2}+k\cdot y_{In_2})} + e^{2\pi i(h\cdot x_{In_3}+k\cdot y_{In_3})} \right)
\end{aligned}
\tag{C.1.2}
$$

$F_M(\boldsymbol{\kappa})$, the magnetic structure factor is **coded** as:

$$
\begin{aligned}
F_M(\boldsymbol{\kappa}) &= \sum_{Magnetic\ atoms} f(\boldsymbol{\kappa})e^{i\boldsymbol{\kappa}\cdot\boldsymbol{r_a}} \\
&= \sum_{Ho} f(\boldsymbol{\kappa})e^{i\boldsymbol{\kappa}\cdot\boldsymbol{r_{Ho}}} \\
&= f(\boldsymbol{\kappa})\left(e^{2\pi i(h\cdot x_{Ho_1}+k\cdot y_{Ho_1})} + e^{2\pi i(h\cdot x_{Ho_2}+k\cdot y_{Ho_2})} + e^{2\pi i(h\cdot x_{Ho_3}+k\cdot y_{Ho_3})}\right)
\end{aligned}
$$

where $f(\boldsymbol{\kappa})$ is the Ho^{3+} form factor. This requires calculating the transition matrix between all states of the Ho^{3+} ion, λ, described by $2J+1$ total angular momentum levels, M_J. As $J = 8$, there are 17 M_J values, $M_J = -8, ..., 0, ...+8$.

$$
|\lambda > = \sum_M a_M |JM > \tag{C.1.3}
$$

which gives:

$$
\begin{aligned}
f(\boldsymbol{\kappa}) &= \sum_M \sum_{M'} < JM | a_M^* \hat{\mathbf{Q}}_\perp a_M | J'M' > \tag{C.1.4} \\
&= \sum_M \sum_{M'} a_M^* a_M < JM | \hat{\mathbf{Q}}_\perp | J'M' > \tag{C.1.5}
\end{aligned}
$$

where

$$
\begin{aligned}
< JM | \hat{\mathbf{Q}}_\perp | J'M' > &= (4\pi)^{\frac{1}{2}} \sum_{K''Q''} Y_{Q''}^{K''}(\hat{\kappa}) \sum_{K'Q'} [A(K''K') + B(K''K')] \\
&\times (K'Q'JM'|JM)(K''Q''K'Q'|1q)
\end{aligned}
$$

or in the MAPLE notation used, a prime symbol was written as the letter p, and remembering that $J = 8$ and $q = 0$;

$$
\begin{aligned}
\hat{F}(\bar{\kappa}) &= \sum_{Kpp} \sum_{Qpp} Y_{Qpp}^{Kpp}(\hat{\kappa}) \sum_{Kp} \sum_{Qp} \sum_M \sum_{Mp} a_M a_{Mp}^* [A(Kpp\ Kp) + B(Kpp\ Kp)] \\
&\times\ <\ Kp\ Qp\ 8\ Mp\ |\ J\ 8\ >\ <\ Kpp\ Qpp\ Kp\ Qp\ |\ 1\ 0\ > \tag{C.1.6}
\end{aligned}
$$

where the two final terms in pointed brackets are Clebsch Gorden coefficients given by

$$< Kp\ Qp\ 8\ Mp\ |\ 8\ M > \ =\ (-1)^{Kp-8-M}\sqrt{(2\times 8)+1}\begin{pmatrix} Kp & 8 & 8 \\ Q & Mp & M \end{pmatrix}$$

$$< Kpp\ Qpp\ Kp\ Qp\ |\ 1\ 0 > \ =\ (-1)^{Kpp-Kp}\sqrt{1}\begin{pmatrix} Kpp & Kp & 1 \\ Qpp & Qp & 0 \end{pmatrix}$$

$$(C.1.7)$$

C.2 Maple Code

The maple code written to extract the Ho^{3+} form factor from the flipping ratio data is now included. This also includes the programming of the multipole expansion to be used for fitting to the form factor or flipping ratio.

```
> #****************************************************************************#
  # Maple Code to caculate the Flipping ratio measured on D3 using full magnetic
  # form factor for the Ho3+ Ion.
  # Written By DEP and KUN  2009/2010.
  # The parameters below were refined using CCSL on D9 data taken by DEP .
  # bPt,bIn,bHo =  the scattering cross-sections
  # MoM       = refined moment using the dipole approximation from D9
  # λ         = D3 Wavelength.
  #****************************************************************************#
> restart :
  Digits := 40 :
  with( plots ) :
  with( Statistics ) :
  with( ExcelTools ) :
  with( LinearAlgebra ) :
  with( ArrayTools ) :
> bPt := 0.96E−12 :              # nuclear scattering lengths

  bIn := 0.4065E-12 :            # units=10⁻¹²cm
  bHo := 0.801E-12 :
  Mom := 7.8919 + 2.4035 :        #  magnetic moment on Ho in μ_B

  λ := 0.8386 :                   # Wavelength
  a := 7.5945 :                   # Refined cell parameters
  c := 3.8216 :
```

$$astar := \frac{2 \cdot \pi}{a} \; \frac{1}{\cos\left(\frac{30}{180} \cdot \pi\right)} \; :$$

$$cstar := \frac{2 \cdot \pi}{c} \; :$$

```
  S := 2 :                        # Spin (Hunds rules)
  L := 6 :                        # Ang Mo (Hunds Rules)
  J := S + L :
```

$$gs := 1 + \frac{(S \cdot (S + 1) - L \cdot (L + 1))}{J \cdot (J + 1)} \; :$$

$$gl := \frac{1}{2} + \frac{(L \cdot (L + 1) - S \cdot (S + 1))}{2J \cdot (J + 1)} \; :$$

```
  g := gl + gs :                  # Lande g−factor
  ro := -0.54E−12 :                #  magneitc scattering length


> #****************************************************************************#
  #  Now input key coefficents taken from the Crystallographic Tables V.C
  #  cojn = a 4 by 7 array, containing aAbBcCd, the coefficents required for the Bessel j'th
  #        Bessel function fitted to the form factor.
  # A1coef  = a storage array for the coeffcients required in the orbital contribution to
  #           scattering A(K'',K'), of which there are three.  A'(0,1) A'(2,3) A'(4,5)
  # C1coef  = a storage array for the coeffcients required in the spin contribution to
  #           scattering, B(K'',K') of which there are seven.  C'(0,1) C'(2,1) C'(2,3) etc
  #****************************************************************************#
> cojn := Matrix(4, 7, [0.0566, 18.3176, 0.3365, 7.688, 0.6317, 2.9427, -0.0248, 0.2188, 18.5157, 1.024, 6.707,
        0.9251, 2.1614, 0.0268, -0.2717, 9.7313, 0.0474, 4.6378, 0.2292, 1.0473, 0.0124, -0.0289, 6.0504,
        -0.1545, 2.2305, 0.1550, 1.2605, 0.0177]) :
  A1coef := Vector_row(3, [ -2.1213, 0.3596, -0.1713]) :

  C1coef := Vector_row(7, [ -2.1213, 0.1000, -0.1648, 0.1297, -0.2496, 0.3505, -0.8481]) :

> #****************************************************************************#
> # Input the atomic positions from the D9 refinement.
> #****************************************************************************#

> posPt := [ [ \frac{1}{3}, \frac{2}{3}, 0 ], [ \frac{2}{3}, \frac{1}{3}, 0 ], [ 0, 0, \frac{1}{2} ] ] :
```

```
  xposPt := 0.59303 :
  posHo := [[xposPt, 0, 1/2], [0, xposPt, 1/2], [1 − xposPt, 1 − xposPt, 1/2]] :
  xposIn := 0.26077 :
  posIn := [[xposIn, 0, 0], [0, xposIn, 0], [1 − xposIn, 1 − xposIn, 0]] :
  # print(posPt, posHo, posIn) :
> #********************************************************************#
> #  A Procedure to calculate s = sin(θ)/λ from hkl Miller indicies
> #  INPUT= (h,k)
> #  OUTPUT =  s = sin(θ)/λ
> #********************************************************************#
```

```
>  slam := proc(h, k) #  return   sin(ϑ)/λ

      local s :

      s := 1/a · sqrt( (h^2 + k^2 + h·k)/3 ) ;
       return evalf(s);
      end proc:
```

```
>  normam := proc(am, n);        # recieves a vector of non−normalised values and normalises them to sum(am)^2
              = 1
      local nc, i, amn;
      nc := 0;
      amn := Vector(n, 0);
          for i from 1 to n do
          nc := nc + am[i]^2;               # work out normalisation constant
          end do;
          for i from 1 to n do

          amn[i] := sqrt( am[i]^2 / nc ) ;        #apply  normalisation

          end do;
        return amn;
      end proc:
```

```
> #********************************************************************#
> #  A Procedure to calculate any jn (n = 0, 2 4, 6) form factor bessel function.
> #  INPUT= (s,jn). s = sin(θ)/λ for a given hkl reflection. This can be calculated in the proc
> #          slam. jn = code number corresponding to the order (n) of jn required.
> #          NOTE only the first jn, namely j0 is not multiplied by s^2.
> #          NOTE as n = (0,2,4,6) the array row for j0=1, j2=2, j4=3, j6=4
   # OUTPUT = the jn'th component of the form factor for a given hkl.
   #********************************************************************#
```

```
>  jn := proc(s, jn)
      local jncalc, jrow, ss :

      jrow := jn/2 + 1;            # convert n to array row index

      ss := s·s :
      jncalc := cojn[jrow, 1]·exp(−cojn[jrow, 2]· ss) + cojn[jrow, 3]·exp(−cojn[jrow, 4]· ss) + cojn[jrow,
        5]·exp(−cojn[jrow, 6]· ss) + cojn[jrow, 7] :
        if jn ≠ 0 then
          jncalc := jncalc·ss :
        end if:
      return  jncalc :
      end proc:
> plot([ jn(s, 0), jn(s, 2), jn(s, 4), jn(s, 6) ], s = 0 ..1.5, title = "j'ns");
```

j'ns
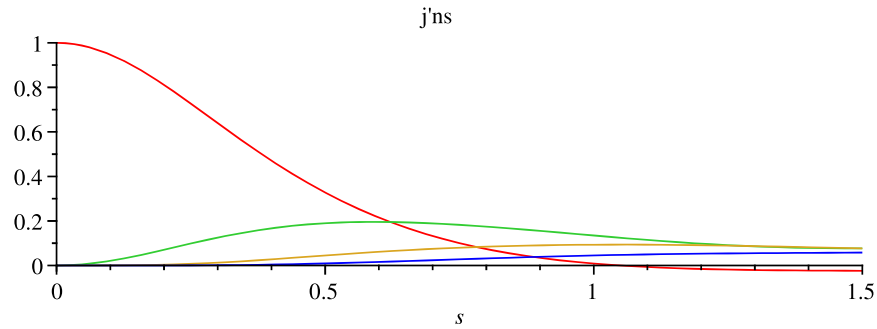
```
> #****************************************************************************#
> # Define atwo arrays fo A(K'',K') and B(K'',K') functions dependant on coefficents
> # stored in A1coef and  C1coef, and the jn'th Bessel function.
> #****************************************************************************#
```

$$> \quad A := \textbf{proc}(Kpp, Kp, s)$$

$$\textbf{local } indx, c :$$

$$\textbf{if } |Kpp - Kp| \neq 1 \textbf{ then return } 0; \textbf{ end if}:$$

$$\textbf{if } \quad Kp = 7 \textbf{ then return } 0; \textbf{ end if}:$$

$$indx := \frac{Kp + 1}{2};$$

$$c := A1coef[indx] \cdot (jn(s, Kp - 1) + jn(s, Kp + 1)) :$$

$$\textbf{if } Kpp > Kp \ \textbf{ then return } \text{sqrt}\left(\frac{Kp}{Kp + 1} \right) \cdot c;$$

$$\textbf{else return } c; \ \textbf{end if}:$$

$$\textbf{end proc}:$$

$$> \quad B := \textbf{proc}(Kpp, Kp, s)$$

$$\textbf{local } index :$$

$$\textbf{if } |Kpp - Kp| \neq 1 \textbf{ then return } 0; \textbf{ end if}:$$

$$\textbf{if } Kpp > Kp \textbf{ then } \ index := Kpp;$$

$$\textbf{else } index := Kp \textbf{ end if}:$$

$$\textbf{if } Kp = 1 \textbf{ and } Kpp = 0 \textbf{ then return } C1coef[1] \cdot \frac{2}{3} \ \cdot jn(s, 0) - C1coef[2] \cdot \frac{\text{sqrt}(2)}{3} \ \cdot jn(s, 2); \textbf{ end if}:$$

$$\textbf{if } Kp = 1 \textbf{ and } Kpp = 2 \textbf{ then return } C1coef[1] \cdot \frac{\text{sqrt}(2)}{3} \ \cdot jn(s, 0) - C1coef[2] \cdot \frac{1}{3} \ \cdot jn(s, 2); \textbf{ end if}:$$

$$\textbf{if } Kp = 3 \textbf{ and } Kpp = 2 \textbf{ then return } - C1coef[3] \cdot \frac{4}{\text{sqrt}(21)} \ \cdot jn(s, 2) + C1coef[4] \cdot \frac{2}{\text{sqrt}(7)} \ \cdot jn(s, 4); \textbf{ end if}:$$

$$\textbf{if } Kp = 3 \textbf{ and } Kpp = 4 \textbf{ then return } - C1coef[3] \cdot \frac{\text{sqrt}(4)}{\text{sqrt}(7)} \ \cdot jn(s, 2) + C1coef[4] \cdot \frac{\text{sqrt}(3)}{\text{sqrt}(7)} \ \cdot jn(s, 4); \textbf{ end if}:$$

$$\textbf{if } Kp = 5 \textbf{ and } Kpp = 4 \textbf{ then return } C1coef[5] \cdot \frac{6}{\text{sqrt}(33)} \ \cdot jn(s, 4) - C1coef[6] \cdot \frac{\text{sqrt}(10)}{\text{sqrt}(11)} \ \cdot jn(s, 6); \textbf{ end if}:$$

$$\textbf{if } Kp = 5 \textbf{ and } Kpp = 6 \textbf{ then return } C1coef[5] \cdot \frac{\text{sqrt}(30)}{\text{sqrt}(33)} \ \cdot jn(s, 4) - C1coef[6] \cdot \frac{\text{sqrt}(25)}{\text{sqrt}(33)} \ \cdot jn(s, 6); \textbf{ end if}:$$

$$\textbf{if } Kp = 7 \textbf{ and } Kpp = 6 \textbf{ then return } - C1coef[7] \cdot \frac{7}{\text{sqrt}(39)} \ \cdot jn(s, 6); \textbf{ end if}:$$

$$\textbf{if } Kp = 7 \textbf{ and } Kpp = 8 \textbf{ then return } - \text{sqrt}\left(\frac{7}{8} \right) \cdot C1coef[7] \cdot \frac{7}{\text{sqrt}(39)} \ \cdot jn(s, 6); \textbf{ end if}:$$

$$\textbf{end proc}:$$

```
> #****************************************************************************#
> # The spherical harmonics are coded
> #****************************************************************************#
```

> $Y := \mathbf{proc}(l, m, \theta, \Phi)$
> $\mathbf{local}\, f:$
>
> $f := \dfrac{1}{\sqrt{4 \cdot \pi}}\;:$
>
> **if** $l = 0$ **then return** f; **end if**:
>
> **if** $l = 1$ **then**
>   **if** $m = 0$ **then return** $f \cdot \sqrt{3} \cdot \cos(\theta)$; **end if**:
>   **if** $|m| = 1$ **then return** $-m \cdot f \cdot \sqrt{\dfrac{3}{2}} \cdot \sin(\theta) \cdot \exp(m \cdot I \cdot \Phi)$; **end if**:
> **end if**:
>
> **if** $l = 2$ **then**
>   **if** $m = 0$ **then return** $\dfrac{f \cdot \sqrt{5}}{2} \cdot \left(3 \cdot \left(\cos(\theta)\right)^2 - 1\right)$; **end if**:
>   **if** $|m| = 1$ **then return** $-m \cdot f \cdot \sqrt{\dfrac{15}{2}} \cdot \sin(\theta) \cdot \cos(\theta) \cdot \exp(m \cdot I \cdot \Phi)$; **end if**:
>   **if** $|m| = 2$ **then return** $f \cdot \sqrt{\dfrac{15}{8}} \cdot \left(\sin(\theta)\right)^2 \cdot \exp(m \cdot I \cdot \Phi)$; **end if**:
> **end if**:
>
> **if** $l = 3$ **then**
>   **if** $m = 0$ **then return** $\dfrac{f \cdot \sqrt{7}}{2} \cdot \left(5 \cdot \left(\cos(\theta)\right)^3 - 3 \cdot \cos(\theta)\right)$; **end if**:
>   **if** $|m| = 1$ **then return** $-\dfrac{m \cdot f \cdot \sqrt{21}}{4} \cdot \sin(\theta) \cdot \left(5 \cdot \left(\cos(\theta)\right)^2 - 1\right) \cdot \exp(m \cdot I \cdot \Phi)$; **end if**:
>   **if** $|m| = 2$ **then return** $\dfrac{f \cdot \sqrt{210}}{4} \cdot \left(\sin(\theta)\right)^2 \cdot \cos(\theta) \cdot \exp(m \cdot I \cdot \Phi)$; **end if**:
>   **if** $|m| = 3$ **then return** $\dfrac{-m \cdot f \cdot \sqrt{35}}{4 \cdot |m|} \cdot \left(\sin(\theta)\right)^3 \cdot \exp(m \cdot I \cdot \Phi)$; **end if**:
> **end if**:
>
> **if** $l = 4$ **then**
>   **if** $m = 0$ **then return** $\dfrac{f \cdot 3}{8} \cdot \left(35 \cdot \left(\cos(\theta)\right)^4 - 30 \cdot \left(\cos(\theta)\right)^2 + 3\right)$; **end if**:
>   **if** $|m| = 1$ **then return** $-\dfrac{m \cdot f \cdot 3 \cdot \sqrt{5}}{4} \cdot \sin(\theta) \cdot \left(7 \cdot \left(\cos(\theta)\right)^3 - 3 \cdot \cos(\theta)\right) \cdot \exp(m \cdot I \cdot \Phi)$; **end if**:
>   **if** $|m| = 2$ **then return** $\dfrac{f \cdot 3 \cdot \sqrt{10}}{8} \cdot \left(\sin(\theta)\right)^2 \cdot \left(7 \cdot \left(\cos(\theta)\right)^2 - 1\right) \cdot \exp(m \cdot I \cdot \Phi)$; **end if**:
>   **if** $\left|m\right| = 3$ **then return** $\dfrac{-m \cdot f \cdot 3 \cdot \sqrt{35}}{4 \cdot |m|} \cdot \left(\sin(\theta)\right)^3 \cdot \cos(\theta) \cdot \exp(m \cdot I \cdot \Phi)$; **end if**:
>   **if** $|m| = 4$ **then return** $\dfrac{f \cdot 3 \cdot \sqrt{70}}{16} \cdot \left(\sin(\theta)\right)^4 \cdot \exp(m \cdot I \cdot \Phi)$; **end if**:
> **end if**:
>
> **if** $l = 6$ **then return** $f \cdot Y6(m, \theta, \Phi)$; **end if**:
>
> **if** $l = 8$ **then return** $f \cdot Y8(m, \theta, \Phi)$; **end if**:
>
> $print(\text{" error in Y(l,m) calculation for l=", } l, \text{ "   m=", } m)$;
> **return** 0;
>
> **end proc**:

```
> Y6 := proc(m, θ, Φ)
```

$\quad$ **if** $m = 0$ **then return** $\frac{\sqrt{13}}{16} \cdot \left(231 \cdot \left(\cos(\theta)\right)^6 - 315 \cdot \left(\cos(\theta)\right)^4 + 105 \cdot \left(\cos(\theta)\right)^2 - 5\right)$; **end if**:

$\quad$ **if** $|m| = 1$ **then return** $-\frac{m \cdot \sqrt{546}}{16} \cdot \sin(\theta) \cdot \left(33 \cdot \left(\cos(\theta)\right)^5 - 30 \cdot \left(\cos(\theta)\right)^3 + 5 \cdot \cos(\theta)\right) \cdot \exp(m \cdot I \cdot \Phi)$;
$\qquad$ **end if**:

$\quad$ **if** $|m| = 2$ **then return** $\frac{\sqrt{1365}}{32} \cdot \left(\sin(\theta)\right)^2 \cdot \left(33 \cdot \left(\cos(\theta)\right)^4 - 18 \cdot \left(\cos(\theta)\right)^2 + 1\right) \cdot \exp(m \cdot I \cdot \Phi)$; **end if**:

$\quad$ **if** $\left|m\right| = 3$ **then return** $\frac{-m \cdot \sqrt{1365}}{16 \cdot |m|} \cdot \left(\sin(\theta)\right)^3 \cdot \left(11 \cdot \left(\cos(\theta)\right)^3 - 3 \cdot \cos(\theta)\right) \cdot \exp(m \cdot I \cdot \Phi)$; **end if**:

$\quad$ **if** $|m| = 4$ **then return** $\frac{3 \cdot \sqrt{182}}{32} \cdot \left(\sin(\theta)\right)^4 \cdot \left(11 \cdot \left(\cos(\theta)\right)^2 - 1\right) \cdot \exp(m \cdot I \cdot \Phi)$; **end if**:

$\quad$ **if** $\left|m\right| = 5$ **then return** $\frac{-m \cdot 3 \cdot \sqrt{1001}}{16 \cdot |m|} \cdot \left(\sin(\theta)\right)^5 \cdot \cos(\theta) \cdot \exp(m \cdot I \cdot \Phi)$; **end if**:

$\quad$ **if** $|m| = 6$ **then return** $\frac{\sqrt{3003}}{32} \cdot \left(\sin(\theta)\right)^6 \cdot \exp(m \cdot I \cdot \Phi)$; **end if**:

$\quad$ **end proc**:

```
Y8 := proc(m, θ, Φ)
```

$\quad$ **if** $m = 0$ **then return** $\frac{\sqrt{17}}{128} \cdot \left(6435 \cdot \left(\cos(\theta)\right)^8 - 12012 \cdot \left(\cos(\theta)\right)^6 + 6930 \cdot \left(\cos(\theta)\right)^4 - 1260 \right.$
$\qquad \left. \cdot \left(\cos(\theta)\right)^2 + 35\right)$; **end if**:

$\quad$ **if** $|m| = 1$ **then return** $-\frac{m \cdot 3 \cdot \sqrt{34}}{64} \cdot \sin(\theta) \cdot \left(715 \cdot \left(\cos(\theta)\right)^7 - 1001 \cdot \left(\cos(\theta)\right)^5 + 385 \cdot \left(\cos(\theta)\right)^3 - 35\right.$
$\qquad \left. \cdot \cos(\theta)\right) \cdot \exp(m \cdot I \cdot \Phi)$; **end if**:

$\quad$ **if** $|m| = 2$ **then return** $\frac{3 \cdot \sqrt{595}}{64} \cdot \left(\sin(\theta)\right)^2 \cdot \left(143 \cdot \left(\cos(\theta)\right)^6 - 143 \cdot \left(\cos(\theta)\right)^4 + 33 \cdot \left(\cos(\theta)\right)^2 - 1\right)$
$\qquad \cdot \exp(m \cdot I \cdot \Phi)$; **end if**:

$\quad$ **if** $\left|m\right| = 3$ **then return** $\frac{-m \cdot \sqrt{39270}}{64 \cdot |m|} \cdot \left(\sin(\theta)\right)^3 \cdot \left(39 \cdot \left(\cos(\theta)\right)^5 - 26 \cdot \left(\cos(\theta)\right)^3 + 3 \cdot \cos(\theta)\right) \cdot \exp(m$
$\qquad \cdot I \cdot \Phi)$; **end if**:

$\quad$ **if** $|m| = 4$ **then return** $\frac{3 \cdot \sqrt{2618}}{128} \cdot \left(\sin(\theta)\right)^4 \cdot \left(65 \cdot \left(\cos(\theta)\right)^4 - 26 \cdot \left(\cos(\theta)\right)^2 + 1\right) \cdot \exp(m \cdot I \cdot \Phi)$; **end**
$\qquad$ **if**:

$\quad$ **if** $|m| = 5$ **then return** $\frac{-m \cdot 3 \cdot \sqrt{34034}}{64 \cdot |m|} \cdot \left(\sin(\theta)\right)^5 \cdot \left(5 \cdot \left(\cos(\theta)\right)^3 - \cos(\theta)\right) \cdot \exp(m \cdot I \cdot \Phi)$; **end if**:

$\quad$ **if** $\left|m\right| = 6$ **then return** $\frac{\sqrt{7293}}{64} \cdot \left(\sin(\theta)\right)^6 \cdot \left(15 \cdot \left(\cos(\theta)\right)^2 - 1\right) \cdot \exp(m \cdot I \cdot \Phi)$; **end if**:

$\quad$ **if** $\left|m\right| = 7$ **then return** $\frac{-m \cdot 3 \cdot \sqrt{24310}}{64 \cdot |m|} \cdot \left(\sin(\theta)\right)^7 \cdot \cos(\theta) \cdot \exp(m \cdot I \cdot \Phi)$; **end if**:

$\quad$ **if** $|m| = 8$ **then return** $\frac{3 \cdot \sqrt{24310}}{256} \cdot \left(\sin(\theta)\right)^8 \cdot \exp(m \cdot I \cdot \Phi)$; **end if**:

$\quad$ **end proc**:

```
> #***************************************************************************#
  # getphi is a procedure that returns the angle between the scattering vector (G) and a* on the
> # reciprocal lattice. The reciprocal lattice has  60 degrees between a* and b*.
> #***************************************************************************#
> getphi := proc(h, k);                                    #angle from reciprocal lattice vector to a-star
    local as, bs, c, cabs, Φ :
    if (h = 0) and (k = 0) then return 0; end if;
    as := [1, 0] :
```

```
    #  bs := [cos(π/3), sin(π/6)] : now evaluated
   bs := [0.5, 0.5·sqrt(3)] :
   c := h·as + k·bs :
   cabs := sqrt(c[1]·c[1] + c[2]·c[2]) :
   Φ := arccos(c[1]/cabs);
   if k < 0 then return (2·π − Φ); end if;
   return Φ;
  end proc:
```

> #*some tests*

$$\#\ `print\left(evalf\left(getphi(1, 0) \cdot \frac{180}{\pi}\right), 0\right);$$

$$\#print\left(evalf\left(getphi(1, 1) \cdot \frac{180}{\pi}\right), 30\right);$$

$$\#print\left(evalf\left(getphi(0, 1) \cdot \frac{180}{\pi}\right), 60\right);$$

$$\#print\left(evalf\left(getphi(-1, 1) \cdot \frac{180}{\pi}\right), 120\right);$$

$$\#print\left(evalf\left(getphi(-1, 0) \cdot \frac{180}{\pi}\right), 180\right);$$

$$\#print\left(evalf\left(getphi(-1, -1) \cdot \frac{180}{\pi}\right), 210\right);$$

$$\#print\left(evalf\left(getphi(0, -1) \cdot \frac{180}{\pi}\right), 240\right);$$

$$\#print\left(evalf\left(getphi(1, -1) \cdot \frac{180}{\pi}\right), 300\right);$$

> #**#
  #CG is a procedure to calculate the Clebsch–Gordan coupling coefficient for the angular
  #momentum states accepted as arguments.
> #**#

> $CG := \mathbf{proc}(j1, m1, j2, m2, j3, m3)$
    #*Note the order in which arguments are passed*
  local κ, κmin, κmax, c1, c2, c3, c4;
    κmin := max(0, -(j3 − j2 + m1), -(j3 − j1 − m2));
    κmax := min(j1 + j2 − j3, j1 − m1, j2 + m2);
  if $m1 + m2 \neq m3$ **then return** 0; **end if**:
  if (j1 + j2 < j3) **then return** 0; **end if**:   # *checks to avoid negative factorials in c1*
  if (j2 + j3 < j1) **then return** 0; **end if**:   # *checks to avoid negative factorials in c1*
  if ($j3$ + j1 < j2) **then return** 0; **end if**:   # *checks to avoid negative factorialsin c1*

$$c1 := (-1)^{j1 - j2 - m3} \cdot sqrt\left(\frac{(j1 + j2 - j3)!\cdot(j2 + j3 - j1)!\cdot(j3 + j1 - j2)!}{(j1 + j2 + j3 + 1)!}\right) :$$

  c2 := 0 :
  for κ **from** κmin **to** κmax **do**

$$c2 := c2 + (-1)^{\kappa} \cdot \frac{sqrt((j1 + m1)!\cdot(j1 - m1)!\cdot(j2 + m2)!)}{\kappa!\cdot(j1 + j2 - j3 - \kappa)!\cdot(j1 - m1 - \kappa)!\cdot(j2 + m2 - \kappa)!}$$
$$\cdot \frac{sqrt((j2 - m2)!\cdot(j3 + m3)!\cdot(j3 - m3)!)}{(j3 - j2 + m1 + \kappa)!\cdot(j3 - j1 - m2 + \kappa)!};$$

  end do:
  return $\left((-1)^{(j2 - j1 + m3)} \cdot \sqrt{(2 \cdot j3 + 1)} \cdot c1 \cdot c2\right);$
  end proc:

> #**#

```maple
#A vector to store the am coefficients, which are to be refined is initialised and normalised.
# 'nam' is the Number of AM coefficients and can be passed to the 'normam' proc
#*****************************************************************************#
> nam := 17 :
  am := normam( Vector([0.8, 0, 2, 0, 1, 0, 2, 0, 2, 0, 0, 0, 0, 0, 0, 0, 0]), nam) : #chisq=6
   evalf(am);
```

$$\begin{bmatrix} 1 .. 17 \; Vector_{column} \\ Data \; Type: \; anything \\ Storage: \; rectangular \\ Order: \; Fortran\_order \end{bmatrix}$$

(1)

```maple
> #*****************************************************************************#
  # The Matrix elements between given J states is evaluated. This is the main procedure.
  # In keeping with standard notation 'p' stands for primed , as such Kpp is K'' etc.
  # Φ and θ are angles describing the orientation of the scattering vector.
  #*****************************************************************************#
> MatEl := proc(h, k, M, Mp)
  local Kp, Kpp, Qp, Qpp, sumMp , CGcoef, θ, Φ, s, Sph, AB, Spc;
   global ro;
```

$$\theta := \frac{\pi}{2};$$ # it is the basal plane

```maple
  s := slam(h, k) :
  Φ := getphi(h, k) :
  # print(  "  Φ in MatEl ", evalf(Φ));
  sumMp := 0 :
     for Kpp from 0 to 8 by 2 do          # to 2  = the dipole approx 8 for full
       for Qpp from -Kpp to Kpp do
       Sph := Y(Kpp, Qpp, θ, Φ) :
         for Kp  from |Kpp − 1| to  min(7, Kpp + 1) by 2 do   # min(1  = the dipole approx, 7 for full
           for Qp from -Kp to  Kp do
             if  (Kpp + Kp ≥ 1) and (Kp + 1 ≥ Kpp) and (1 + Kpp ≥ Kp) then
               if Qp + Mp = M  and Qpp + Qp = 0 then
                 AB := A(Kpp, Kp, s) + B(Kpp, Kp, s) :
                 CGcoef := CG(Kp, Qp, 8, Mp, 8, M)·CG(Kpp, Qpp, Kp, Qp, 1, 0) :
                  sumMp := sumMp + evalf(AB·CGcoef· Sph) :
               end if:
             end if:
           end do:              #loop in Qp
         end do:                #loop in Kp
       end do;              #loop in Qpp
     end do;            #loop in Kpp
```

$$return \; evalf\left(-2·\sqrt{4·\pi} · (sumMp) \right);$$ #note a factor of 2 will give magnetiude in μB

```maple
  end proc:
> # some tests
  #MatEl(1, 0, 8, 8);
  #MatEl( 0, 1, 8, 8);
  #MatEl(1, 1, 8, 8);
> #*****************************************************************************#
  # The form factor procedure Matl() is checked by plotting the angular dependence of
  # the magnetic intensity. The scattering in the forward direction should be proportional
  # to the J-level scattering.  For Ho this is form( 10 to -10.)
  #*****************************************************************************#
> plot({seq( MatEl(s, 0, i, i), i =-8 ..8)}, s = 0 ..15, resolution = 400, thickness = 2, axesfont = [TIMES, ROMAN,
      16], labelfont = [TIMES, ROMAN, 14]);
```
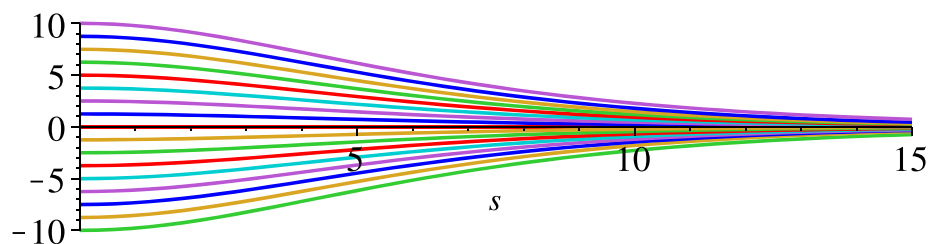
```
> #*********************************************************************#
  #proc to calculate nuclear structure factor
  #*********************************************************************#
> Fnuc := proc(h, k)
    local con, sum1, sum2, sum3, i, sumed;
    global bIn, bPt, bHo :
    con := 2·π·I;
    sum1 := 0 :
    sum2 := 0 :
    sum3 := 0 :
    for i from 1 to 3 do
      sum1 := sum1 + bHo·(exp(con·(h·posHo[i, 1] + k·posHo[i, 2]))) :
      sum2 := sum2 + bPt·(exp(con·(h·posPt[i, 1]  + k·posPt[i, 2]))) :
      sum3 := sum3 + bIn·(exp(con·(h·posIn[i, 1]  + k·posIn[i, 2]))) :
    end do;
    sumed := evalf(sum1 + sum2 + sum3) :
    return  sumed/2.69E−13;
  end proc:
```

```
> Fnuc(1, 1)
```

$$5.2023380100768834917574881081642595502692 - 2.807528930700603823848081794866463754043 \, I \qquad (2)$$

```
> #*********************************************************************#
  # Form factor calc, uses the am coefficents and the multipole matrix. sums diagonal elements
  # only. Defines what J values this runs over + to - J, or 0 to J etc.
> #*********************************************************************#
> Form := proc(h, k)
    local summat, M, Mp;
    global am;
    summat := 0;
    for M from -J to J do
      summat := summat + am[M + 9]²·evalf( ( MatEl(h, k, M, M) ) ) :
  # print( "Form routine", M, "   ", (am[M + 9])², "    ", MatEl(h, k, M, M), summat);
    end do:
    return summat;
  end proc:
> Form(0, 0);
```

$$3.768292307304721199633024089448535490007 \qquad (3)$$

```
> #*********************************************************************#
  # Proc to calculate the magnetic form factor. The moment is on the Ho site only.
  #*********************************************************************#
> Fmag := proc(h, k)
    local con, sum1, i;
    global bHo;
    con := 2·π·I;
    sum1 := 0 :
```

```
      for  i from 1 to 3 do
      sum1 := sum1 + (exp(con·(h·posHo[i, 1] + k·posHo[i, 2])));
      end do;
       sum1 := Form(h, k)·sum1;
       return evalf (sum1);
       end proc:
>  test := evalf (Fmag(0, 0));
```

$$test := 11.30487692191416359889907226834560647002 + 0.\,I \qquad\qquad (4)$$

```
>  #***********************************************************************#
      # Here the flipping ratio is calculated.
      #***********************************************************************#

>  R := proc(h, k)          # calculate the flipping ratio R as measured
       local fn, fm, r;
       fn := Fnuc(h, k) :
       fm := Fmag(h, k) :
```

$$r := \left(\frac{|fn + fm|}{|fn - fm|} \right);$$

```
       return r·r;
       end proc:
```

```
> #************************************************************************#
  # The data is loaded into a matrix, which initalises itself to the correct size.
  # dpoints is the number of data points red into the matrix.
> #************************************************************************#
>   data := Import("74kd3.xls") :
    dpoints := Size(data, 1);   # maple 12 onward
```
$$dpoints := 50 \tag{5}$$
```
> #************************************************************************#
  # Here all the 'colum indicies' are defined. This is for the 'Rdat' column data is written.
  # Rdat is for all the calculated data and is an "array" for compatibility with export function.
> #************************************************************************#
>  Cols := 13 :
   Rdat := Array(1 ..dpoints, 1 ..Cols, 0) :
   hCol := 1 :
   kCol := 2 :
   lCol := 3 :
   RobsCol := 4 :                       # R  measured on D3
   DRCol := 5 :                         # DR  measured on D3
   slamCol := 6 :                       # sin(thet) over lambda
   RcalcCol := 7 :                       # R calculated
   FormCol := 8 :                        # calculated form factor
   nucCol := 9 :                        #  nuclear structure factor
   magCol := 10 :                       #  magnetic structure factor
   mFcol := 11 :                        #  moment·form factor solution
   DmFcol := 12 :                       # caculated error bar
   NoRootscol := 13 :                   # number of physical roots
> #************************************************************************#
  #A larger array is initallised to store all the data caculated for plotting etc.
> #************************************************************************#
>  Cols := 15 :
   Rdat := Array(1 ..dpoints, 1 ..Cols, 0) :
     for i from 1 to dpoints do
         Rdat[i, hCol] := data[i, 1] :
         Rdat[i, kCol] := data[i, 2] :
         Rdat[i, lCol] := data[i, 3] :
         Rdat[i, RobsCol] := data[i, 4] :
         Rdat[i, DRCol] := data[i, 5] :
     end do:

> #************************************************************************#
  # Rdat is filled. Note, runtime is long if all items are appended.
> #************************************************************************#
>  for i from 1 to max(5, dpoints) do          # constructs a table of final data for export.
       h := Rdat[i, hCol];
       k := Rdat[i, kCol];
     Rdat[i, slamCol] := slam(h, k);                              # appends sin(Θ) λ
     Rdat[i, RcalcCol] := evalf(R(h, k));                          # appends R
     Rdat[i, FormCol] := evalf(Form(h, k));                       # appends Rform factor
     Rdat[i, nucCol] := |evalf(Fnuc(h, k))|;                      # appends MOD Fnuc
     Rdat[i, magCol] := |evalf(Fmag(h, k))|;                      # appends FmagMODto
    end do:
   lprint("Data array with appended data ") :
   print( "        h, k, l ,   Robs  ,  DRobs , Sin(th) /l ,  Rcalc,  |form|,  |Fnuc|, |Fmag| ") :
    for i from 1 to 5 do
   # print(Rdat[i, hCol], Rdat[i, kCol], Rdat[i, lCol], Rdat[i, RobsCol], Rdat[i, DRCol], Rdat[i, slamCol],
       Rdat[i, RcalcCol], Rdat[i, FormCol], Rdat[i, nucCol], Rdat[i, magCol]) :
    end do;

"Data array with appended data "
```
(6)

```
> #****************************************************************************#
  # The data is loaded into a matrix, which initalises itself to the correct size.
  # dpoints is the number of data points red into the matrix.
> #****************************************************************************#
>   data := Import("74kd3.xls") :
    dpoints := Size(data, 1) ;  # maple 12 onward
```
$$dpoints := 50 \qquad (5)$$
```
> #****************************************************************************#
  # Here all the 'colum indicies' are defined. This is for the 'Rdat' column data is written.
  # Rdat is for all the calculated data and is an "array" for compatibility with export function.
> #****************************************************************************#
>   Cols := 13 :
    Rdat := Array(1 ..dpoints, 1 ..Cols, 0) :
    hCol := 1 :
    kCol := 2 :
    lCol := 3 :
    RobsCol := 4 :                       # R  measured on D3
    DRCol := 5 :                         # DR  measured on D3
    slamCol := 6 :                       # sin(thet) over lambda
    RcalcCol := 7 :                      # R calculated
    FormCol := 8 :                       # calculated form factor
    nucCol := 9 :                        #  nuclear structure factor
    magCol := 10 :                       #  magnetic structure factor
    mFcol := 11 :                        #  moment·form factor solution
    DmFcol := 12 :                       # caculated error bar
    NoRootscol := 13 :                   # number of physical roots
> #****************************************************************************#
  #A larger array is initallised to store all the data caculated for plotting etc.
> #****************************************************************************#
>   Cols := 15 :
    Rdat := Array(1 ..dpoints, 1 ..Cols, 0) :
      for i from 1 to dpoints do
          Rdat[i, hCol] := data[i, 1] :
          Rdat[i, kCol] := data[i, 2] :
          Rdat[i, lCol] := data[i, 3] :
          Rdat[i, RobsCol] := data[i, 4] :
          Rdat[i, DRCol] := data[i, 5] :
      end do:

> #****************************************************************************#
  # Rdat is filled. Note, runtime is long if all items are appended.
> #****************************************************************************#
>   for i from 1 to max(5, dpoints) do          # constructs a table of final data for export.
      h := Rdat[i, hCol];
      k := Rdat[i, kCol];
      Rdat[i, slamCol] := slam(h, k);                                # appends sin(Θ) λ
      Rdat[i, RcalcCol] := evalf(R(h, k));                           # appends R
      Rdat[i, FormCol] := evalf(Form(h, k));                         # appends Rform factor
      Rdat[i, nucCol] := |evalf(Fnuc(h, k))|;                        # appends MOD Fnuc
      Rdat[i, magCol] := |evalf(Fmag(h, k))|;                        # appends FmagMODto
    end do:
    lprint("Data array with appended data ") :
    print( "        h, k, l ,   Robs  ,  DRobs , Sin(th) /l ,  Rcalc,  |form|,  |Fnuc|, |Fmag| ") :
     for i from 1 to 5 do
    # print(Rdat[i, hCol], Rdat[i, kCol], Rdat[i, lCol], Rdat[i, RobsCol], Rdat[i, DRCol], Rdat[i, slamCol],
          Rdat[i, RcalcCol], Rdat[i, FormCol], Rdat[i, nucCol], Rdat[i, magCol]) :
    end do;

"Data array with appended data "
```

for *i* **from** 1 **to** *dpoints* **do**

$$chisq := chisq + \left(\frac{Robs[i] - Rcalc[i]}{DRobs[i]} \right)^2 :$$

end do:

$$chisq := \frac{chisq}{31} ;$$

print("the χ^2 for this fit is", *chisq*) :

 # *display*(pRobs, pRcal, view = [0 ..0.85, 0 ..15], *axesfont* = [*TIMES, ROMAN*, 14], labels = ["sin(θ)/λ", "R"],
    labelfont = [*TIMES, ROMAN*, 14]) ;

#display(pRobs, pRcal, view = [0 ..0.85, 0 ..7], *textplot*([*seq*(*hklistR*[g], *g* = 1 ..dpoints)], *align* = {*above*,
    right})) ;

display(pRobs, pRcal, view = [0 ..0.85, 0 ..15], *textplot*([*seq*(*dlistR*[g], *g* = 1 ..dpoints)], *align* = {*above*,
    right})) ;

#display(pRobs, pRcal) ;   # *no y axis clipping*

#display(pRobs) ;   # *no y axis clipping*

#display(pform) ;

#display(*pfnuc*,) ;

#display(*pfmag*) ;

$$chisq := 245.8138216531880045384220148987133941259$$

"the χ^2 for this fit is", 245.8138216531880045384220148987133941259

<p style="padding-left:40px">>   *Export*(*Rdat*, "Rdat74K.xls") :</p>

    lprint("Data array exported ") :

    print("   h, k, l,   Robs , DRobs , Sin(th) /l , Rcalc, |form|, |Fnuc|, |Fmag| ") :

"Data array exported "

        "   h, k, l,   Robs , DRobs , Sin(th) /l , Rcalc, |form|, |Fnuc|, |Fmag| "   **(7)**

> #***#

> # The code now sorts the code and extracts the form factor from the Rcalc data. Note Rcalc

> # could be potentially fitted to Robs at this point using the am coefficients.

> #***#

```
> #*******************************************************************************#
> # The code now finds 'X' by casting the magnetic structure factor (MS) into the form
  # MS= X*exp(i.k.g) where X = |m|*f(k), which is the moment multiplied by the Ho
  # form factor. For this the 'R', 'Form' and 'Fmag' procedures are re-defined in a slightly
  # different way. This is shown by adding 'X' to the name.
> #*******************************************************************************#
> FormX := proc(h, k)
     local summat, M, Mp;
     global am;
     summat := 0;
     for M from -J to J do
        summat := summat + am[M + 9]²·evalf( ( MatEl(h, k, M, M) ) ) :
      end do:
     return summat;
     end proc:
> FmagX := proc(h, k)
     local con, sum1, i;
     con := 2·π·I;
     sum1 := 0 :
     for i from 1 to 3 do
     sum1 := sum1 + (exp(con·(h·posHo[i, 1] + k·posHo[i, 2]) ) );
     end do;
      sum1 := sum1;
     return evalf(sum1);
     end proc:
> RX := proc(h, k, x)
     local fn, fm, r;
     fn := Fnuc(h, k) :
     fm := x·FmagX(h, k) :
     r := ( |fn + fm| / |fn − fm| );

     return r·r;
     end proc:
> #*******************************************************************************#
  # Each individual reflection is examined for roots. ns (no solutions) is an arbitary value to fill
  # Rdat. Any entry with value 'ns' will later be discarded ready for fitting.
> #*******************************************************************************#
> ns := 4 :
> #*******************************************************************************#
  # NoRootscol is the number of roots that could be physically used - both have to be tried.
  # mFcol is the column index for Rdat table. Defined above.
> #*******************************************************************************#
>    for row from 1 to dpoints do  #data taken from Rdat
     Rob := Rdat[row, 4] :
     sol := evalf( fsolve(RX(Rdat[row, hCol], Rdat[row, kCol], x) = Rdat[row, RobsCol]) );
          if (type(sol, float) = false) then
             Rdat[row, mFcol] := ns;
          else
             Rdat[row, mFcol] := sol;
          end if;
     end do:
    #Rdat ;
>    #----- Individual reflection -----
     reflection := 23 :
     Rdat[reflection, mFcol] := evalf(fsolve(RX(Rdat[reflection, hCol], Rdat[reflection, kCol], x)
        = Rdat[reflection, RobsCol], x = 3 ..5) ) :
     Rdat[reflection, NoRootscol] := 1 :
    #----- Individual reflection -----
```
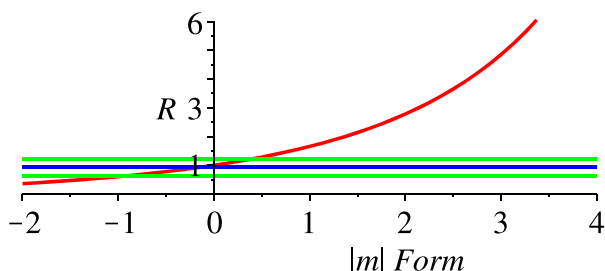
```
     reflection := 15 :
     Rdat[reflection, mFcol] := ns :
     Rdat[reflection, NoRootscol] := 1 :
   #----- Individual reflection -----
     reflection := 31 :
     Rdat[reflection, mFcol] := ns :
     Rdat[reflection, NoRootscol] := 1 :
   #----- Individual reflection -----
     reflection := 10 :
     Rdat[reflection, mFcol] := evalf (fsolve(RX(Rdat[reflection, hCol], Rdat[reflection, kCol], x)
       = Rdat[reflection, RobsCol], x = 1 ..3 ) ) :
     Rdat[reflection, NoRootscol] := 1 :
   #----- Individual reflection -----
     reflection := 41 :
     Rdat[reflection, mFcol] := evalf (fsolve(RX(Rdat[reflection, hCol], Rdat[reflection, kCol], x)
       = Rdat[reflection, RobsCol], x = 1 ..3 ) ) :
     Rdat[reflection, NoRootscol] := 1 :
   #----- Individual reflection -----
     reflection := 40 :
     Rdat[reflection, mFcol] := evalf (fsolve(RX(Rdat[reflection, hCol], Rdat[reflection, kCol], x)
       = Rdat[reflection, RobsCol], x = 1 ..3 ) ) :
     Rdat[reflection, NoRootscol] := 1 :
   #----- Individual reflection -----
     reflection := 20 :
     Rdat[reflection, mFcol] := ns :
     Rdat[reflection, NoRootscol] := 1 :
   #----- Individual reflection -----
     reflection := 30 :
     Rdat[reflection, mFcol] := ns :
     Rdat[reflection, NoRootscol] := 1 :
   #----- Individual reflection -----
> #***********************************************************************#
  # Now append the error bar to the extracted form factor
> #***********************************************************************#
> slice := 0.00000001 :
  for i from 1 to dpoints do
     if Rdat[i, mFcol] = ns then
        Rdat[i, DmFcol] := 0;
     else
        Rdat[i, DmFcol] := |(2·slice) / ( RX(Rdat[i, hCol], Rdat[i, kCol], Rdat[i, mFcol] + slice) − RX(Rdat[i,
        hCol], Rdat[i, kCol], Rdat[i, mFcol] − slice) )·Rdat[i, DRCol]|;
     end if;
  end do;
  #Rdat;
> #***********************************************************************#
  # Used to look at indiviual roots. change dset to view any one solution, data stored in Rdat
> #***********************************************************************#
> dset := 38;
  h := Rdat[dset, hCol];
  k := Rdat[dset, kCol];
  Rob := Rdat[dset, RobsCol];
  dRob := Rdat[dset, DRCol];
  findroot := evalf ( fsolve(RX(h, k, x) = Rdat[dset, RobsCol]) ) ;
  grad := RX(h, k, ( findroot + slice) ) − RX(h, k, ( findroot − slice) ) / 2·slice ;
  # mm := 1 / grad ;
  lowx := -2 :
  upx := 4 :
  sss := slam(h, k) :
```

$upy := 6$:
$lowy := 0$:
$dd := evalf\,(\,fsolve(RX(h, k, x) = \mathrm{Rob}, \mathrm{x} = 0\,)\,)$:
$Err := \dfrac{1}{grad}\cdot dRob$:
$FFerror := Rdat[\,dset, DmFcol\,]$;
$pc := \mathrm{Rob} - grad\cdot findroot$;
$\#plot(\,[\,RX(h, k, x), \mathrm{Rob}, (\mathrm{Rob} + dRob), (\mathrm{Rob} - dRob), grad\cdot\mathrm{x} + \mathrm{pc}, \,], x = \mathrm{lowx}\,..\mathrm{upx}, thickness = 2, resolution$
$\qquad = 150, axesfont = [\,TIMES, ROMAN, 14\,], color = [\,red, blue, green, green, brown\,], labels = [\,|m|\, \cdot\, Form,$
$\qquad R\,], labelfont = [\,TIMES, ROMAN, 14\,], legend = [\,Function\ R, R\ measured, + DR, - DR, Error\,], legendstyle$
$\qquad = [\,location = right\,], view = [\,\mathrm{lowx}\,..\mathrm{upx}, \mathrm{lowy}\,..\mathrm{upy}\,])$;
$\#plot(\,[\,RX(h, k, x), \mathrm{Rob}, (\mathrm{Rob} + dRob), (\mathrm{Rob} - dRob), grad\cdot\mathrm{x} + \mathrm{pc}, \,], x = \mathrm{lowx}\,..\mathrm{upx}, thickness = 2, resolution$
$\qquad = 800, axesfont = [\,TIMES, ROMAN, 14\,], color = [\,red, blue, green, green, brown\,], labels = [\,|m|\, \cdot\, Form,$
$\qquad R\,], labelfont = [\,TIMES, ROMAN, 14\,], view = [\,\mathrm{lowx}\,..\mathrm{upx}, \mathrm{lowy}\,..\mathrm{upy}\,])$;
$plot(\,[\,RX(h, k, x), \mathrm{Rob}, (\mathrm{Rob} + dRob), (\mathrm{Rob} - dRob)\,], x = \mathrm{lowx}\,..\mathrm{upx}, thickness = 2, resolution = 800, axesfont$
$\qquad = [\,TIMES, ROMAN, 14\,], color = [\,red, blue, green, green, brown\,], labels = [\,|m|\, \cdot\, Form, R\,], labelfont$
$\qquad = [\,TIMES, ROMAN, 14\,], view = [\,\mathrm{lowx}\,..\mathrm{upx}, \mathrm{lowy}\,..\mathrm{upy}\,])$;

$$dset := 38$$
$$h := 9.0$$
$$k := 1.0$$
$$Rob := 0.92309$$
$$dRob := 0.302939$$
$$findroot := -0.159664374510910805599647313528436363631951$$
$$grad := 0.4628035682827669638153336920942435000000$$
$$FFerror := 0.6545736047888641368041324269944611510416$$
$$pc := 0.9969832422512855861711962746037965004897$$

```
> noDel := 0 :
  for i from 1 to dpoints do
    if Rdat[i, mFcol] = ns then
    noDel := noDel + 1;                    #noDel is the number of point to delete from Rdat
  end if:
  end do:
  print("number of points removed =", noDel);
  Gdpoints := dpoints − noDel :
  print("number of points removed =", noDel, "leaving", Gdpoints);
  hkF := Matrix(Gdpoints, 7, 0) :            # new data Matrix initallised to contain final GOOD data points
  pos := 1 :
  for i from 1 to (dpoints) do
  if Rdat[i, mFcol] ≠ ns then
  hkF[pos, 1] := Rdat[i, hCol];            #h
  hkF[pos, 2] := Rdat[i, kCol];            #k
```

```
    hkF[ pos, 3 ] := Rdat[i, mFcol];              #mF=X
    hkF[ pos, 4 ] := Rdat[i, DmFcol];             #DmF
    hkF[ pos, 5 ] := Rdat[i, RobsCol];             # R
    hkF[ pos, 6 ] := Rdat[i, DRCol];              #DR
    hkF[ pos, 7 ] := FormX(Rdat[i, hCol], Rdat[i, kCol]) : #calculated form factor
    pos := pos + 1;
    end if:
    end do:
    hkF
```

$$\text{"number of points removed ="}, 15$$
$$\text{"number of points removed ="}, 15, \text{"leaving"}, 35$$

$$\begin{bmatrix} 35 \times 7 \ Matrix \\ Data \ Type: \ anything \\ Storage: \ rectangular \\ Order: \ Fortran\_order \end{bmatrix} \tag{8}$$

```
> #********************************************************************************#
  # plots constructed to check output, plotted with the form factor before fitting.
  # New vectors initalised and filled for plot commands.
  # Data arrays given the suffix 'G' for 'Good data'
> #********************************************************************************#
> sthetG := Vector(Gdpoints, 0) :
  momFG := Vector(Gdpoints, 0) :
  DmomFG := Vector(Gdpoints, 0) :
  formGcalc := Vector(Gdpoints, 0) :
  hklabelsG := Array(1 ..Gdpoints, 1 ..3, 0) :         # have to define an array to achive 'list of lists' convertion!
  dlabelsG := Array(1 ..Gdpoints, 1 ..3, 0) :
         # have to define an array to achive 'list of lists' convertion!
    for i from 1 to Gdpoints do
       sthetG[i] := slam(hkF[i, 1], hkF[i, 2]);
       momFG[i] := hkF[i, 3] :                          #filled with moment ·form factor
       DmomFG[i] := hkF[i, 4] :                         #filled with  error
       formGcalc[i] := hkF[i, 7] :                      #filled with  the calculated form factor
       dlabelsG[i, 1] := sthetG[i];
       dlabelsG[i, 2] := momFG[i];
       dlabelsG[i, 3] := i;

       hklabelsG[i, 1] := sthetG[i];
       hklabelsG[i, 2] := momFG[i];
       hklabelsG[i, 3] := (gethklabel(hkF[i, 1], hkF[i, 2]));
    end do:

  dlistG := convert(dlabelsG, listlist) :          #conversion for 'list of lists' convention in text plot!
  hklistG := convert(hklabelsG, listlist) :         #conversion for 'list of lists' convention in text plot!
  # now plot strings defined ready for "display" command #
  pformxG := ScatterPlot(sthetG, momFG, title = "Form Factor from R", colour = blue, labels = ["sin(θ)/λ",
         "Form |M|"], linestyle = solid, yerrors = [DmomFG, DmomFG]) :
  pformcalG := ScatterPlot(sthetG, formGcalc, title = "Form Factor from R", colour = orange, labels
         = ["sin(θ)/λ", "Form |M|"]) :
  p00 := ScatterPlot([0], [FormX(0, 0)], colour = green, symbol = asterisk, symbolsize = 15) :
> #********************************************************************************#
  #  plots displayed with current ChiSq calculatred
> #********************************************************************************#
> chisq := 0 :
    for i from 1 to Gdpoints do
```

$$chisq := chisq + \left(\frac{momFG[i] - formGcalc[i]}{DmomFG[i]} \right)^2 :$$

```
    end do:
```

$$chisq := \frac{chisq}{Gdpoints};$$

#display(p00, pformxG, pformcalG, view = [0 ..0.8, 0 ..4.5]);
display(p00, pformxG, pformcalG, textplot([seq(dlistG[g], g = 1 ..Gdpoints)], align = {above, right}), view
     = [0 ..0.8, 0 ..4.5]) ;
#display(p00, pformxG, pformcalG, textplot([seq(hklistG[g], g = 1 ..Gdpoints)], align = {above, right}), view
     = [0 ..0.8, -3 ..4.5]) ;
#hkF;
#Rdat;

chisq := 4.79152406466475575574844183684755182954

Form Factor from R
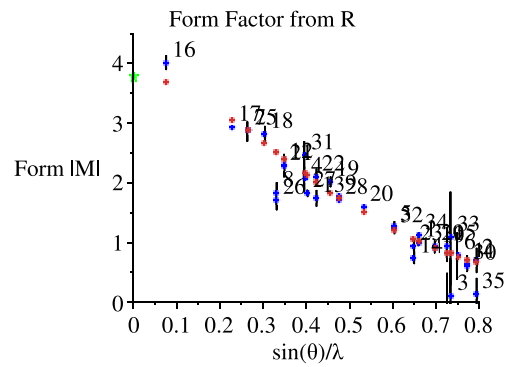
> #**#
  # End of data reduction. Now fitttinf form factor to experimental results.
  #**#

Appendix D

Flipping Ratio Data

The complete set of data for the T=74 K D3 experiment is tabulated below. This data used to produce figure 6.9. R_{D3} is the flipping ratio as measured on D3, with the experimental error $\pm\Delta$. R_{calc} is the calculated flipping ratio using the approximation to the form factor discussed in section 6.3.2.3. 'X' is the solution used to calculate the Ho^{3+} form factor from R_{D3}. $X = |m|*f(\boldsymbol{\kappa})$. $|F_N|$ and $|F_M|$ are the calculated nuclear and magnetic structure factors respectively.

h	k	1	R_{D3}	$\pm\Delta$	R_{calc}	R_{Diff}	$\frac{sin(\theta)}{\lambda}$	X	F_M [μ_B]	F_N [μ_B]	F_N [$10^{-12}cm$]	F_M [$10^{-12}cm$]
10	-5	0	1.894	0.054	2.012	0.118	0.658	1.084	17.446	3.098	1.673	4.693
12	-5	0	2.227	0.530	1.560	-0.666	0.794	0.396	8.175	0.912	0.493	2.199
8	-4	0	1.166	0.043	1.091	-0.075	0.527	1.573	12.925	4.444	2.400	3.477
11	-4	0	0.990	0.051	0.941	-0.049	0.733	0.720	11.789	1.447	0.781	3.171
6	-3	0	1.546	0.056	1.521	-0.026	0.395	1.972	10.905	3.367	1.818	2.933
7	-3	0	8.239	3.061	4.135	-4.103	0.462	1.759	3.961	1.898	1.025	1.065
9	-3	0	1.842	0.059	1.867	0.025	0.603	1.313	11.031	3.331	1.799	2.967
11	-3	0	3.087	1.762	2.514	-0.573	0.749	0.639	5.060	1.291	0.697	1.361
4	-2	0	1.495	0.028	1.463	-0.032	0.263	2.680	9.762	3.014	1.627	2.626
5	-2	0	4.506	0.287	4.976	0.470	0.331	2.250	3.942	3.503	1.891	1.060
6	-2	0	10.364	0.795	10.953	0.588	0.402	1.946	8.464	4.573	2.469	2.277
7	-2	0	2.433	0.033	2.386	-0.047	0.475	1.724	15.363	3.364	1.817	4.133
10	-2	0	1.430	0.045	1.425	-0.004	0.697	0.904	13.325	1.181	0.638	3.584
11	-2	0	1.895	0.252	1.657	-0.239	0.772	0.517	9.147	1.148	0.620	2.460
2	-1	0	0.982	0.003	0.883	-0.099	0.132	3.787	5.912	9.062	4.894	1.590
3	-1	0	13.403	0.793	16.943	3.541	0.201	3.187	7.118	4.388	2.370	1.915
4	-1	0	21.643	1.234	71.572	49.929	0.274	2.602	7.470	6.835	3.691	2.010
5	-1	0	0.643	0.020	0.662	0.019	0.348	2.165	10.048	1.458	0.787	2.703
6	-1	0	1.970	0.092	2.060	0.089	0.423	1.876	4.923	1.674	0.904	1.324
8	-1	0	1.069	0.026	1.022	-0.047	0.574	1.420	12.142	1.837	0.992	3.266
9	-1	0	3.218	0.471	6.379	3.161	0.650	1.123	7.206	3.121	1.685	1.938
10	-1	0	1.597	0.196	1.466	-0.131	0.725	0.761	6.812	0.650	0.351	1.833
1	0	0	2.827	0.090	2.714	-0.113	0.076	4.177	0.682	2.790	1.506	0.184
2	0	0	11.104	0.527	15.338	4.234	0.152	3.616	3.823	6.445	3.480	1.028

h	k	l	R_{D3}	$\pm\Delta$	R_{calc}	R_{Diff}	$\frac{sin(\theta)}{\lambda}$	X	$F_M\ [\mu_B]$	$F_N\ [\mu_B]$	F_N $[10^{-12}cm]$	F_M $[10^{-12}cm]$
3	0	0	2.622	0.021	2.649	0.026	0.228	2.957	16.887	4.033	2.178	4.543
4	0	0	0.247	0.017	0.308	0.061	0.304	2.405	3.267	0.934	0.504	0.879
5	0	0	11.395	1.678	21.316	9.921	0.380	2.028	9.299	5.988	3.233	2.501
6	0	0	0.351	0.016	0.400	0.049	0.456	1.777	6.857	1.542	0.833	1.844
7	0	0	4.689	0.204	4.534	-0.155	0.532	1.557	9.331	3.367	1.818	2.510
9	0	0	0.997	0.066	0.984	-0.012	0.684	0.964	10.362	0.041	0.022	2.787
1	1	0	1.005	0.003	0.883	-0.122	0.132	3.787	5.912	9.062	4.894	1.590
2	1	0	13.089	0.545	16.943	3.854	0.201	3.187	7.118	4.388	2.370	1.915
3	1	0	23.818	1.486	71.572	47.754	0.274	2.602	7.470	6.835	3.691	2.010
4	1	0	0.649	0.020	0.662	0.013	0.348	2.165	10.048	1.458	0.787	2.703
5	1	0	2.216	0.095	2.060	-0.156	0.423	1.876	4.923	1.674	0.904	1.324
7	1	0	1.086	0.028	1.022	-0.064	0.574	1.420	12.142	1.837	0.992	3.266
8	1	0	4.561	0.962	6.379	1.819	0.650	1.123	7.206	3.121	1.685	1.938
9	1	0	0.923	0.303	1.466	0.543	0.725	0.761	6.812	0.650	0.351	1.833
2	2	0	1.495	0.028	1.463	-0.032	0.263	2.680	9.762	3.014	1.627	2.626
3	2	0	4.278	0.293	4.976	0.698	0.331	2.250	3.942	3.503	1.891	1.060
4	2	0	9.297	0.671	10.953	1.655	0.402	1.946	8.464	4.573	2.469	2.277
5	2	0	2.392	0.029	2.386	-0.005	0.475	1.724	15.363	3.364	1.817	4.133
8	2	0	1.450	0.050	1.425	-0.025	0.697	0.904	13.325	1.181	0.638	3.584
9	2	0	1.844	0.105	1.657	-0.187	0.772	0.517	9.147	1.148	0.620	2.460
3	3	0	1.654	0.059	1.521	-0.133	0.395	1.972	10.905	3.367	1.818	2.933
6	3	0	1.809	0.063	1.867	0.058	0.603	1.313	11.031	3.331	1.799	2.967
4	4	0	1.158	0.033	1.091	-0.067	0.527	1.573	12.925	4.444	2.400	3.477
7	4	0	0.914	0.056	0.941	0.026	0.733	0.720	11.789	1.447	0.781	3.171
5	5	0	2.041	0.061	2.012	-0.030	0.658	1.084	17.446	3.098	1.673	4.693
7	5	0	1.170	0.350	1.560	0.390	0.794	0.396	8.175	0.912	0.493	2.199

Bibliography

[1] Baran, S., Gondek, Ł., Hernández-Velasco, J., Kaczorowski, D., and Szytuła, A. *JMMM* **305**, 196 (2006).

[2] Morosan, E., Bud'ko, S. L., and Canfield, P. C. *Phys. Rev. B* **72**, 014425 (2005).

[3] Watson, K. C., Crangle, J., Neumann, K. U., and Ziebeck, K. R. A. *JMMM* **140**, 883 (1995).

[4] Stephens, T. *An Investigation of the Magnetic Properties of Heavy REPtIn Alloys*. PhD thesis, Loughborough Univeristy, (2005).

[5] Jensen, J. and Mackintosh, A. R. *Rare Earth Magnetism*. Clarendon Press Oxford, (1991).

[6] Morosan, E., Bud'ko, S. L., and Canfield, P. C. *Physical Review B* **71**, 014445 (2005).

[7] Szytuła, A., Baran, S., Gondek, Ł., Arulraj, A., Penc, B., Arulraj, A., and Stüsser, N. *Acta Physica Polonica A* **117**(4), 590 (2010).

[8] R. Pöttgen, Z. K. *Z. Kristallogr.* **211**, 884 (1996).

[9] Ferro, R., Marazza, R., and Rambaldi, G. *Zeitschrift für anorganische und allgemeine Chemie* **410**, 219 (1974).

[10] Rossi, D., Mazzone, D., Marazza, R., and R.Ferro. *Zeitschrift für anorganische und allgemeine Chemie* **507**, 235 (1983).

[11] Chubukov, A. *Phys. Rev. Lett.* **69**(5), 832 (1992).

[12] Sachdev, S. *Phys. Rev. B* **45**(21), 12377–12396 (1992).

[13] Moriya, T. *Phys. Rev. Lett.* **4**(5), 228 (1960).

[14] Dzyaloshinsky, I. *Journal of Physics and Chemistry of Solids* **4**(4), 241 (1958).

[15] Hund, F. *Z. Phys.* **33**(1), 855 (1925).

[16] Balcar, E. and Lovesey, S. *J. Phys.:Condens. Matter* **3**, 7095 (1991).

[17] Ruderman, M. A. and Kittel, C. *Phys. Rev.* **96**(1), 99 (1954).

[18] Bland, J. *http://www.cmp.liv.ac.uk/frink/thesis/thesis/node71.html.* (2003).

[19] Toulouse, G. *Commun. Phys.* **2**, 115 (1977).

[20] Ludwig, W. and Falter, C. *Symmetries in Physics.* Springer-Verlag Berlin Heidelberg, (1988).

[21] Stevens, K. W. H. *Proc. Phys. Soc. A* **65**, 209 (1952).

[22] Watson, K. *Investigation of the Magnetic and Lattice Properties of REPtIn and RE₂AgIn.* PhD thesis, Loughborough University, (1998).

[23] Zaremba, V. I., Galadzhun, Y. V., Belan, B. D., Pikul, A., Stepien-Damm, J., and Kaczorowski, D. *Journal of Alloys and Compounds* **316**, 64 (2000).

[24] Baran, S., Gondek, Ł., Hernández-Velasco, J., Kaczorowski, D., and Szytuła, A. *JMMM* **300**, 484–489 (2006).

[25] Baran, S., Kaczorowski, D., Szytuła, A., Penc, B., and Arulraj, A. *JMMM* **322**(15), 2177 (2010).

[26] Kaczorowski, D., Andraka, B., Pietri, R., Cichorek, T., and Zaremba, V. I. *Phys. Rev. B* **61**, 15255 (2000).

[27] Hansen, T., Henry, P., Fischer, H., Torregrossa, J., and Convert, P. *Measurement Science and Technology* **19**(3), 6 (2008).

[28] Fujita, T., Satoh, K., Maeno, Y., Uwatoko, Y., and Fujii, H. *JMMM* **76**, 133 (1988).

[29] Morosan, E., Bud'ko, S. L., Mozharivskyj, Y. A., and Canfield, P. C. *Phys. Rev. B* **73**, 17 (2006).

[30] Lovesey, S. W. *Theory of neutron scattering from condensed matter.* Oxford Scientific Publications, (1984).

[31] Squires, G. *Introduction to the theory of thermal neutron scattering.* Cambridge University Press, (1978).

[32] Giacovazzo, C., Monaco, H., Artioli, G., Viterbo, D., Ferraris, G., Gilli, G., Zanotti, G., and Catti, M. *Fundamentals of Crystallography.* Oxford University Press, (2002).

[33] Hartree, D. R. *The Calculations of Atomic Structure.* John Wiley and Sons New York, (1957).

[34] Lovesey, S. and Rimmer, D. *Rep. Prog. Phys* **32**, 333 (1969).

[35] Prince, E. *International Tables for Crystallography Volume C.* Kluwer Academic Publishers, (2003 3rd Edition).

[36] Condon, E. U. and Odabaşi, H. *Atomic Structure.* Cambridge University Press, (1980).

[37] Richard, D., Ferrand, M., and Kearley, G. *J. Neutron Research* **4**, 33 (1996).

[38] Rodriguez-Carvajal, J. *Physica B.* **192**, 55 (1993).

[39] Rodríguez-Carvajal, J. *Basireps;.* the program can be freely downloaded at ftp://ftp.cea.fr/pub/llb/divers/BasIreps, (2004).

[40] Lelièvre-Berna, E., Bourgeat-Lami, E., Gibert, Y., Kernavanois, N., Locatelli, J., Mary, T., Pastrello, G., Petukhov, A., Pujol, S., Rouques, R., Thomas, F., Thomas, M., and Tasset, F. *Physica B: Condensed Matter* **356**(1), 141 (2005).

[41] *http://www.ill.eu/instruments-support/instruments-groups/instruments/d9/.*

[42] Ouladdiaf, B., Archer, J., McIntyre, G., Hewat, A., Brau, D., and York, S. *Physica B: Condensed Matter* **385**(2), 1052 (2006).

[43] Brown, P. J. *Journal of Neutron Research* **4**(1), 25 (1996).

[44] Brown, J. and Wilson(Ed), A. *International Tables of Crystallography, Vol. C: Mathematical Physical and Chemical Tables*, volume 4.4. Kluwer Academic Publishers, London, (1996).

[45] Jaynes, E. T. *Phys. Rev.* **106**(4), 620 (1957).

[46] Buck(Ed), B. and Macaulay(Ed), V. *Maximum Entropy in Action.* Oxford Science Publications, (1992).

[47] Moze, O. and Buschow(Ed), K. *Crystal Field Effects in Intermetallic Compounds Studied by Inelastic Neutron Scattering.* Elsevier Science B.V., (1998).

[48] Becker(Ed), P. *Electron and Magnetization Density in Molecules and Crystals.* Plenum Press, New York, (1980).

[49] Nathans, R., Shull, C., Shirane, G., and Andresen, A. *Journal of Physics and Chemistry of Solids* **10**(2), 138 (1959).

[50] Blume, M. *Phys. Rev.* **130**(5), 1670 (1963).

[51] Brown, P. and Forsyth, J. *Br. J. Appl. Phys.* **15**, 1529 (1964).